UNIVERSITA' DEGLI STUDI DI VERONA

DEPARTMENT OF COMPUTER SCIENCE

GRADUATE SCHOOL OF NATURAL SCIENCES AND ENGINEERING

DOCTORAL PROGRAM IN COMPUTER SCIENCE

With the financial contribution of University of Verona

31° Cycle (starting year 2015)

DOCTORAL THESIS

STUDYING BRAIN CONNECTIVITY: A NEW MULTIMODAL APPROACH FOR STRUCTURE AND FUNCTION INTEGRATION

S.S.D. *INF/01*

Coordinator: Prof./ssa *Massimo Merro*

Signature _____

Tutor: Prof./ssa *Gloria Menegaz*

Signature _____

Doctoral Student: Dott./ssa *Silvia Obertino*

Signature _____

Studying brain connectivity: a new multimodal approach for structure and function integration

Silvia Obertino

Tesi di Dottorato

Verona, 25 November 2018

"Tu puoi aumentare il potere del tuo cervello da tre a cinque volte semplicemente ridendo e divertendoti prima di lavorare ad un problema."

DOUG HALL

ACKNOWLEDGMENT

Questa tesi è il risultato di tre lunghi e intensi anni di lavoro. Questo percorso ha rappresentato per me una delle più grandi sfide della mia vita, nonché la più grande soddisfazione. Sono stati anni difficili, pieni di difficoltà, battaglie, incomprensioni e litigi, ma anche pieni di soddisfazioni. Per questo ringrazio prima di tutto mio marito Paolo, a cui dedico questa ricerca, perché senza il suo amore e il suo sostegno incrollabile avrei fatto l'errore più grande della mia vita, abbandonando questo percorso a un anno dal traguardo. Ringrazio i miei genitori, mio fratello e i miei nonni che mi hanno sostenuta e affiancata nelle diverse decisioni difficili, sostenendomi anche quando pensavo di lasciare tutto. Vorrei ringraziare con immenso affetto i miei colleghi e amici del Laboratorio MIPLAB a Ginevra, che mi hanno fatto sentire per la prima volta nella mia vita accettata in un gruppo, facendomi sentire amata anche a seicento chilometri di distanza da casa mia. Ringrazio soprattutto il Prof. Dimitri Van De Ville ed Elvira Pirondini PhD. per la loro infinità pazienza nell'aiutarmi a superare le difficili battaglie, aiutandomi a crescere, e insegnandomi a gestire anche le situazioni più difficili. Li ringrazio soprattutto per avere guidato saggiamente il mio ultimo anno di ricerca, dandomi la possibilità di concludere la mia tesi. Un ringraziamento speciale va al Prof. Dimitri Van De Ville che mi ha permesso di vivere un'esperienza di ricerca a Ginevra nel suo laboratorio. Vorrei ringraziare a uno a uno tutti i membri del MIPLAB, a partire dalla mia vicina di scrivania Anjali, nonché compagna di viaggio con Younes a Lione, Lorena: mitica compagna di bevute al CB Happy Hour, Giulia B: la nostra super dottoressa in medicina con una vita nascosta da cantante lirica, Thomas: il pazzo svizzero che canta in giapponese, ma che ti strappa sempre un sorriso, e poi ancora Nawal, Serafeim, Nicolas, Yasaman, Daniela, Raphael e Miljan. Ne mancano ancora due, a cui però dedicherei qualche parola in più: Maria Giulia, che oltre ad aver aiutato nel processo di review della mia tesi è stata il mio punto di riferimento nel laboratorio per tutto il tempo; e Vanessa che ringrazio infinitamente per tutto il bene che mi ha dimostrato, per la bellissima opportunità che abbiamo avuto di collaborare su diversi progetti, e soprattutto per la consapevolezza che in giro per il mondo esiste un ologramma su vetro del mio cervello in una mostra d'arte. Ringrazio ancora tutte le ragazze del MIPLAB, studentesse comprese, che mi hanno organizzato una bellissima festa a sorpresa prima del mio matrimonio, dimostrando di aver imparato a conoscermi così profondamente in così poco tempo, condividendo momenti di pura gioia che non dimenticherò mai. Un doveroso ringraziamento va alla mia supervisor Prof. Gloria Menegaz, che mi ha guidata, a suo modo in questi tre anni, fortificandomi. Ultimo ma non ultimo, ringrazio il Prof. Alessandro Daducci e il Prof. Massimo Merro, che mi hanno dimostrato che non bisogna mai mollare per le cose a cui si tiene. Infine, ringrazio questo percorso di vita e le difficoltà incontrate per avermi aperto gli occhi su cosa davvero è importante nella vita e che cosa voglio davvero fare per il resto della mia vita.

ABSTRACT

The brain is a complex system of which anatomical and functional organization is both segregated and integrated. A longstanding question for the neuroscience community has been to elucidate the mutual influences between structure and function. To that aim, first, structural and functional connectivity need to be explored individually. Structural connectivity can be measured by the Diffusion Magnetic Resonance signal followed by successive computational steps up to virtual tractography. Functional connectivity can be established by correlation between the brain activity time courses measured by different modalities, such as functional Magnetic Resonance Imaging or Electro/Magneto Encephalography. Recently, the Graph Signal Processing (GSP) framework has provided a new way to jointly analyse structure and function. In particular, this framework extends and generalizes many classical signal-processing operations to graphs (e.g., spectral analysis, filtering, and so on). The graph here is built by the structural connectome; i.e., the anatomical backbone of the brain where nodes represent brain regions and edge weights strength of structural connectivity. The functional signals are considered as time-dependent graph signals; i.e., measures associated to the nodes of the graph. The concept of the Graph Fourier Transform then allows decomposing regional functional signals into, on one side, a portion that strongly aligned with the underlying structural network ("aligned"), and, on the other side, a portion that is not well aligned with structure ("liberal"). The proportion of aligned-vs-liberal energy in functional signals has been associated with cognitive flexibility. However, the interpretation of these multimodal relationships is still limited and unexplored for higher temporal resolution functional signals such as M/EEG. Moreover, the construction of the structural connectome itself using tractography is still a challenging topic, for which, in the last decade, many new advanced models were proposed, but their impact on the connectome remains unclear.

In the first part of this thesis, I disentangled the variability of tractograms derived from different tractography methods, comparing them with a test-retest paradigm, which allows to define specificity and sensitivity of each model. I want to find the best trade-off between specificity and sensitivity to define the best model that can be deployed for analysis of functional signals. Moreover, I addressed the issue of weighing the graph comparing few estimates, highlighting the sufficiency of binary connectivity, and the power of the latest-generation microstructural properties in clinical applications.

In the second part, I developed a GSP method that allows applying the aligned and liberal filters to M/EEG signals. The model extends the structural constraints to consider indirect connections, which recently demonstrated to be powerful in the structure/function link. I then show that it is possible to identify dynamic changes in aligned-vs-liberal energy, highlighting fluctuations present motor task and resting state. This model opens the perspective of novel biomarkers. Indeed, M/EEG are often used in clinical applications; e.g., multimodal integration in data from Parkinson's disease or stroke could combine changes of both structural and functional connectivity.

SOMMARIO

Il cervello è un sistema che integra organizzazioni anatomiche e funzionali. Negli ultimi dieci anni, la comunità neuroscientifica si è posta la domanda sulla relazione struttura-funzione. Essa può essere esplorata attraverso lo studio della connettività. Nello specifico, la connettività strutturale può essere definita dal segnale di risonanza magnetica pesato in diffusione seguito dalla computazione della trattografia; mentre la correlazione funzionale del cervello può essere calcolata a partire da diversi segnali, come la risonanza magnetica funzionale o l'elettro-/magneto-encefalografia, che consente la cattura del segnale di attivazione cerebrale a una risoluzione temporale più elevata. Recentemente, la relazione struttura-funzione è stata esplorata utilizzando strumenti di elaborazione del segnale sui grafi, che estendono e generalizzano le operazioni di elaborazione del segnale ai grafi. In specifico, alcuni studi utilizzano la trasformata di Fourier applicata alla connettività strutturale per misurare la decomposizione del segnale funzionale in porzioni che si allineano ("aligned") e non si allineano ("liberal") con la sottostante rete di materia bianca. Il relativo allineamento funzionale con l'anatomia è stato associato alla flessibilità cognitiva, sottolineando forti allineamenti di attività corticali, e suggerendo che i sistemi sottocorticali contengono più segnali liberi rispetto alla corteccia. Queste relazioni multimodali non sono, però, ancora chiare per segnali con elevata risoluzione temporale, oltre ad essere ristretti a specifiche zone cerebrali. Oltretutto, al giorno d'oggi la ricostruzione della trattografia è ancora un argomento impegnativo, soprattutto se utilizzata per l'estrazione della connettività strutturale. Nel corso dell'ultimo decennio si è vista una proliferazione di nuovi modelli per ricostruire la trattografia, ma il loro conseguente effetto sullo strumento di connettività non è ancora chiaro.

In questa tesi, ho districato i dubbi sulla variabilità dei trattogrammi derivati da diversi metodi di trattografia, confrontandoli con un paradigma di test-retest, che consente di definire la specificità e la sensibilità di ciascun modello. Ho cercato di trovare un compromesso tra queste, per definire un miglior metodo trattografico. Inoltre, ho affrontato il problema dei grafi pesati confrontando alcune possibili stime, evidenziando la sufficienza della connettività binaria e la potenza delle proprietà microstrutturali di nuova generazione nelle applicazioni cliniche. Qui, ho sviluppato un modello di proiezione che consente l'uso dei filtri aligned e liberal per i segnali di encefalografia. Il modello estende i vincoli strutturali per considerare le connessioni indirette, che recentemente si sono dimostrate utili nella relazione struttura-funzione.

I risultati preliminari del nuovo modello indicano un'implicazione dinamica di momenti più aligned e momenti più liberal, evidenziando le fluttuazioni presenti nello stato di riposo. Inoltre, viene presentata una relazione specifica di periodi più allineati e liberali per il paradigma motorio. Questo modello apre la prospettiva alla definizione di nuovi biomarcatori. Considerando che l'encefalografia è spesso usata nelle applicazioni cliniche, questa integrazione multimodale applicata su dati di Parkinson o di ictus potrebbe combinare le informazioni dei cambiamenti strutturali e funzionali nelle connessioni cerebrali, che al momento sono state dimostrate individualmente.

Index

MAIN PUBLICATIONS

Brusini, L., Obertino, S., Zucchelli, M., Galazzo, I. B., Krueger, G., Granziera, C., & Menegaz, G. (2015, October). **Assessment of mean apparent propagator-based indices as biomarkers of axonal remodeling after stroke**. *Proc. In International Conference on Medical Image Computing and Computer-Assisted Intervention (MICCAI)* (pp. 199-206). Springer, Cham.

Brusini, L., Obertino, S., Galazzo, I. B., Zucchelli, M., Krueger, G., Granziera, C., & Menegaz, G. (2016). **Ensemble average propagator-based detection of microstructural alterations after stroke**. *International journal of computer assisted radiology and surgery*, 11(9), 1585-1597.

Mendez, A., Obertino, S., & Menegaz, G. (2016, June). **Shore-based microstructural indices: do they tell us more?** *Proc. In Pattern Recognition in Neuroimaging (PRNI), 2016 International Workshop* (pp. 1-4). IEEE.

Obertino, S., Granziera, C., & Menegaz, G. (2016, June). **Infinite feature selection on shore-based biomarkers reveals connectivity modulation after stroke**. *Proc. In Pattern Recognition in Neuroimaging (PRNI), 2016 International Workshop* (pp. 1-4). IEEE.

Obertino, S., Storti, S.F., Daducci, A., Granziera, C., & Menegaz, G. (2016, June). **Graph-based analysis of the structural connectivity network modulation in stroke patients**. *Proc. In Organization for Human Brain Mapping (OHBM), 2016 Annual Meeting* (pp. 1).

Obertino, S., Danti, F., Zucchelli, M., Pizzini, F., & Menegaz, G. (2017, April). **Can we trust structural connectivity?** *Proc. In International Society for Magnetic Resonance in Medicine (ISMRM), 2017 Annual Meeting & Exhibition* (pp. 1765).

Obertino, S., Hernández, S. J., Galazzo, I. B., Pizzini, F. B., Zucchelli, M., & Menegaz, G. (2017, September). **Exploiting Machine Learning Principles for Assessing the Fingerprinting Potential of Connectivity Features**. *Proc. In Computational Diffusion MRI Workshop (CDMRI) of International Conference on Medical Image Computing and Computer-Assisted Intervention (MICCAI)* (pp. 175-188). Springer, Cham.

Boscolo Galazzo, I., Brusini, L., Obertino, S., Zucchelli, M., Granziera, C., & Menegaz, G. (2018). **On the Viability of Diffusion MRI-Based Microstructural Biomarkers in Ischemic Stroke**. *Frontiers in neuroscience*, 12, 92.

Obertino, S., Pirondini, E., Menegaz, G. & Van De Ville, D. (under submission). **Graph signal processing to combine structure and function**.

LIST OF ACRONYMS

MRI - Magnetic Resonance Imaging

EEG – Electro Encephalography

MEG – Magneto Encephalography

fMRI – functional Magnetic Resonance Imaging

BOLD – blood oxygen level dependent

DWI – Diffusion Weighted Imaging

WM – White Matter

GM – Grey Matter

CSF – Cerebral Spinal Fluid

ODF – Orientation Distribution Function

HARDI - High Angular Resolution Diffusion Imaging

DSI – Diffusion Spectrum Imaging

EAP – Ensemble Average Propagator

DTI – Diffusion Tensor Imaging

SH – Spherical Harmonics

fODF – fiber ODF

SD – Spherical Deconvolution

NODDI – Neurite Orientation Dispersion and Density Imaging

SHORE – Simple Harmonic Oscillator based Reconstruction and Estimation

MAP – Mean Apparent Propagator

FACT – Fiber Assignment by Continuous Tracking

ROI – Region Of Interest

FA – Fractional Anisotropy

GFA – Generalized Fractional Anisotropy

MD – Mean Diffusivity

υ_{ic} – Intracellular Volume Fraction

υ_{ec} – Extracellular Volume Fraction

ODI – Orientation Dispersion Index

RTOP – Return To Origin Probability

RTAP – Return To Axis Probability

RTPP – Return To Plane Probability

PA – Propagator Anisotropy

MSD – Mean Square Displacement

D – Axon Diameter

HCP – Human Connectome Project

TR – Repetition Time

TE – Echo Time

M1 – Primary Motor Cortex

SMA – Supplementary Motor Area

SC – Sensory Cortex

Thl – Thalamus

PM – Pre-Motor Area

Cau – Caudatus

Put – Putamen

GPi – Globus Pallidus

ANOVA – Analysis Of Variance

ROC - Receiver operating characteristic

AUC – Area Under the Curve

GFT – Graph Fourier Transform

rMEG – resting-state MEG

tMEG – task MEG

LIST OF FIGURES

LIST OF TABLES

1 Introduction

The human brain is one of the biggest and complex structures of the body. The cerebral cortex contains approximately from 15 to 30 billion neurons, and each one is connected by synapses to several thousand other neurons. These neurons communicate together with electrical train pulses carried along protoplasmic fibers called axons (presented in Figure 1.1). These axons can transfer information from one side of the brain to another far away with very long fibers, also more than 1 m in length.

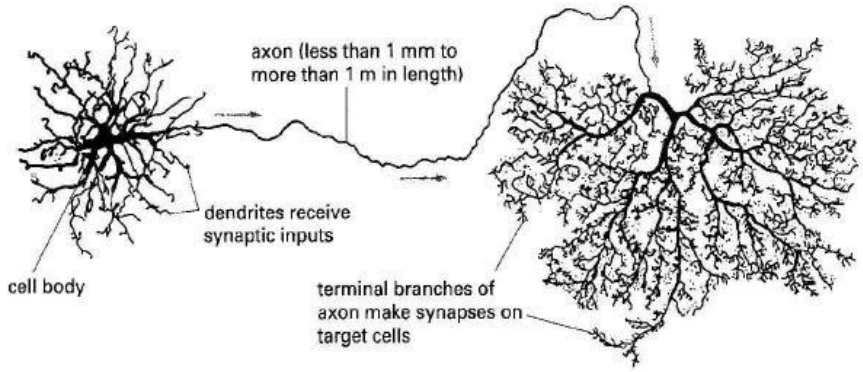

Figure 1.1: Neuronal system representation (with permission from B. Alberts et al., Molecular Biology of the Cell, Fourth Edition: Garland Science 2002, p. 1228).

An intrinsic multiscale architecture can be retrieved in the brain, defining different physical levels:

- Microscale (shown in Figure 1.2-A) is the level of single neurons and synapses (1μm resolution). It could be explored with electron microscopy, but the number of neurons comprising the brain easily ranges into the billions in more highly evolved organisms. The human cerebral cortex alone contains on the order of 10^{10} neurons linked by 10^{14} synaptic connections.
- Mesoscale (shown in Figure 1.2-B) is the level of neuronal group of populations (100μm resolution), which form local circuits that link hundreds or thousands of individual neurons. This scale can be explored with invasive techniques such as histological dissection and staining, degeneration methods, and axonal tracing.
- Macroscale (shown in Figure 1.2-C) is the level of anatomically distinct brain regions and inter-regional pathways (mm resolution), which can be explored with *in-vivo* imaging techniques such as the Computed axial

Tomography (CT), Optical Imaging (OI) and Magnetic Resonance Imaging (MRI).

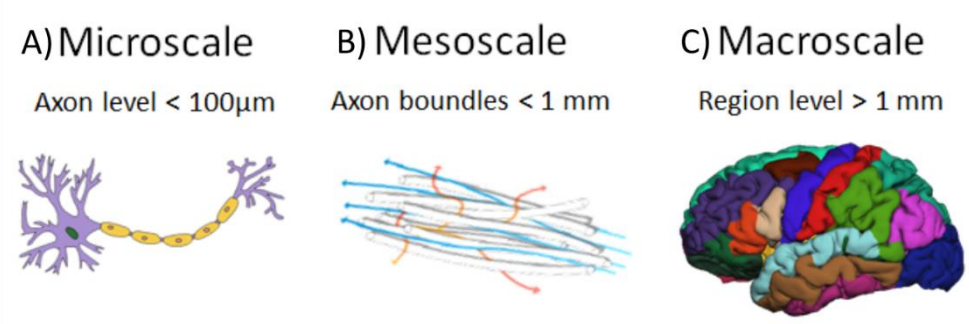

Figure 1.2: Example of different scales, from micro-scale (neurons) on left to meso- (groups of neurons) to macro-scale (cortical regions) on the right.

As shown, the brain is a complex and highly dynamic biological network, which has only been partially mapped to date. The intrinsic differentiation of the brain in scales allows neuroscientists to study at different levels the networks describing the dynamicity of this complex organ.

1.1 THE ERA OF HUMAN CONNECTOMICS

In neuroscience, the term "connectome" was introduced in 2005 to define the mapping of neural interactions within the brain. Inspired by the ongoing effort to sequence the human genetic code to build a so-called genome, two different scientists, Sporns [1] and Hagmann [2], suggested the term "connectome", simultaneously but independently, to refer to a map of the neural connections. Accordingly, the study of connectomes is known as connectomics, which might range from the detailed microscale of the full set of neurons and synapses within the nervous system of an organism (or part of it), to the macroscale description of the connectivity between bigger cortical and subcortical structures. The Hagmann declination of connectome was referred to the structural description of the human brains as a physical structure, but the brain is more than a physical set of tissues. Sporns had a more complex declination, defining different conceptualizations of the brain and consequently of the connectome (see Figure 1.3):

- **Structural connectivity** represents a physical network of connections, which may correspond to fiber pathways or individual synapses. It may

be investigated with patterns approaches, which include tract tracing and reconstruction of axon from serial sections of neural tissue [3]. Alternatively, diffusion imaging techniques yield probabilistic connection profiles, which are *in-vivo* estimations of structural connectivity at a specific spatial scale [4].

- **Functional connectivity** measures patterns of dynamic interactions among recording sites or brain parcels and investigates changes in these interactions during experimental perturbations [5]. It can be empirically measured as correlation/covariance between brain regions' signals which change over time. Different *in-vivo* techniques can acquire the functional signal from the scalp, such as Electro and Magneto Encephalography (EEG/MEG), or in the brain; e.g., functional MRI (fMRI).
- **Effective connectivity** describes causal effects of one neural system over another one [5]. This connectivity can be inferred from high temporal resolution data acquired through EEG/MEG, by performing sophisticated time series analysis.

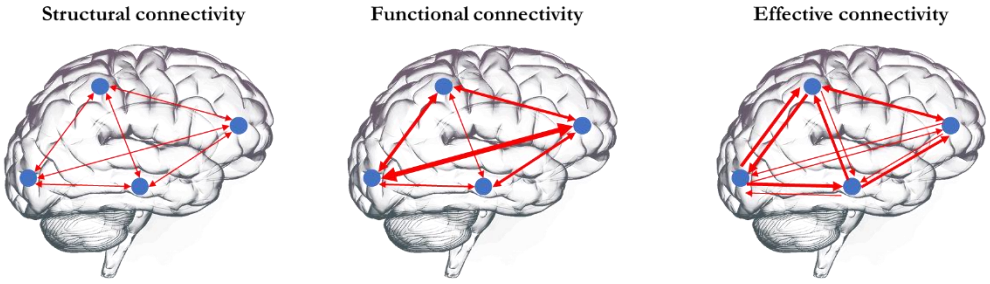

Figure 1.3: Illustration of structural, functional and effective brain connectivity and their difference in a graphical view.

A connectome defined at the microscale is feasible for species with relatively simple brains (for example C. elegans) and desirable given the valuable information it provides for single cell studies of development and physiology. However, for species with larger brains, remarkably humans, a definition of the connectome at micro- and meso-scales implies several considerable methodological and computational obstacles. For example, a reconstruction of high-resolution mammalian brain (1 mm^3) may generate on the order of a thousand terabytes of data. Reconstructing a whole human brain at such resolution would certainly exceed a million petabytes, a data set larger than all the written material in all the libraries of the world [6]. While methods for mapping the connectome at the microscale are still under development,

numerous established empirical approaches based on modern neuroimaging techniques allow nowadays the construction of connectome data sets at the level of macroscopic connectivity.

1.2 MODERN NEUROIMAGING TECHNIQUES

The macro-scale connectivity can be estimated from different signals acquired with different imaging modalities. We can distinguish between two main categories based on the signal which is acquired:

- Structural imaging, which permit to investigate the structure of the nervous system;
- Functional imaging, which is used to define the activity of the brain and therefore the synchronization or desynchronization of regions.

The modern set of neuroimaging techniques is composed by non-invasive methods that allow estimating structural and functional signals, such as Magnetic resonance imaging for both structure and function and Encephalography for the functional signal. More details will follow in the next paragraphs about these techniques.

1.2.1 Magnetic resonance imaging

Magnetic Resonance Imaging (MRI) is a modern medical imaging technique that uses strong magnetic fields and radio waves to generate images of the different tissues in the body. MRI is largely used in clinical medical diagnosis, thanks to its ability of defining the different stages of disease and follow-up non-invasively; i.e., avoiding radiation exposure. On the other hand, MRI scans are typically longer and louder compared to computer tomography (CT), and need the subject to enter in a narrow and constringing tube, which might cause issues in case of claustrophobia. Moreover, subjects with medical implants or non-removable metal objects inside the body cannot enter the MRI scanner.

The signal is measured from a receiving coil, which acquires a radio frequency signal emitted by excited hydrogen atoms inside the body, after the application of a temporarily oscillating magnetic field at the appropriate resonance frequency.

Changing the frequency signal applied to the acquisition, images with different contrasts can be acquired, making MRI a versatile and useful tool for a large spectrum of applications. For example, in the application to the brain, the T1-weighted contrast permits to reconstruct an image with appreciable anatomical detail and differentiate really well different brain tissues, i.e., white matter, gray matter and cerebrospinal fluid. Instead, the blood-oxygen-level dependent (BOLD) contrast [7] on which functional MRI (fMRI) is based, detects changes associated to blood flow, that can be brought back to brain activity. Alternatively, diffusion-weighted MRI (DW-MRI) measures the Brownian motion of water molecules inside the body, acquiring the energy response of several spatially-varying magnetic fields (i.e., gradients) applied in different directions [8]. We will detail in the next paragraph the main principles of DW-MRI processing in order to investigate structural connectivity.

1.2.2 Advanced diffusion-weighted MRI to build structural connectomes

Theoretically, DW-MRI acquisitions with three gradient directions are sufficient to estimate a three-dimensional diffusion profile, represented by a simple diffusion tensor [9]. However, this representation is unable to characterize complex architectures, such as crossing, kissing or fanning between fiber bundles, that require more than one tensor to be correctly reconstructed. In the last years, advanced DW-MRI techniques were developed in order to avoid this limitation, employing more diffusion gradients and opening the possibility to use sophisticated mathematical models to better estimate the white matter axonal pathways, even in presence of complex architectures. The estimation of the axonal pathways, generally called fibers, allows to virtually reconstructing axonal connections between all voxels in the brain. Structural connectomes can then be derived by quantifying the presence of connections between pairs of brain parcels, generally derived from standard atlases. Multiple metrics of connectivity can be used, such as the number of connections (i.e., the number of reconstructed fibers in the bundle), the mean length of the connection or metrics describing the microstructural properties of bundles, such as fractional anisotropy (FA, more detail in Chapter 2). In the last few years, the usage of microstructural properties to weigh the structural connectivity has become popular,

for example Falcon and colleagues proposed the use of FA normalized with the number of fibers for each connection as connectivity metric [10]. This allows for a more precise connectivity model, informed with microstructural properties of the network, which might be particularly useful in clinical applications, where a deterioration of these properties is often found. Extensive details about structural connectivity measures and methods will be given in Chapter 2/3.

1.2.3 Encephalography and source imaging to obtain functional connectomes

Both Electroencephalography (EEG) and magnetoencephalography (MEG) localize neural electrical activity with extracranial recordings. They measure, respectively, electric potential differences and weak magnetic fields that are generated by the electric activity of the neural cells. When a neuron is excited, it produces excitatory postsynaptic potentials at the level of the apical dendritic tree, producing a potential difference between the soma cell and the basal dendrites and the apical dendritic tree. This potential difference causes a current that flows from the non-excited soma and the basal dendrites to the apical tree. There are two different types of currents: the primary and the secondary one, which are related to intracellular and extracellular currents, respectively. EEG and MEG differentiate from each other by the sensitivity to the effects of primary and secondary currents. In details, MEG is more sensitive to the primary currents respect to EEG, which is extremely sensitive to the effects of the secondary currents [11]. Both EEG and MEG are acquired from the scalp, therefore a source localization approach is required to reconstruct the activation of the brain. The source localization process is a two-step method that solves two problems.

The first step is related to the forward problem, which map the propagation from the neural sources to the EEG electrodes and/or the MEG SQUID on the scalp. It can be formulated as:

$$\hat{Y}_t = GX_t$$

where $\hat{Y}_t = [y_{1,t}, y_{2,t}, \dots, y_{N_E,t}]$ represents the observations in the N_E channels at time t, $X_t = [x_{1,t}, x_{2,t}, \dots, x_{N_S,t}]$ represents the signals of N_S dipole sources at time t

and G is the solution of the forward problem. The forward problem needs to first estimate the volume conductor that model the conductivity between brain and scalp. The important aspects to configure the volume conductor are the geometry of the head, the tissue conductivities and the electrodes/magnetometers placement respect to the head. Starting from the geometry of the head, different types of geometrical model exist in literature. The simplest model is based on one or three/four concentric spheres that represent the different tissues of the head, such as the scalp, the brain matter and the liquid between scalp and brain. This spherical approach is enough for most EEG/MEG numerical solutions. However, the head is not spherical, and the localization of the deep sources requires a realistic shape for the head volume conductor [12]. The realistic models are more accurate, improving the dipole localization of few centimetres [13] [14] [15]. The models based on a realistic shape utilized different imaging modalities, such as the T1-weighted MRI or the CT. Some examples of realistic geometry models are the Boundary Element Method (BEM) or the Finite Element Method (FEM), which approximate head shape better than the spherical model, but with a computational complexity. The second requirement for the forward problem is the electrical characteristics of biological tissues, which are inhomogeneous, anisotropic, dispersive, and nonlinear. Head tissues such as the skull, scalp, muscles, cerebrospinal fluid, grey and white matter have different conductivities σ, permittivity ε, and magnetic permeabilities μ. The skull as well as the scalp shows a multilayer structure, which presents different electrical properties. The multilayer modelling is a possible solution to describe the geometry of the tissue [16]. Another possibility attribute inhomogeneous properties to the tissue, assigning different tensors of conductivity $\sigma = \sigma(x, y, z)$ and permittivity $\varepsilon = \varepsilon(x, y, z)$ on each triangular elements of the brain surface mesh. These conductivity values influence the forward problems and the inverse solution. Consequently, it is critical to assign proper and accurate conductivity values of an individual's head. As reported in literature, an average value can be extrapolated from electrical property ranges for most head tissues in terms of conductivity σ and permittivity ε [12] [17] [18] [19] [20]. Using the average values may result in inaccurate solutions due to a function of position [21] or of age [22]. However, some studies have shown that the usage of approximated conductivities is reasonable if combined with an accurate geometrical description of the head (i.e. based on a

subject's T1-weighted or CT images) [23]. In order to determine the electrodes/magnetometers placement respect to the head two different systems are used. In EEG some reference points may be acquired respect to a fix reference system in order to reconstruct the brain in space and perfectly overlap the electrodes over the scalp reference system. Generally, three points are required for the head. These points are the nasion (intersection of the frontal bone and the two nasal bones) and the two tragu (small pointed eminence of the external ear). Moreover, the coordinates of all electrodes may be acquired to have the position of the cap on the head. In case of MEG, the magnetometers are fix in space. Consequently, only three reference points (nasion and two tragus) are acquired as coordinates respect to the centre of the magnetic coil. After the reconstruction of the brain reference system with the setup of the sources and their relationship with the electrodes, the Maxwell's equations are solved to extract the linear operator G, which links the conduction of the different layers from the scalp to the brain. The leadfield matrix G is a matrix in which each source point is described as a combination of N_E fields.

The second step of the source localization is related to the inverse problem, which defines the relationship between the source in the brain and the electric or magnetic field acquired on the scalp. The inverse problem is formulated as:

$$X_t = G^{-1}Y_t + \upsilon_t$$

where $X_t = [x_{1,t}, x_{2,t}, \dots, x_{N_S,t}]$ represents the solution of N_S sources at time t, $Y_t = [y_{1,t}, y_{2,t}, \dots, y_{N_E,t}]$ represents the observations in the N_E channels at time t, G is the leadfield matrix estimate with the forward problem and υ_t is the added noise, generally modelled as a Gaussian vector [24]. The estimation of the location and the strengths of the N_S sources is essentially an ill-posed problem due to the infinite number of possible solutions. For this reason, different inverse modelling approaches exist as particular inverse solutions. The earliest and most straightforward strategy is to fix the number of sources and use a nonlinear estimation algorithm to minimize the squared error between the data and the fields, calculating the Frobenius norm of the residual [11] [25] [26]:

$$\min_s \left\| Y - \hat{Y} \right\|_F^2$$

where s refers to all the dipole sources as a set of positions r_i and orientations θ_i; Y is the set of EEG/MEG signals, and $\hat{Y} = GX$ is the estimated signals from the

leadfield matrix G and the set of dipole sources X derived by the inverse problem. This model represents only one of the models present in literature, but it will be the model used in this thesis, referring as Minimum Norm Estimation (MNE).

1.2.4 Multimodal approaches for connectomics

A relationship between different types of connectomes (anatomical, functional, effective) is expected to exist, because they represent the results of different probes of the same network, the brain. The investigation of this relationship still represents a significant challenge to present-day and has been the focus several works in the field in the last decade. The application of graph network analysis allows the comparison of brain connectivity patterns obtained from different connectivity modalities. For example, the discovery of small-world attributes in functional connectivity patterns derived from fMRI, EEG and MEG studies raises the question of how closely functional connections map onto structural connections. An emerging view suggests that structural connection patterns are indeed major constraints for the dynamics of cortical circuits and systems, which are captured by functional and effective connectivity. In addition to the constraining influence of structural connections, rapid temporal fluctuations in functional or effective connectivity may reflect additional changes in physiological variables or input. Given these links between structural and functional connectivity, it is likely that at least some structural characteristics of brain regions are reflected in their functional interactions. For example, structural hub regions should maintain a large numbers of functional relations. A computational model of the large-scale structure of cerebral cortex [27] suggested a partial correspondence between structural and functional hubs even at very short time scales. Moreover, Honey et al [28] tried a predicting approach of resting-state functional connectivity from structural one, using distance and indirect anatomical connections to mediate the relationship between connectivities. Then, van den Heuvel and colleagues proved the presence of a link between resting state networks (RSNs) and structural architecture, demonstrating the existence of structural white matter connections between the functionally linked regions of RSNs [29]. After that, in 2012 Bowman et al [30] proposed a cluster analysis with a novel

distance measure to underlie the importance of structural connectivity to supplement the functional MRI data. They described the combined functional-structure dissimilarity measure to infer their anatomically-weighted functional connectivity (awFC). Finally, in 2015 Falcon and colleagues used a novel application, i.e. The Virtual Brain (TVB), which uses Fractional Anisotropy (FA) weighted for number of streamlines in combination with lengths of individual connections, to simulate the functional BOLD signal [10].

Recently, some studies explored the use of graph signal-processing (see par. 1,3 for extensive details), which generalizes basic operations of signal processing to graphs, to combine functional and structural data [31] [32]. The Graph Fourier Transform (GFT) associated with spectral filtering operations, for instance, allows for the decomposition of the functional signal into a portion that aligns tightly to the structural backbone of connectivity, and a portion which detached from that. Medaglia and colleagues interestingly showed how measures of alignment/liberality of functional connectivity respect to the white matter structure are indeed subject-specific and relate to individual scores of cognitive flexibilities. However, this study is limited to the exploration of functional signals with fMRI. A recent study [33] demonstrates that estimations from structural networks were more accurate when predicting MEG networks on both individual and group levels than when predicting fMRI networks. This justifies the need of new approaches integrating structural connectivity with functional signals derived from electroencephalography.

1.3 GRAPH THEORY AND GRAPH SIGNAL PROCESSING

Many data in the world reflect underlying complex structure as, for example, the brain. Network modelling using graphs is offering the ability to address this complexity. The graph perspective can be naturally used for whole-brain "connectomics", where the graph $G = \langle V, E \rangle$ is identified with a set of nodes V as parcels of brain and the edges E are the structural or functional links between parcels. The edge weights can be binarized or weighted. At the beginning, graph theory was used first in functional connectivity studies [34], but in the past few years this kind of approach has also been applied to structural studies [35]. In particular, Falcon and colleagues presented a connectivity analysis applying graph theory on a

weighted structural graph with quantitative standard microstructural properties (FA values) normalized by the number of fibers [10]. Graph theory then allows estimating graph-theoretical local or global measures that summarize the topological structure. For instance, assortative measures, distance measures, motifs measures, centrality measures, efficiency measures and many other can be estimated for each node [36]. In many cases, these estimations are used to compare different graphs, finding similarity and differences between them. For example, the Laplacian matrix can be used to find many useful properties of a graph. Given a graph G, its Laplacian matrix L is defined as:

$$L = D - A$$

where D is the degree matrix and A is the adjacency matrix of the graph. This graph Laplacian has some interesting properties (i.e, symmetric and diagonally dominant, positive-semidefinite [$\lambda_i \geq 0$, for all i] ecc.) that makes it a powerful representation also for complex graphs.

The introduction of graph signal processing permits to approach the analysis of the graph with a different perspective. It represents a powerful tool for the representation, processing and analysis of complex graphs [37]. The Graph Fourier Transform (GFT) is one of the main graph signal processing tools, which define a Fourier transform in a graph. Specifically, an analogy can be described with the classical Fourier transform of a function f in terms of the complex exponentials:

$$\hat{\mathrm{f}}(\xi) \coloneqq \langle \mathrm{f}, \mathrm{e}^{2\pi \mathrm{i} \xi \mathrm{t}} \rangle = \int_{\mathbb{R}} f(t) e^{-2\pi i \xi t} \, \mathrm{dt}$$

where it can be observed that the Fourier kernel is also an eigenfunction of the derivative operator. Therefore, the GFT $\hat{f}$ of a graph signal $f \in \mathbb{R}^N$ associated to the vertices of a graph $\mathcal{G}$ can be defined in terms of the eigenvectors of the graph Laplacian:

$$\hat{f}(\lambda_\ell) \coloneqq \langle f, u_\ell \rangle = \sum_{i=1}^{N} f(i) u_\ell^*(i)$$

Then, similar notions of frequencies and frequency components are provided by Laplacian eigenvalues and eigenvectors, respectively [37]. Connected graphs present a constant Laplacian eigenvector u_0 associated with the eigenvalue 0, which has the constant value $1/\sqrt{N}$ in each vertex. Moreover, the graph Laplacian eigenvectors

associated with low frequencies λ_ℓ vary slowly across the graph, while the ones associated with larger eigenvalues oscillate more rapidly.

1.4 OPEN CHALLENGES

Advanced connectivity model. Validation of connectivity models is nowadays one of the most important question. Indeed, the fibers represent only an estimation of the axonal pathways, and there are a lot of different signal reconstruction model that can result on different accuracy on the reconstruction of the main directions in each voxel. Moreover, the spatial concept of the connectivity might change choosing different parcellation, and there are a lot of different atlases based on the function or on the cytoarchitecture or simply based on particles subdivision. No solutions are currently available to validate the entire connectome. Partial validation based on histology can be performed for the structural part and the use of phantoms and synthetic data is of help, but a clear way to identify the accuracy of the structural connectivity at the global level is still missing.

Advanced weighting model. Although the most used structural connectivity is the binary one, Falcon and colleagues [10] open the issues of using some informative properties in the connectivity. Recently, the proliferation of reconstruction models has been followed by a proliferation of new diffusion indices, which can be more informative respect to a measure of the anisotropy. These new generation microstructural indices are just presented in the literature and no assessment in clinical application is present in the state-of-art. Moreover, the assessment and usability of more informative techniques in the connectivity model is not explored yet.

Function/structure link. The state-of-art about the multimodal approaches presents some examples of integration between structure and function, but does not appear fully explored yet. The adoption of multimodal techniques is important to increase the knowledge of brain mapping. Almost all approaches presented above investigates the link between static connectivities, which is the simplest case. But, as already described, the brain is a complex high dynamic biological network and some

studies suggested that the correspondence between structure and function is only partial. Graph signal processing opens new interesting possibilities to integrate the information of structure and function with a dynamic point of view. Recent results on this topic are encouraging, but many aspects of this methodology still need to be extended and refined. Medaglia and colleagues [31] limited their study to brain activation signals derived from fMRI, while using different modalities with higher temporal resolution would lead to new interesting explorations. Moreover, they selected manually the cut-off for signal filtering; i.e., the number of components to derive the subdivision in aligned and liberal signals. Identifying a criterium to optimally define the filtering cut-offs would generalize the method and make it more stable and insensitive to arbitrary choices.

1.5 CONTRIBUTION OF THIS WORK

The goal of this thesis is first to assess and reduce the uncertainty embedded in the structural connectome estimation pipeline in such a way that the resulting model is neuroanatomically and neurophysiologically plausible, as well as maximally precise and reliable. Second, to introduce a novel multimodality approach allowing to dynamically integrate structure and function. In detail, we can therefore identify two main sections of the work, covering:

1. Quantification and modelling of the impact of each step in the pipeline for structural connectivity estimation. This implies the investigation of the methods and parameters of each step (from the acquisition scheme, to signal reconstruction, to microstructure measures, to connectivity matrices and graphs).

2. Investigation and modelling of the link between structural and dynamic functional connectivity to get to a holistic self-consistent anatomically and functionally plausible link over time.

In this thesis, the estimation of the structural connectivity is evaluated from different points of view. First, a preliminary assessment of the recently proposed

microstructural properties is presented in the specific clinical application of stroke, one of the most diffused neurological diseases. This allows evaluating the importance of considering these new sets of properties based on advanced DW-MRI methods, which add complexity to the model and require longer time for acquisition and signal reconstruction analysis. Second, the reproducibility of the structural connectivity is estimated using different methods to reconstruct the fibers, showing the importance of choosing the optimal model to solve complex architectures. In this step, the inclusion of the microstructural properties is also evaluated through their reproducibility in the whole connectivity. Third, the combination that presents the best reproducibility is used to obtain the structural connectome, and a new method to integrate this with dynamic functional connectivity is introduced.

In details, **Chapter 2** of this thesis presents an overview of the state-of-the-art methods of structural connectivity estimation, describing different fiber reconstruction models and the assessment of fiber properties that can be used as biomarker.

Chapter 3 shows the work I performed to assess some recently proposed indices. We start from simple focalized connections, driven by the idea to study loops and restricted networks related to the impairments caused by a focalized lesion. Then, whole-brain structural connectivity analysis is applied, using two different approaches: graph theory and machine learning.

In **Chapter 4**, I introduce a paradigm that allows answering to the reproducibility question of the different methods. A possible good tractography eaxtraction model that better represents the stability across healthy subjects is defined in combination with the best properties.

Finally, **Chapter 5** describes a new model that integrates the structural connectivity and functional signals, derived from encephalography. The graph signal processing framework is adopted and allows to analyse the dynamics of functional signals, while considering their structural backbone underneath.

Limitations and future perspectives of my work are then summarized and discussed in **Chapter 6**.

2 STRUCTURAL CONNECTIVITY FROM MESO- TO MICRO-SCALE

Diffusion Imaging is an *in-vivo* technique that allows mapping the white matter fibers estimating the path of the axons. In this Chapter the main steps to map the white matter fibers are presented. The main steps include:

1. Acquisition of diffusion signal;
2. Signal reconstruction;
3. Microstructural computation;
4. White matter fibers estimation (tractography);
5. Parcellation definition;
6. Connectivity extraction.

2.1 ACQUISITION OF DWI-MRI

The most common way to measure diffusion inside a tissue is using diffusion Magnetic Resonance pulses. The most common pulse is called Pulsed Gradient Spin Echo (PGSE). The latter was invented by Stejskal and Tanner [38]. The PGSE is defined by two gradients with strength G and duration δ, separated by the time Δ. The main idea is to measure the Brownian movement of the water molecules principally represented as a rotational energy state also called spin. The first gradient is applied after a 90 degree Radio Frequency (RF) spin-echo pulse and the second one after a 180 degree RF pulse. The first pulse takes the spin in the plane transverse to the main magnetization direction. After the time Δ the 180 degree pulse is applied refocusing the spins, which inverts the magnetisation vectors. This refocus is perfect only if the water molecules and their corresponding spins have not moved along the direction in which G is applied. If the water molecules have indeed diffused, the refocus is not perfect and the detected signal is smaller than the one that would be originated from static molecules. In order to quantify this signal loss, it is generally necessary to acquire the signal without any diffusion gradient ($G = 0$). This acquisition allows obtaining the reference signal, which only depends on the amount of spins in the voxel (b0 image). The amplitude of the detected diffusion signal depends on four factors: the direction of the diffusion gradient $\mathbf{u}$, the gradient strength G, the pulse width δ, and the pulse separation time Δ.

In literature, the diffusion signal S is generally expressed as a function of the so-called q-value:

$$q = \frac{\gamma \delta \mathbf{G}}{2\pi}$$

with $\mathbf{G} = G\mathbf{u}$, and the water gyromagnetic ratio γ, corresponding to $2.67513 \cdot 10^8$ T/s. The effective diffusion time τ can be calculated as $\Delta - \delta/3$ and consequently the b-value can be formulated as:

$$b = 4\pi^2 \tau q^2 = \gamma^2 G^2 \delta^2 (\Delta - \delta/3)$$

which is measured in s/mm^2.

Using the PGSE sequence at a certain b-value it is possible to obtain a snapshot of the diffusion process in a given direction, and the name of this technique is Diffusion Weighted Imaging (DWI). The number of gradients and b-values used to acquire DWIs is limited by two factors. One is the acquisition time, which increases with the number of directions acquired. The second is the maximal b-value obtainable by the scanner, which depends also on the maximal gradient strength G_{max}. The most common diffusion weighted acquisition scheme is composed of multiple gradients acquired at the same b-values but in multiple directions that are spread uniformly on the surface of a sphere, which is called "shell" (example schema in Figure 2.1-A). If the number of diffusion directions is high (typically over 60 diffusion directions) the acquisition is considered suitable for the High Angular Resolution Diffusion Imaging (HARDI) techniques. Acquisition presenting gradient spread on the surface of the sphere, but with multiple b-values, are called multi-shell and are suitable for advanced reconstruction models (example schema in Figure 2.1-B). Another type of DW acquisition is the Cartesian grid acquisition scheme in which the three-dimensional q-space is sampled uniformly in a cube or a sphere of a certain radius that is called Diffusion Spectrum Imaging (DSI) (example schema in Figure 2.1-C).

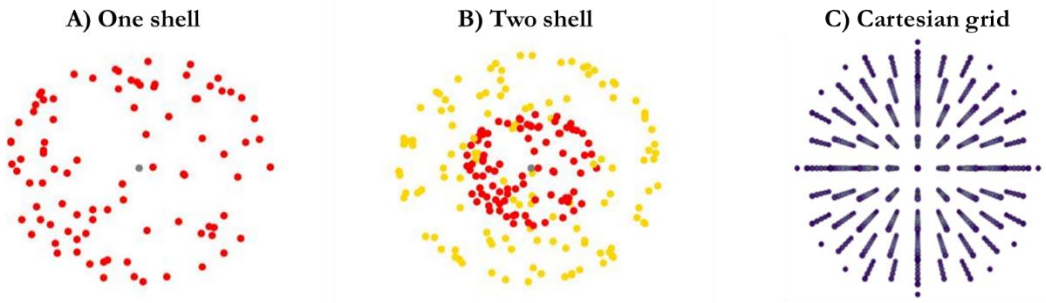

Figure 2.1: example of different acquisition schemas in the q-space

2.2 SIGNAL RECONSTRUCTION IN DW-MRI

The diffusion signal characterizes the tissue diffusion pattern, modelling the signal with mathematical approaches. Nevertheless, there are a lot of different models to recover the complexity of the brain tissue, which can be subdivided into three main categories, according to the characteristics of the models: the *Propagator models*; the *Fiber Orientation models*; and the *Compartmental models*.

2.2.1 Propagator models

The main goal for the *Propagator models* is the reconstruction of the Ensemble Average Propagator (EAP) from the diffusion signal, which represents the probability function of water molecules displacement in each direction:

$$P(r) = \int_{q \in R^3} E(q) e^{-2\pi i q \cdot r} \, dq$$

where P(**r**) is linked to diffusion signal E(**q**) =S(**q**)/S_0 by an inverse Fourier relationship. The simplest model is the most popular Diffusion Tensor Imaging (DTI). It was proposed by Basser and colleagues [9] modelling the signal attenuation in the voxels as a multivariate Gaussian function. The mathematical expression for the signal was the following

$$E(q) = \exp(-4\pi^2 \Delta q^T \mathbf{D} q)$$

where D represents the diffusivities along the three directions on the diagonal elements, while the other elements correspond to the correlation between displacements along those orthogonal axes. To estimate this model an acquisition of six directions is sufficient, making the total acquisition time very short. The ODF is modelled as a single tensor which is clearly inadequate in voxels containing complex fibers architectures like crossing, fanning and kissing [39] [40] [41].

2.2.2 ODF driven reconstruction model

Conversely, the main objective of the *Fiber Orientation models* is to reconstruct the directionalities, in order to solve the problem of complex architectures, reconstructing more than one main direction per voxel. The most popular model is

the Spherical Deconvolution (SD), proposed by Tournier, in 2004 [42]. The SD describe the signal as the result of a convolution operation between the expected true fiber distribution and the response function produced by a single fiber, as shown in Figure 2.2 on the first row. Consequently, the expected fiber distribution, defined as fiber ODF (fODF), can be derived performing the inverse operation, the deconvolution between the measured diffusion signal profile and the response function (single fiber) as shown on second row of Figure 2.2.

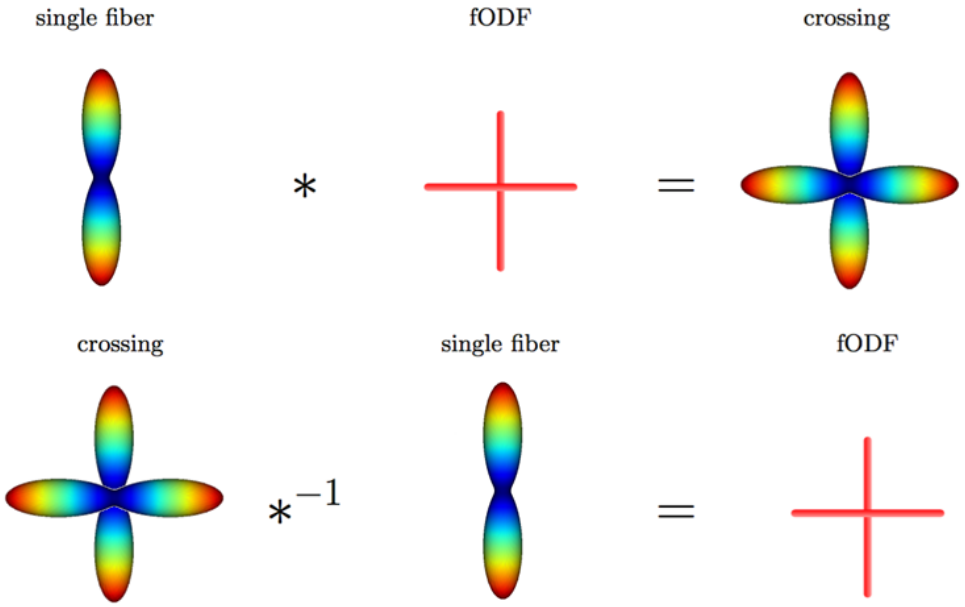

Figure 2.2: The convolution between single fiber propagation and a crossing orientation to obtain crossing propagation on first row, and the consequently deconvolution to obtain fiber ODF.

This method correctly recovers the crossing fiber configuration, but it suffers of deconvolution problems as ill-positioning and susceptibility to noise [42]. Besides, it needs to assume a priori the fiber response function, which might be realistic only in particular bundles in the human brain; e.g., the well-known corpus callosum offers a good chance to have a single fiber profile in the specific direction [43].

2.2.3 Compartmental models

The third and last class of models, the *Compartmental models,* focuses on microstructural properties and describes the signal as a composition of signals from different kind of tissues called compartments. The Neurite Orientation Dispersion

and Density Imaging (NODDI) model distinguishes three types of microstructural environments as compartments: the intra-cellular, the extra-cellular, and the cerebrospinal fluid [44]. The intracellular compartment refers to the space bounded by the membrane of neurites, the extra-cellular refers to the space around the neurites (show in Figure 2.3), and the isotropic refers to the space occupied by cerebrospinal fluid. Then, the signal is modelled as:

$$E = (1 - v_{iso})(v_{ic}E_{ic} + (1 - v_{ic})E_{ec}) + v_{iso}E_{iso}$$

where $v_{iso}$and E_{iso} are respectively the volume fraction and the signal associated with the cerebrospinal fluid, v_{ic} and E_{ic} are the same for the intra-cellular environment, and E_{ec} are for the extra-cellular environment.

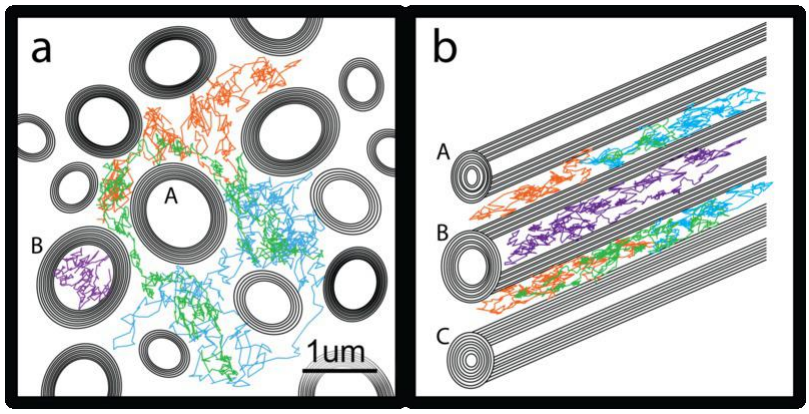

Figure 2.3: The intra and extra axonal spaces seen in a representation from the above (on the right) and from the side (on the left). (figure from [45], with permission of Dr. Kleinnijenhuis)

2.2.4 Advanced model for signal reconstruction

In the last few years some new advanced models were defined in order to solve the problems of the ODF shape describing the complex architecture of crossing/kissing. In details, two different new formalization of *Propagator models*, in which the reference frame changed, were introduced. The cartesian model called Simple Harmonic Oscillator based Reconstruction and Estimation (SHORE) [46] was firstly introduced by Özarslan. While, in 2013 he formulated the same approach in Cartesian coordinates calling the method Mean Apparent Propagator (MAP) MRI [47]. Moreover, in 2018 Zucchelli et al. [48] introduced a revisiting NODDI model that combine the constraint of the *Compartmental models* with the possibility to extract the fODF with a spherical harmonics (SH) encoding.

In SHORE the signal is defined as a combination of orthonormal functions, which consists of the solutions of the three-dimensional quantum mechanical harmonic oscillator. The formulation in spherical coordinates was introduced in mono-dimensionality by Özarslan [49] and generalized to the three-dimensional space [46]. The signal is defined as

$$E(qu) = \sum_{l=0,even}^{N_{max}} \sum_{n=l}^{(N_{max}+l)/2} \sum_{m=-l}^{l} c_{nlm}\, \Phi_{nlm}(qu)$$

where $N_{max}$is the maximal order of the functions in the truncated series and $\Phi_{nlm}(\mathbf{q})$ is the orthonormal SHORE basis. This family of functions is defined as

$$\Phi_{nlm}(qu) = \left[\frac{2(n-l)!}{\zeta^{3/2}\Gamma(n+3/2)}\right]^{1/2} \left(\frac{q^2}{\zeta}\right)^{l/2} \exp\left(\frac{-q^2}{2\zeta}\right) L_{n-l}^{l+1/2}\left(\frac{q^2}{\zeta}\right) Y_l^m(u)$$

where Γ is the Gamma function, $\zeta = \frac{1}{8\pi^2\tau D}$ is the scaling parameter [τ: diffusion time; D: diffusivity].

In MAP MRI the formulation can be obtained rotating the reference frame as

$$E(qu) = \sum_{N=0}^{N_{max}} \sum_{\{n_x,n_y,n_z\}} c_{n_x n_y n_z}\, \Phi_{n_x n_y n_z}(A, q)$$

where the basis functions are in the form

$$\Phi_{n_x n_y n_z}(A, q) = \Phi_{n_x}(u_x, q_x)\Phi_{n_y}(u_y, q_y)\Phi_{n_z}(u_z, q_z)$$

and $A = 2Dt_d$ is the covariance matrix of displacements [$\mathbf{D}$ is the diffusion tensor in the anatomical reference frame]. However, when comparing SHORE and MAP we can remark that the fiber crossing angle is underestimated by MAP when the angle is smaller than 90°, while SHORE does not resolve crossing smaller than 40°, as shown in Figure 2.4 [50].

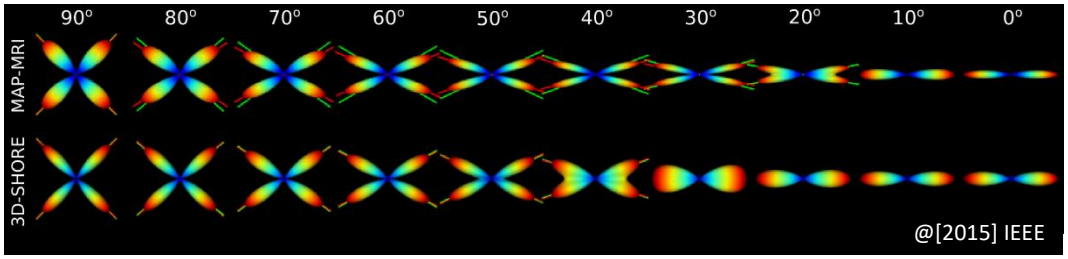

Figure 2.4: ODFS of a noiseless multi-tensor crossing obtained using MAPMRI and 3D-SHORE. When a crossing is detected, the ground truth and the estimated fiber directions are shown as green and red lines. MAP is able to resolve much smaller crossing angles than the other techniques, but also consistently underestimates the crossing angles smaller than 90°. (figure from [50])

Last year Zucchelli et al. [48] formalized an extension of the NODDI model. The model, called NODDI-SH, is basically a Spherical Mean Transform (SMT)-based extension of the NODDI model, providing a Spherical Harmonics (SH)-encoded fODF [51] and using the volume fractions to represent the local directionality spreading. The idea consists in plugging the three-compartments NODDI model in a signal reconstruction formula where the fODF is expressed by SHs. First, the neurite densities are recovered by the SMT. Then, SH coefficients are estimated by linear minimization [51]. Following the multi-shell SD scheme [51], the contribution to the diffusion signal from each compartment is obtained as the convolution of a single fiber response function $\mathrm{F(b,u,v)}$ times the fODF $\rho(\mathrm{v})$

$$\mathrm{E(b,u)} = \int_{\vec{\mathbf{v}}\in\mathcal{S}^2} F(b,\mathbf{u},\mathbf{v})\rho(\mathbf{v})\,\mathrm{dv}$$

where b is the b-value, $\mathbf{u}$ is a certain gradient direction, and $\mathbf{v}$ is a unit vector representing the considered fiber orientation. Replacing $\rho(\mathbf{v})$ with its representation using real symmetric SH $Y(\mathbf{v})$, the integral can be solved in closed form:

$$\mathrm{E(b,u)} = \sum_{\mathrm{l=0,even}}^{\mathrm{N}} \sum_{\mathrm{m=-l}}^{\mathrm{l}} \mathrm{c_{lm} f_l(b) Y_l^m(u)}$$

where N is the maximum harmonic order, and $f_l(b)$ are the projection coefficients of the single fiber response $F(b)$ onto the SH basis [52] [53] [51]. For a three-compartment model, $F(b)$ can be written as:

$$\mathrm{F(b,u,v)} = \mathrm{\nu_{ic} F_{ic}(b,u,v) + \nu_{ec} F_{ec}(b,u,v) + \nu_{csf} F_{csf}(b)}$$

where ν_{ic}, ν_{ec}, and ν_{csf} are respectively the relative volume fractions of the three compartments intra-cellular (ic), extra-cellular (ec) and CSF (csf) with the constraint $\mathrm{\nu_{ic} + \nu_{ec} + \nu_{csf} = 1}$. Note that the formulation of $F(b,\mathbf{u},\mathbf{v})$ is slightly different that the hierarchical formulation proposed in the original NODDI paper [44]. In order to link the two formulations, it is necessary to normalize the NODDI derived intracellular volume fraction by $\mathrm{1-\nu_{csf}}$, as in [54]. The Plugging-in of NODDI compartments into the equation $F(b,\mathbf{u},\mathbf{v})$ represent the intra-cellular compartment as a stick (or cylinder with zero radius) $\mathrm{F_{ic} = \exp\left(-b\lambda_{\parallel}\left(\overrightarrow{u^T v}\right)^2\right)}$, the extracellular signal as a Gaussian function $\mathrm{F_{ec} = \exp\left(-b\left[(\lambda_{\parallel}-\lambda_{\perp})\left(\overrightarrow{u^T v}\right)^2 + \lambda_{\perp}\right]\right)}$, and the CSF signal as an isotropic Gaussian, $\mathrm{F_{csf} = \exp(-b\,\lambda_{csf})}$. Moreover, the CSF

diffusivity is set to λ_{csf} =3 · 10^{-3} mm^2/s, the parallel diffusivities (intra and extra cellular) are assumed to be equal to $\lambda_{\parallel}$=1.7 · 10^{-3} mm^2/s and the extra-cellular perpendicular diffusivity depends on the parallel diffusivity and the volume fractions: $\lambda_{\perp} = \lambda_{\parallel} \frac{\nu_{ec}}{\nu_{ec}+\nu_{ic}}$. As mentioned above, the model parameters ν_{ic} and ν_{ec} (ν_{csf} and $\lambda_{\perp}$ are derived measures) were obtained using the SMT, as in [52] and [53].

2.3 EXTRACTION OF MICROSTRUCTURAL PROPERTIES

From all the described methods, microstructural measures that describe the brain tissues properties can be derived. We will describe them in the following.

2.3.1 Tensor Microstructure

The *Propagator models* provide a different kind of indirect measure related to microstructural properties. In the case of DTI, the tensor eigenvalues and eigenvectors can be directly linked to biological properties of the tissues

$$D = \lambda_1 v_1 v_1^T + \lambda_2 v_2 v_2^T + \lambda_3 v_3 v_3^T$$

where λ_i is the i^{th} biggest eigenvalue associated to the eigenvector v_i $(i = 1; 2; 3)$. The biggest eigenvector v_1 corresponds to the main diffusion direction in the tissue, which represents the average direction of axons in each voxel. The associated eigenvalue λ_1 represents the apparent diffusion coefficient of this principal diffusion direction.

Several microstructural indices based on the tensor eigenvalues have been proposed in literature, such as Fractional Anisotropy (FA), Mean Diffusivity (MD), Radial Diffusivity (RD), Axial Diffusivity (AD).

FA is a scalar value that describes the degree of anisotropy of the diffusion process. When FA equals 0, it means that diffusion is isotropic, while an FA value of 1 means that diffusion occurs only along one axis and is fully restricted along all other directions. In the DTI model, FA is calculated from the eigenvalues (λ_1, λ_2, λ_3) of the diffusion tensor following this formula [55]:

$$FA = \sqrt{\frac{1}{2}\frac{(\lambda_1 - \lambda_2)^2 + (\lambda_1 - \lambda_3)^2 + (\lambda_2 - \lambda_3)^2}{\lambda_1^2 + \lambda_2^2 + \lambda_3^2}}$$

The FA index is often graphically represented as a brain map with colours corresponding to the direction indicated by v_1 (colour FA). In this representation the colour red is associated with the x direction, green for y direction, and blue for z direction (example in Figure 2.5, which shows the maps of DTI FA and colour FA for a coronal slice of a healthy subject).

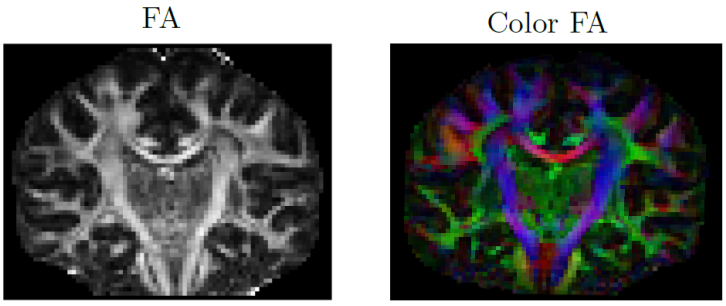

Figure 2.5: FA index (left) and FA colour (right) of a healthy subject in a coronal slice.

FA depends strictly on the structures present in the voxel: axons tubular shapes give high anisotropy (value > 0.5), the cell bodies in the cortex have an intermediate value since diffusion is generally more isotropic, and free displacement conditions (like in the cerebrospinal fluid) feature very low values expressing the fact that diffusion is perfectly isotropic (value =0).

FA was extended to the so-called Generalized Fractional Anisotropy (GFA), giving it the same relationship with the structure in the voxel. GFA is calculated as the standard deviation of the ODF sampled on a discrete sphere in N points divided by its quadratic mean:

$$GFA = \sqrt{\frac{N \sum_{i=1}^{N} (ODF(\mathbf{u}_i) - \overline{ODF})^2}{(N-1)\sum_{i=1}^{N} ODF(\mathbf{u}_i)^2}}$$

where ($\overline{ODF}$) is the arithmetical mean of the ODF [56].

Diffusivity measures are related to the total amount of diffusion in each voxel. While FA is a summary measure of microstructural integrity, the diffusivity properties reflect different features of the brain membrane. In details, Mean diffusivity (MD) is an inverse measure of the membrane density, formulating as the mean of the three largest eigenvalues:

$$\mathrm{MD} = \frac{\lambda_1 + \lambda_2 + \lambda_3}{3}$$

The other measures of diffusivity represent the relationship with the main direction, i.e the Axial Diffusivity (AD):

$$\mathrm{AD} = \lambda_1$$

and the mean of the other two directions, i.e the Radial Diffusivity (RD):

$$\mathrm{RD} = \frac{\lambda_2 + \lambda_3}{2}$$

These two measures are related to the dimension of the axons measuring the diffusion along the axons and in the perpendicular plane, respectively.

2.3.2 Compartmental Properties

The *Compartmental models* permit to derive the volume of each compartment describing the space as a contribution of balls and sticks in the case of NODDI model. This method allows to estimate some measures of the tissues, such as the intra-cellular (v_{ic}), the extra-cellular (v_{ec}) and the isotropic (v_{iso}) volume fraction plus an index called Orientation Dispersion Index (ODI).

The volume fraction represents a concentration of the compartment described in each voxel. Respectively, NODDI model allows the estimation of the following volume fraction measures:

- v_{ic} refers to the space bounded by the membrane of neurites, which are modelled as a set of sticks (i.e. cylinders of zero radius) to capture the highly restricted nature of diffusion perpendicular to axons and the unhindered diffusion along them.
- v_{ec} refers to the space around the axons, which is generally occupied by different types of glial cells or cell bodies. Here, the diffusion is hindered by the presence of the neurites, but it is not restricted. For this reason, this space is modelled as a simple anisotropic diffusion (Gaussian).
- v_{iso} represents the CSF component and its space, modelled as isotropic Gaussian diffusion.

At the beginning Zhang and colleagues [57] introduced a measure of the dispersion or fanning of the axonal fibers or dendrites, called ODI, simply defining the concentration parameter of the orientation distribution function κ. This measure was not intuitive because it mapped higher orientation dispersion with lower values. For this reason, in 2012, they redefined the ODI measure as:

$$\mathrm{ODI} = \frac{2}{\pi}\arctan(1/\kappa)$$

which ranges from 0 to 1, becoming more straightforward to visualize than κ [44].

2.3.3 Advanced Microstructural Properties

From the advanced *Propagator models* some new microstructural indices were recently introduced in the literature. These indices are the Return To the Origin Probability (RTOP), the Return To the Axis Probability (RTAP), and the Return To the Plane Probability (RTPP). They can be calculated in two ways, either from the signal or from the propagator. Other two microstructural properties were defined with SHORE and MAPMRI definition as Propagator Anisotropy (PA) and Mean Square Displacement (MSD); these kinds of measure are specific characterization of anisotropy components and water displacement in spherical harmonics equation.

RTOP is calculated as the volume integral of the signal or, alternately, following the properties of the Fourier transform, as the Ensemble Average Propagator (EAP) in zero:

$$\mathrm{RTOP} = \int_{R^3} \mathrm{E(q)}\ \mathrm{d}^{3}\mathrm{q} = \mathrm{P(0)}$$

RTOP corresponds to the probability that the water molecules do not move (or return to the starting point) during the time of the application of the two diffusion pulses of the gradient sequence (higher for more smaller cerebral tissues pores in WM). There are some conditions in which this index is the inverse of the apparent mean volume $\langle V \rangle$ of the pores inside the voxel:

- long diffusion time ($\Delta \ll \delta$);
- narrow pulse ($\delta \sim 0$).

Similarly, RTAP can be obtained either as the integral of the signal in the plane passing through the origin and perpendicular to the main diffusion direction, $q_\perp$, or as the integral of the EAP along the main diffusion direction $\overrightarrow{r_\parallel}$:

$$\mathrm{RTAP} = \int_{R^2} E(q_\perp)\, d^{2q_\perp} = \int_R P(\overrightarrow{r_\parallel})\, dr$$

RTAP represents the probability that the water molecules displacement is conned to the same axis during the diffusion pulses (higher for narrower pores). RTAP in long diffusion time and narrow pulse assumption is related to apparent mean cross-sectional area $\langle A \rangle$ of the pores inside the voxel as follow:

$$\mathrm{RTAP} = \frac{1}{\langle A \rangle}$$

RTPP can be obtained as the integral of the signal along the main diffusion direction or as the integral of the EAP over the plane passing through the origin and perpendicular to the main diffusion direction:

$$\mathrm{RTPP} = \int_R E(q_\parallel)\, d^{2q} = \int_{R^2} P(r_\perp)\, d^{2r_\perp}$$

RTPP is the orthogonal indices with respect to RTAP, expressing the probability that the water molecules displacement is conned to the same plane (higher for shorter pore). RTPP in long diffusion time and narrow pulse assumption is related to apparent mean cross-sectional length $\langle L \rangle$ of the pores inside the voxel as follow:

$$\mathrm{RTPP} = \frac{1}{\langle L \rangle}$$

PA could capture information that is unavailable in more traditional measures of anisotropy like FA. The idea of this index is to define the distance from the isotropic components:

$$\mathrm{PA} = \sqrt{1 - \frac{\sum_{n=0}^{(N_{max}/2)+1} c_{n00}^2}{\sum_{l=0,even}^{N_{max}} \sum_{m=-l}^{l} c_{nlm}^2}}$$

where c_{nlm} is the coefficients of SHORE and MAP models.

The MSD represents the mean square displacement of the water molecules in the unit time and is computed as follows:

$$MSD = \int_{R^3} P(\boldsymbol{r}) r^2 d^3\boldsymbol{r}$$

MSD has been proven to be closely related to the classical MD index, sharing similar patterns [58].

2.4 TRACTOGRAPHY

Following the principal diffusion directions in each voxels, it is possible to obtain a representation of the WM as "streamlines" [59] [60] [61]. These streamlines are a computer graphic representation of WM bundles which connect the different areas of the brain, although there is no guarantee that the streamlines correspond directly to fiber orientations, since they could also include false positives and negatives. The algorithms used to calculate the streamlines are called tractography algorithms [62]. Tractography algorithms reconstruct streamlines by following the principal diffusion direction in each voxel. This information is derived from the ODF which is dependent from the reconstruction model as described in the previous subsection. Stopping criteria of the reconstruction algorithm have to be introduced to define some rule which follows the anatomy of the brain, and these correspond usually two the following conditions:

- for an acute turning white matter tract, the connection of two neighbouring voxels would unlikely be formed at such a large turning angle;
- when the degree of isotropy is higher, tract tracing should stop because the voxel under examination is likely to contain mostly grey matter or the Cerebrospinal Fluid.

Moreover, tractograms can be evaluated depending on the solving of complex architectures like crossing, kissing and fanning. This depends on the adopted reconstruction model and consequently on ODFs. Several reconstruction models are available and they can be dived in two main categories: *Deterministic* and *Probabilistic* tractography (Figure 2.6 shows an example of two main categories).

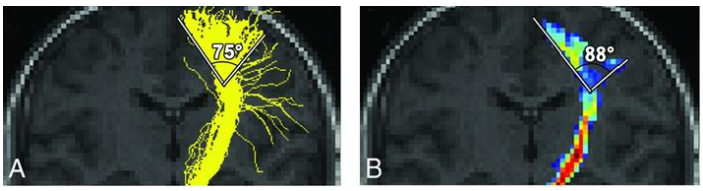

Figure 2.6: Depiction of the left descending motor pathways on example subject. Local deterministic (A), probabilistic (B) tractography are shown respectively to give an idea of their differences.

2.4.1 Deterministic algorithm

The most intuitive way to reconstruct a 3D trajectory from a 3D vector field is to propagate a line from a seed point by following the local vector orientation. However, if a line is propagated simply by connecting voxels, which are discrete entities, the vector information contained at each voxel may not be fully reflected in the propagation. The simplest way to convert the discrete voxel information into a continuous tracking line is to linearly propagate 'a line', in a continuous number field (see Figure 2.6-A as example). This linear propagation approach, which was called fiber assignment by continuous tracking (FACT), was used for the first successful tract reconstruction, which was accomplished for a fixed rat brain and showed good agreement with histological knowledge [63] [60]. This simple linear approach can be modified to create a smooth (curved) path, which should be more accurate when is permitted by the image resolution. Line propagation must be terminated at some point. The most intuitive termination criterion is the extent of anisotropy. In a low anisotropy region, such as grey matter (GM), there may not be a coherent tract orientation within a voxel and the orientation of the largest principal axis is more sensitive to noise errors (for isotropic diffusion, the anisotropy information is dominated by noise and becomes purely random). The disadvantage of local methods, particularly the FACT algorithm, is the accumulation of errors during the algorithm propagation. Most deterministic algorithms follow the principal orientation of diffusion, leading erroneous results, if there are fibers within a voxel running in different directions. In addition, fibers with a strong curvature may be difficult to reconstruct.

2.4.2 Probabilistic algorithm

Probabilistic tractography assesses the probability that a voxel is connected to a given starting point (seed), by means of iterative random walks. This method exploits the statistical nature of the information obtained by DWI and determines the most probable mathematic pathway. Figure 2.6-B shows an example of probabilistic tractography in which the colour from blue to red is scaled on the probability.

Probabilistic tractography is more robust than deterministic tractography in areas of high uncertainty (e.g., areas of high noise or fiber crossings).

2.5 PARCELLATION

Defining the nodes of a macroscale connectome is a complex task as we lack agreement on how best to define the constituent brain units. Depending on the goal of the investigation, the specific brain subunits represented by nodes can range from the small patches of cortex contained in individual MRI voxels to larger brain areas.

2.5.1 Voxel-based

The simplest approach is the using spatial unit (voxel) as Region of Interest (ROI). This approach permit to understand how well connected any given voxel is to the rest of the grey matter voxels in the brain [64] [65]. Though voxel-based nodes overcome the problem of defining and choosing ROIs, this represents a very complex problem in terms of space and in terms of visualization: a whole brain volume includes a number of voxels in the order 10^5 of magnitude.

2.5.2 Particles-based

Network nodes may be defined without reference to connection patterns, by defining spatial ROIs that partition the cortical surface. This approach generates homogeneous volume or spatial extent groups of voxels, defined particles. One drawback is the need to pre-specify the number of areas to be generated, which can be estimated based on homogeneity, accuracy, reproducibility or stability of the brain areas [66] [67].

2.5.3 Atlas-based

Architectural templates may be used to define anatomical regions that are aligned with macroscopic anatomical surface features (atlas-based parcellation). Although the large-scale human brain patterns captured using different strategies of parcelling data (gyral based atlas: ie, a gyrus was defined as running between the bottoms of two adjacent sulci; histological atlas: ie, post-mortem cyto- and myelo-architectonic segmentations; functional atlas: ie, reporting locations of activation foci in functional brain mapping) may bear a gross similarity to one another, the specific details conveyed vary substantially. Ideally, both brain function and structural information should be used to delineate brain areas allowing a clear definition of brain partition usable in both functional and structural connectivities that permit the easier interpretability of relationship records.

2.6 STRUCTURAL CONNECTOME: FROM TRACTOGRAPHY TO CONNECTIVITY

For the purpose of connectivity analysis, a mapping method is needed to summarize tractography, which contains about one million streamlines, in an object that can be analysed and compared across subjects or across cohorts, i.e., the structural connectome.

A structural connectome reflects the extent of connection between each pair ROIs, so it can be represented as a matrix with ROIs as entries of rows and columns, where each cell a_{ij} contains the number of fibers in the tractogram connecting ROIs *i* and *j*. A threshold *t* can be defined as minimum number of fibers to define the presence of a connection and permits to binarize the structural connectivity matrix as follows:

$$s_{ij} = \begin{cases} 0 & if \quad 0 \leq a_{ij} < t \\ 1 & if \quad a_{ij} \geq t \end{cases}$$

Moreover, in the last few years the way to compute structural connectivity started to change in literature, by including more informative properties than the number of reconstructed streamlines; e.g., the average length of fibers or their microstructural properties [10].

3 RELEVANCE OF MICROSTRUCTURAL PROPERTIES EXTRACTED FROM DW-MRI

Recently, new microstructural indices derived from advanced reconstruction models that require multi-shell acquisitions have been introduced in literature. This Chapter summarizes the work we performed to assess the validity of this new parameters as brain biomarkers in healthy subjects [Mendez, et al. 2016] and in stroke, from specific networks analysis [Brusini, et al. 2015, Brusini, et al. 2016; Boscolo, et al. 2017] to the whole connectivity [Obertino, et al. 2016 (PRNI); Obertino, et al. 2016 (OHBM)].

3.1 COMPARISON BETWEEN DIFFERENT INDEXES OF MICROSTRUCTURAL PROPERTIES

The compartment properties (ν_{ic}, ν_{ec}, ν_{iso}, ODI), presented in Chapter 2, have been recently suggested as specific markers of white matter abnormality in stroke disease [68], comparing them to the well-known tensor microstructural measures, conventionally adopted in literature as biomarkers [69]. The advanced *Propagator models*, instead, have never been used as a set of possible markers of white matter changes. In order to understand if these new set of properties capture meaningful microstructural information, a preliminary comparison between indices based on different reconstruction models was performed, scoring the indices with feature selection approach in healthy subjects [Mendez, et al. 2016]. I contribute to this work doing part of the analysis, writing the paper and preparing the presentation for the conference.

3.1.1 Methods

Three leading diffusion MRI models were selected: the compartmental NODDI model, and two advanced *Propagator models*, i.e the SHORE and the MAP. The information conveyed by the respective set of indices were analysed with some information-theoretic measures. The features, considered in this case as different microstructural properties, were selected progressively, one at a time in a greedy scheme, in which the i^{th} feature is selected by maximizing the objective function

Extended minimum Redundancy, Maximum Relevance (EmRMR) [70] which express the trade-off between relevance and redundancy.

A collection of *in-vivo* data were obtained from the Human Connectome Project (HCP) [71]. A total of nine subjects was considered in this work. The HCP acquisition scheme consists of nine b0 values and 90 diffusion gradients distributed on three different shells with b = 1000; 2000; 3000 s=mm^2. The diffusion HCP data have an isotropic spatial resolution of 1.25 mm. For each subject, a subset of the central image slices corresponding to the location of the ventricles was selected for voxel-wise analysis, amounting to an average of 3×10^4 voxels.

In order to assess the descriptive power of some different indices (ν_{ic}, ν_{iso}, ODI, RTAP, RTOP, RTPP, MSD and PA) in capturing microstructural features, a simple case was considered in which only three classes corresponding to white matter (WM), grey matter (GM) and cerebrospinal fluid (CSF) were present. Even though this is a fairly simple classification task, it allows a first ranking of the considered features according to the chosen criteria. To define the three different target labels, the masks selecting the three types of tissue provided by the HCP were used.

Given the input dataset $\mathbb{X}$ with a set of *n* features $\mathbb{X} = \{\mathrm{X}_1, \dots, \mathrm{X}_n\}$, labelled with a target class *C*, the classic feature selection problem consists in identifying a subspace which best characterizes *C* from the complete attribute space $\mathbb{R}^N$ [72]. One of the most famous methods for feature selection based on information theory, called minimum Redundancy Maximum Relevance (mRMR), was presented in [72]. According to mRMR, the features are selected progressively, one at a time in a greedy scheme in which the i^{th} feature is selected by maximizing the objective function expressing the trade-off between relevance and redundancy.

$$\max_{\mathrm{X_i} \in \mathbb{X}/\mathbb{S}} \{Rel(\mathrm{X_i}) - Red(\mathrm{X_i}|\mathbb{S})\}$$

where

$$Rel(\mathrm{X_i}) = \sum_{\mathrm{X_i},C} P(\mathrm{X_i}, C) log \frac{P(\mathrm{X_i}, C)}{P(\mathrm{X_i})P(C)}$$

$$Red(\mathrm{X_i}|\mathbb{S}) = \frac{1}{|\mathbb{S}|} \sum_{\mathrm{X_j} \in \mathbb{S}} I(\mathrm{X_i}; \mathrm{X_j})$$

In this work, the EmRMR objective function was used:

$$\max_{X_i \in X/\mathbb{S}} \left\{ I(X_i; C) - \alpha \sum_{X_j \in \mathbb{S}} \left[I(X_i; X_j) - I(X_i; X_j | C) \right] \right\}$$

where relevance $Rel(X_i)$ of a feature X_i is calculated as its mutual information $I(X_i; C)$ with the target class *C*, and α is a weighting factor used for casting the problem as extended quadratic programming and $I(X_i; X_j | C)$ is the conditional mutual information [73].

3.1.2 Results

The set of microstructural properties considered is composed by:

- the ν_{ic} and ν_{iso} volume fraction and the orientation dispersion index ODI for the compartmental NODDI model;
- the RTOP, RTAP, RTPP, MSD and PA from the SHORE model;
- the RTOP, RTAP, RTPP from MAP MRI.

The Relevance score and subsequently the EmRMR criterium was used to rank all the features according to the criterium of maximum relevance and minimum total redundancy. Given the EmRMR as an iterative selection procedure, it was also used to rank the features on each model individually. The procedure was repeated by performing bootstrap resampling 50 times per subject in order to obtain a more accurate distribution of the ranking and scores.

Figure 3.1-A shows the distribution of relevance scores calculated for the three target classes. The highest score was reached by MAP RTAP and RTOP followed by the same indices derived from SHORE and by PA. This highlights the prominence of the ability of SHORE-based descriptors in capturing microstructural features where diffusion is restricted.

Figure 3.1-B illustrates the results of the final selection by the EmRMR method, in which lower scores correspond to better ranking. SHORE RTAP, PA and MAP RTAP reach the best performance, reinforcing the leading role of these features as indicated by relevance analysis. RTOP in both MAP and SHORE has a slightly worse score consistent with the results of the previous analysis.

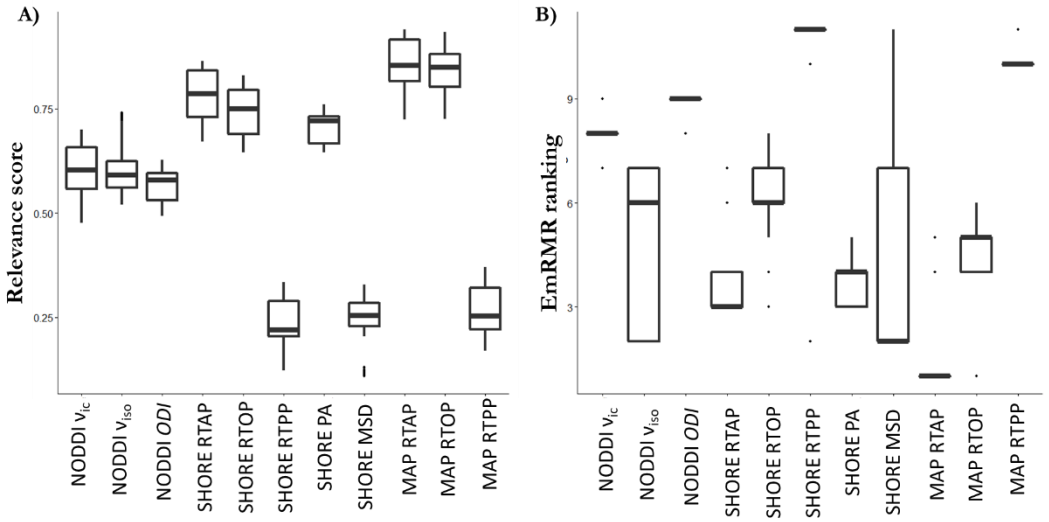

Figure 3.1: Relevance scores (Panel A) and EmRMR ranking (Panel B) on NODDI, SHORE and MAP MRI indices.

3.2 ASSESSMENT AND VALIDATION OF ADVANCED MICROSTRUCTURAL PROPERTIES IN MOTOR NETWORKS

Giving the better ranking of the advanced *Propagator models* respect to NODDI, the assessment of the diffusion indexes extracted from these reconstruction models was tested in a stroke population. The clinical dataset at the base of these preliminary works is composed by 10 stroke patients acquired in three different time points: within one week (*tp1*), one month (± one week, *tp2*), and six months (± fifteen days, *tp3*) after stroke; and ten healthy controls in two time points a month apart (*tp1c* and *tp2c*). All subjects underwent a DSI scans in each acquisition (Repetition time/Echo time [TR/TE] = 6600/138 msec, FOV = 212×212 mm, 34 slices, 2.2×2.2×3 mm^3 esolution, 258 gradient directions, b_{max} = 8000 s/mm^2). High-resolution 3D T1-weighted images were also included (TR/TE = 2300/3 msec, FOV = 256×256 mm^2, 160 slices, 1×1×1.2 mm^3 resolution, scan time = 6.13 min). Besides MRI acquisitions, patients underwent clinical neurological assessment following the National Institutes of Health Stroke Scale (NIHSS) at each tp. Only the motor part of the NIHSS score was retained for further analysis. Stroke volumes were derived from the individual high resolution T1-weighted images using the statistical parametric mapping (SPM) lesion segmentation toolbox

(www.fil.ion.ucl.ac.uk/spm/). The inclusion criteria, and the pre-processing of the data are described in [69].

In the following subchapters, a subsequent set of works are presented. Starting from a set of SHORE indexes, a qualitative analysis between cohorts was performed focusing on some motor connections [Brusini, et al. 2015]. While, in a second step the axonal remodelling was quantified in the uninjured motor cortical and subcortical networks [Brusini, et al. 2016], extending the set of microstructural properties [Boscolo, et al. 2017].

3.2.1 Clinical relevance of SHORE indices in motor-tracts

SHORE indices, including RTAP, PA and the Axon Diameter (D) in the form of $\mathrm{D} = \frac{2}{\pi}\,\mathrm{RTAP}$, were evaluated in the inter-callosal connections of the primary motor area (M1), the supplementary motor area (SMA), the somatosensory cortex (SC) and the thalamus (Thl). SHORE indices were compared with GFA, which previously provided evidence of plasticity in the uninjured motor network in stroke patients with motor deficits [69] [74]. The statistical significance of the difference between patients and controls was quantified, jointly with the analysis of the clinical status to predict motor outcomes [Brusini, et al. 2015]. My contribution to this work consisted in the pre-processing of the data, index extraction, help in designing the methods and writing of part of the paper.

3.2.1.1 Methods

For each microstructural index, the percentage absolute changes in mean values between time points were evaluated on both groups as:

$$\Delta_{\mathrm{tp12c}}(m) = |(m_{\mathrm{tp2c}} - m_{\mathrm{tp1c}})|/m_{\mathrm{tp1c}}$$

$$\Delta_{\mathrm{tp12}}(m) = |(m_{\mathrm{tp2}} - m_{\mathrm{tp1}})|/m_{\mathrm{tp1}}$$

$$\Delta_{\mathrm{tp23}}(m) = |(m_{\mathrm{tp3}} - m_{\mathrm{tp2}})|/m_{\mathrm{tp2}}$$

$$\Delta_{\mathrm{tp13}}(m) = |(m_{\mathrm{tp3}} - m_{\mathrm{tp1}})|/m_{\mathrm{tp1}}$$

where m denotes the mean value of the considered index along the fibers of a given connection, and the subscript c denotes the control group.

Normality test (Kolmogorov-Smirnov) revealed that the values were normally distributed enabling the use of parametric statistics. Accordingly, the unpaired t-test with $p < 0.05$ was performed to establish the significant differences between $\Delta_{tp12c}(m)$ and $\Delta_{tp12}(m)$. The predictive value of each metric was assessed by a linear regression model where the motor outcome at six months after stroke (*tp3*) was the dependent variable and the mean values of each index for all the connections at *tp1*, age, stroke size, and NIHSS motor scores at *tp1* and *tp2* were the predictors. A backward selection process was used to select the optimal predictor model with $p = 0.05$ as significance threshold.

3.2.1.2 Results

In controls, the reproducibility of the mean GFA, RTAP, D and PA values was confirmed by the t-test which showed no statistical significant difference between *tp1c* and *tp2c* ($p > 0.05$).

Figure illustrates the mean absolute percent changes of the different indices for patients and controls. For each index, the absolute changes between *tp1* and *tp2* in patients' connections were significantly different from the absolute changes between the same regions in controls between *tp1c* and *tp2c* ($0.01 \leq p \leq 0.05$).

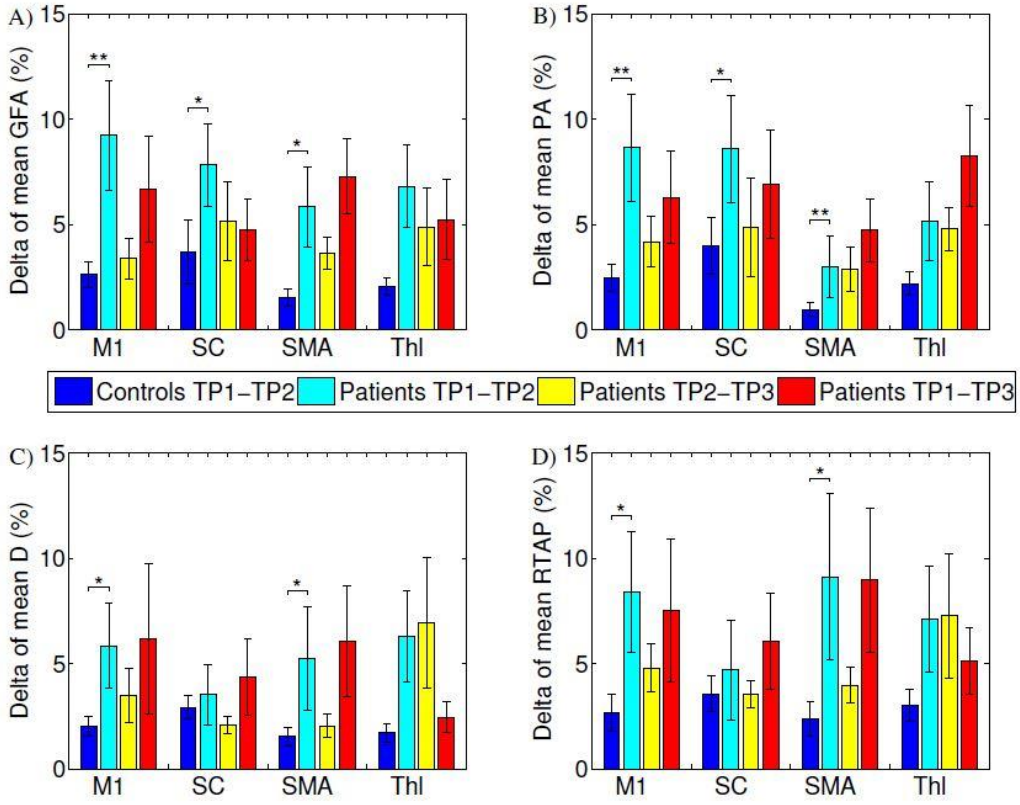

*Figure 3.2: Percent mean absolute longitudinal changes in controls and patients of (A) GFA, (B) PA, (C) D and (D) RTAP with the statistical differences (*p < 0.05, **p < 0.01).*

In the patients' group, a baseline linear regression model including only age and NIHSS at *tp1* and *tp2* gave low correlation as well as a model including only NIHSS at *tp1* and *tp2* (R^2 = 0.691; adjusted R^2 = 0.652). Conversely, for each index, the models including also its mean values across the different connections were able to predict the NIHSS at tp3 with higher significance (Table 3.1: Performance of each prediction model.).

Table 3.1: Performance of each prediction model.

Index	**Multiple R^2**	**Adjusted R^2**	**p-value**
GFA	0.970	0.932	0.004
RTAP	0.919	0.818	0.026
D	0.998	0.990	0.008
PA	0.991	0.973	0.004

The best prediction model was obtained with the axonal diameter D (adjusted R^2 = 0.99). However, all models led to high significance, with Adjusted $R^2 > 0.8$, confirming the importance of GFA and highlighting the relevance of SHORE indices for an early prediction of the patient clinical outcome. Moreover, although GFA and PA are both anisotropy indices, PA has a higher prediction significance pointing at a stronger reliability of this new descriptor.

3.2.2 Identifying group differences between patients and controls in WM networks and GM regions

Seeing that SHORE measures are relevant for some motor inter-callosal connections, the analysis was extended to a series of networks involved in different motor skills, which were identified with the help of neurologists. The analysis on cortical and subcortical tissues was extended to all SHORE indices, including RTOP, RTPP [Brusini, et al. 2016] and MSD, comparing the significance of both statistical analyses of group differences between patients and controls, and the longitudinal prediction in patients, with the results obtained with the simple tensor measures FA and MD [Boscolo, et al. 2017]. Moreover, the analysis was exploited for GM regions in order to reach the ability to detect the neuroplasticity due by the stroke impairment of advanced *Propagator models'* indices also in GM. For both contributions, my work focused on the main idea of using global WM networks instead only few connections. Then, I contributed to the idea of analysing the microstructural properties in the GM. I performed the evaluations of the weighted connections and region values, and I performed the analysis of both WM and GM, writing in particular the draft of the second paper.

3.2.2.1 Methods

The considered regions belong to M1, SMA, SC and Thl the cortical premotor area (PM), and some subcortical nuclei as caudatus (Cau), putamen (Put) and globus pallidus (GPi). The following ensembles of tracts were considered: (1) the set of connections between the regions cited above in the contralesional area and the

corpus callosum (Figure -a) that will be here indicated as trans-callosal circuit (CC); (2) the ensemble of connections linking the cortical regions defined as cortical loop (CORT) (Figure -b); (3) the ensemble of connections linking subcortical regions called subcortical loop (SUBCORT) (Figure -c). To provide a more detailed description of the SUBCORT motor pathways, five main sub-networks were identified: (a) M1 loop (Figure -d), (b) SMA1 loop (Figure -e), (c) SMA2 loop (Figure -f), (d) PM1 loop (Figure -g), (e) PM2 loop (Figure -h).

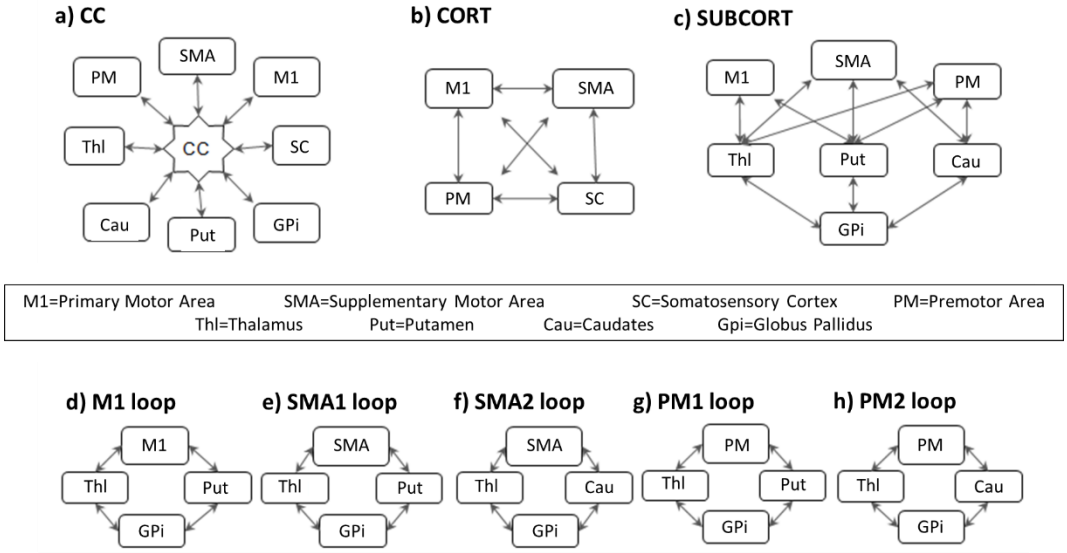

Figure 3.3: Schematic representation of the trans-callosal (CC), cortical (CORT) and subcortical (SUBCORT) networks. The five sub-networks of this latter circuit are also reported on the right panel (d–h).

The individual high-resolution T1-weighted images were segmented into WM, GM and CSF tissues using the SPM toolbox [75]. A binary mask was derived for GM using a conservative 95% threshold on the individual probability maps. Eighty regions from the Freesurfer parcellation were considered (Brainstem and Corpus Callosum were excluded) and masked with the binary GM mask. Four small subcortical regions per hemisphere resulted to be empty after GM masking and were excluded from further analyses, for a total of seventy-two regions. For all indices, the mean GM value across each masked ROI was then calculated. In particular, average measures were calculated across corresponding regions in both hemispheres for controls, while averaging was constrained to the contralateral hemisphere for patients, leading in both cases to thirty-six representative GM values for each index and subject.

The reproducibility of indices' mean values were assessed by evaluating the intraclass correlation coefficients (ICC) and the intra- and inter-subject coefficients of variation (CV_{intra} and CV_{inter}) [76] [77] [78]. ICC is one of the most important methods to assess the reliability of a measure, reflecting both intra- and inter-subject variability. It allows evaluating how measurements derived from the same subject are reproducible across sessions. ICC levels and reliability can be evaluated using the following recommendations: poor (< 0.4), fair (0.41 – 0.59), good (0.60 – 0.74) and excellent (> 0.75) [79] [80]. The CV_{intra} (within-subject CV) measures the variability between sessions of the same subject, reflecting both physiological variations that can occur in a natural way and possible measurement errors [78]. Finally, the CV_{inter} (between-subject CV) measures the stability across the group, reflecting the inter-individual variability. The representative CV_{inter} measure was then computed as the mean of the CV_{interj} from the two sessions. For biological measurements from MRI, $CV_{intra} \leq 10\%$ and $CV_{inter} < 15\%$ are considered as acceptable [81] [82].

To compare the indices in WM, since the Kolmogorov–Smirnov normality test confirmed the normal distribution of the percentage values, statistical comparisons with an unpaired *t*-test were performed to detect significant differences between the percentage absolute changes between time points (Δ_{tp12c} and Δ_{tp12}, Δ_{tp23}, Δ_{tp13} presented in the methods of the previous subchapter), with a strong conservative Bonferroni correction for multiple comparison ($\alpha = 0.05$).

In addition, in order to assess the predictive power of both tensor-derived and 3D-SHORE-derived indices, different linear regression models were considered and their performance in predicting the clinical motor outcome at six months (NIHSS at *tp3*) was tested. For each network, three types of regression models were built and compared. In detail, the following models were considered:

- *Tensor-based model (TBM)*: the average across all the connections of the considered loop at *tp1* was calculated for each index (MD, FA) and both mean values were included as predictors along with age, stroke size and NIHSS at *tp1*.
- *SHORE-based model (SBM)*: the average across all the connections of the considered loop at *tp1* was calculated for each index (GFA, PA, RTAP, RTPP, MSD) and these mean values were included as predictors along with age, stroke size and NIHSS at *tp1*.

- *Global microstructural model (GBM)*: all the indices (both tensor-derived and 3D-SHORE-derived) were included as predictors, after having calculated their individual mean value across all the connections of the considered loop. No clinical information was included.

In each case, the optimal model was identified by a backward selection process (significance threshold: $p = 0.05$).

In order to compare the GM region-based measures, a three-way mixed (within-between) analysis of variance (ANOVA) was firstly performed for each microstructural index to test the significance of different factors, using the mean index value as dependent variable. Three independent variables were considered: *Time* with two levels, *Region* with thirty-six levels (within-subject factors) and *Group* with two levels as between-subject factor. In addition, a further two-way repeated measures ANOVA was performed on the patient group data in order to assess for the presence of longitudinal changes in contralateral GM structures across all temporal scales. Also, in this case the mean value for each index was used as dependent variable in the corresponding ANOVA, while two independent variables were included: *Time* with three levels and *Region* with thirty-six levels. For each ANOVA, Mauchley test was used to assess the sphericity assumption and Greenhouse-Geisser epsilon adjustments for non-sphericity were applied where appropriate. Post-hoc tests adjusted for multiple comparisons with the Bonferroni correction were used when significant interactions were found. For all statistical tests, $p < 0.05$ was considered to be significant.

3.2.2.2 Results

WM networks. In terms of test-retest reproducibility, tract-based results highlighted excellent consistency across sessions in the three networks for tensor-derived as well as 3D-SHORE indices, with ICC > 0.8 in almost all cases and values close to unity for the SUBCORT loop. This high reliability was matched with high intra-subject stability across sessions as measured by CV_{intra} values, well below 10% and, in most of the cases, also below 5%. As expected, the between-subject variability was higher than the within-subject, although the mean CV_{inter} values were ≤ 15% in

all networks, with similar patterns in the three loops for each index. For each index and network, the mean of the percentage absolute changes between all *tp* is reported in Figure along with standard deviation across subjects.

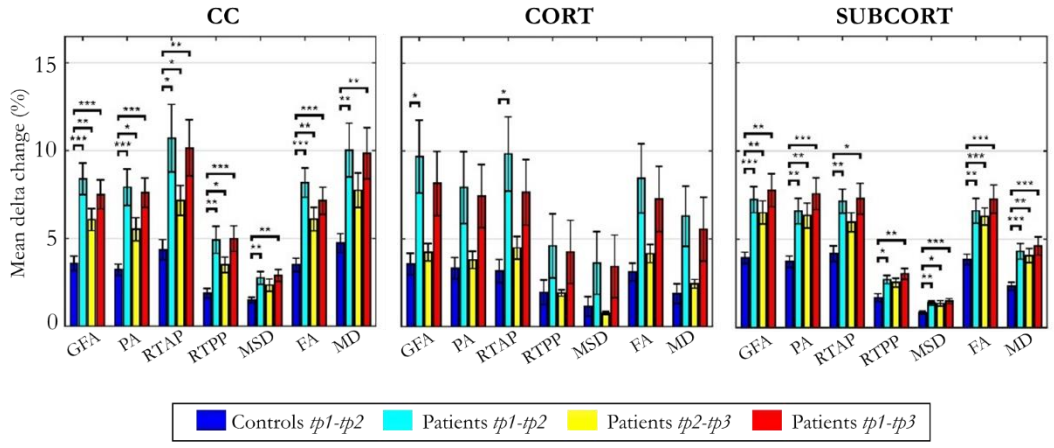

*Figure 3.4: Mean ± standard deviation longitudinal changes across subjects in percent absolute values in controls and patients with significant differences between cohort distributions (*p < 0.05, **p < 0.01, ***p< 0.001) for each index in trans-callosal (CC), cortical (CORT), and subcortical (SUBCORT) networks.*

The p-values resulting from the statistical analysis are shown as stars with three levels of significance (*p < 0.05, **p < 0.01, ***p < 0.001). Regarding the CC network, all the anisotropy measures (GFA, PA and FA) reached the highest significance when comparing Δ_{tp12c} and Δ_{tp12} as well as Δ_{tp12c} and Δ_{tp13} ($p < 0.001$). Moreover, GFA and FA showed higher significance than the other microstructural indices in the comparison between Δ_{tp12c} and Δ_{tp23} ($p < 0.01$). MSD and MD highlighted the same patterns across time and the same statistical differences, with no significant changes between Δ_{tp12c} and Δ_{tp23}. In the CORT network, only few significant differences were detected between controls and patients (Δ_{tp12}) by GFA and RTAP, while for all the other indices the longitudinal changes, although appreciable, did not reach the statistical threshold. Conversely, several significant differences were detected again in the SUBCORT loop by all the indices at multiple time scales, except for RTAP and RTPP which did not depict significant changes between Δ_{tp12c} and Δ_{tp23}. All the anisotropy measures confirmed the presence of marked changes over time involving also this network, with similar patterns to the findings shown in CC.

The reference linear regression model including only clinical variables at baseline (age, stroke size and NIHSS motor score at tp1) and avoiding microstructural indices

could predict the NIHSS outcome at tp3 with low correlation (R2 = 0.546; adjusted R2 = 0.489; $p < 0.05$). The TBM, enclosing MD-FA at *tp1* plus the clinical variables, allowed increasing the prediction capability of the reference model in the CORT and SUBCORT networks. In detail, the TBM for SUBCORT presented the best performance (R2 = 0.975; adjusted R2 = 0.955; $p < 0.001$) holding MD, FA, stroke size and age as relevant predictors. In the case of the CORT network, a higher correlation than the reference model was found with the TBM retaining only stroke size and MD as significant predictors (R2 = 0.700; adjusted R2 = 0.614; $p < 0.05$). Conversely, the tensor-based model for CC did not include any microstructural index, returning the reference model as the optimal one.

The SBM, embedding the five SHORE indices at *tp1* plus the clinical variables, reached the highest correlation in the SUBCORT network (R2 = 1; adjusted R2 = 0.998; $p < 0.001$). The optimal predictive model held clinical variables plus GFA, MSD, RTPP and PA as significant predictors. The SBM for CORT excluded all the microstructural indices, leading to the reference model as the optimal one. Finally, in the CC network the SBM presented a slightly lower correlation than the reference (R2 = 0.454; adjusted R2 = 0.385; $p < 0.05$) but highlighting RTPP as the only significant predictor.

The GBM, including only the DWI-based indices, allowed to substantially increase the capability to timely predict the motor outcome compared to the clinical reference model. In detail, the SUBCORT network provided again the highest correlation (R2 = 0.728; adjusted R2 = 0.694; $p < 0.01$) keeping only RTPP as significant predictor. The predictive model for the CC network also featured high correlation (R2 = 0.713; adjusted R2 = 0.631; $p < 0.05$) maintaining MD and RTPP as predictors, while GFA, RTAP and MD were retained in the predictive model for CORT. This network led to the GBM with the lowest correlation (R2 = 0.724; adjusted R2 = 0.586; $p < 0.05$), but still higher than the reference model.

The results emphasize the importance of using networks' information rather than the single connections considered one by one, possibly highlighting the highly cooperative behaviour of the brain.

GM regions. GM region-based reproducibility results are reported in Table in terms of mean and SD values across ROIs. RTAP, RTPP, MSD and MD reached excellent consistency, with mean ICC > 0.90 and very low SD across ROIs (< 0.10). Conversely, all the anisotropy measures showed only good reliability and more variability across the different GM structures. This was further confirmed by the CV_{intra} measure, reporting mean values < 10% in all cases albeit higher for GFA, PA and FA in comparison to the other microstructural indices. Similar to those resulting from WM networks analysis the mean CV_{inter} values were ≤ 15% in all regions, respecting the recommended range [81] [82].

Table 3.2: Reproducibility for grey matter (GM) outcomes reported as mean ± standard deviation values across all the considered GM regions. Results are quantified in terms of intra-class correlation coefficient (ICC) and intra-subject coefficient of variation (CV intra) for all the indices.

	ICC	**CV_{INTRA} %**
GFA	0.63 ± 0.22	7.36 ± 2.96
PA	0.61 ± 0.24	6.82 ± 2.42
RTAP	0.91 ± 0.07	3.40 ± 1.63
RTPP	0.92 ± 0.07	1.73 ± 0.78
MSD	0.93 ± 0.09	1.97 ± 0.75
FA	0.66 ± 0.17	9.25 ± 3.59
MD	0.94 ± 0.08	3.09 ± 1.71

Regarding the controls vs patients analyses on the outcomes from the region-based quantification in GM tissues, the mixed ANOVA revealed a significant three-way interaction between *Group*, *Time* (TP) and *Region* (ROI) for all the anisotropy measures (GFA, PA, and FA) and RTPP. For the four indices, post-hoc Bonferroni tests revealed significant between-group differences in several regions at both time scales, showing in these cases higher values in patients than controls (Figure -A,B). While the most widespread changes were detected in terms of anisotropy at *tp1*, four common regions were identified as significantly altered (Patients > Controls) also by RTPP. The remaining indices failed to reach a significant three-way interaction even though control vs patient differences can be visually appreciated in Figure -A. Moving a step backwards in the mixed ANOVA, all the indices except RTAP revealed a significant two-way interaction between Group and ROI confirming that,

considering the overall time scales, there were differences in specific GM regions between the two groups. The anisotropy measures were highly consistent, with FA highlighting more widespread increased values in GM for patients as before. Finally, only GFA, PA and FA revealed an overall significant main effect of Group.

Considering the longitudinal analysis on the patient measures only, again all the anisotropy indices along with RTPP and MD revealed a significant interaction between TP and ROI. Post-hoc Bonferroni tests (Figure) detected higher values just after the stroke event (*tp1*) in comparison to *tp2* and *tp3*. Conversely, an opposite trend was found for RTPP detecting a single region with higher values at *tp2* compared to *tp1*. For MD, despite the significant interaction no regions survived the Bonferroni corrections of the post-hoc paired tests (Figure -B,C).

In stroke patients, studies in GM are less consistent and generally consider the tissues in the contralateral hemisphere as normal [83]. However, regions remote (upstream or downstream) from the infarct have been demonstrated to undergo marked changes over a time course of 2 days to 1 year [84]. Maniega et al. [83], which used the contralateral part as reference, showed a trend of increased MD/decreased FA values within the lesion starting from the first week after the injury. Here, the longitudinal analyses on the patient group demonstrated a similar pattern but in the contralateral hemisphere, revealing an increase in MD values over time that mainly involved GM motor regions. Conversely, FA exhibited an initial widespread increase at tp1 over temporo-frontal and motor areas, followed by a gradual decrease towards normality at tp3. However, the fact that differences across time within a patient population and across groups can be detected using such indices provide evidence in favour of their exploitability as potential numerical biomarkers for GM plasticity in disease, leaving their interpretation in terms of microstructural properties an open issue.

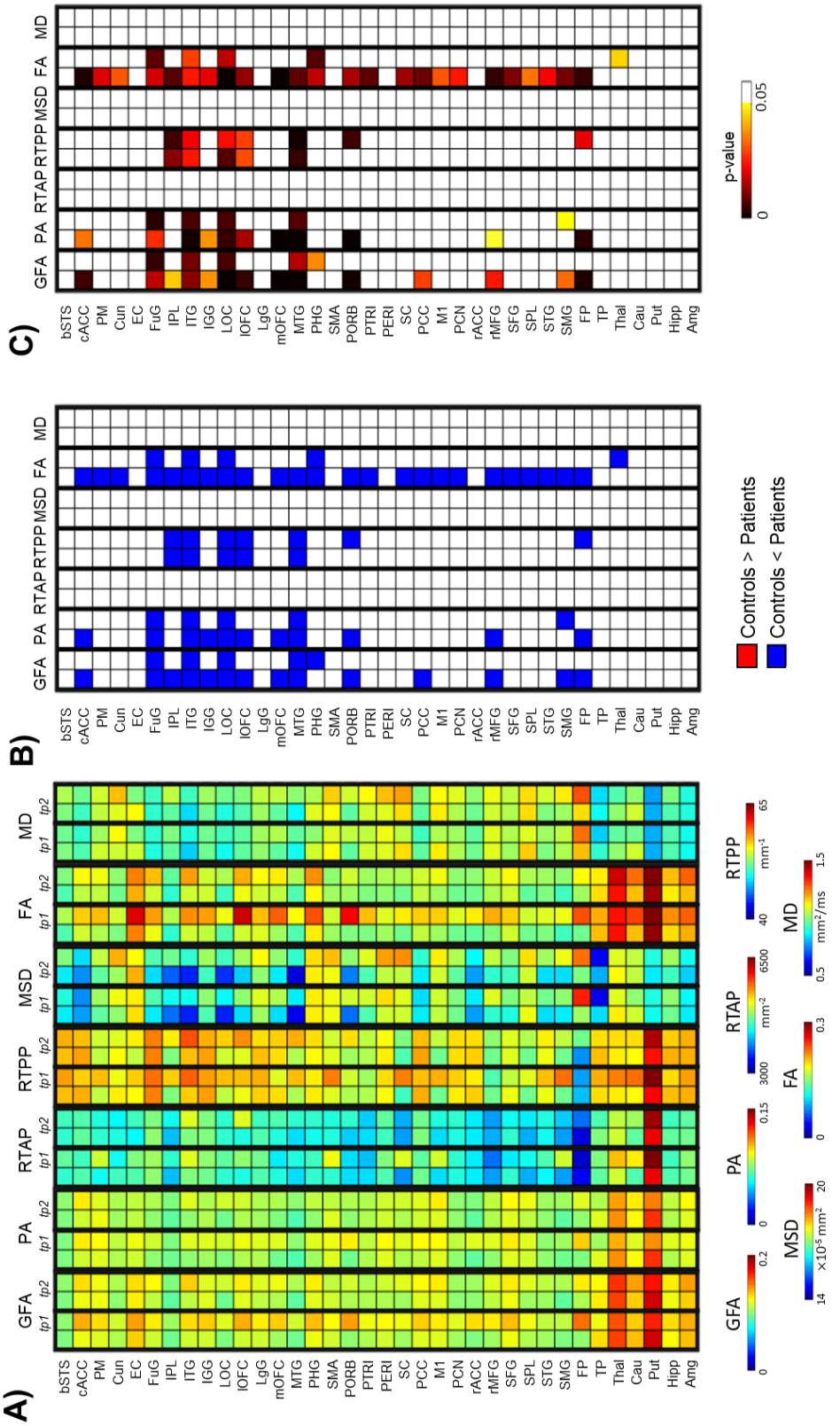

Figure 3.5: A) Mean index values for each index and each time point (tp) block, the first column represents the controls while the second column the patients. B) Post-hoc results of the significant interactions between Group, TP and Region (ROI), expressed in red if the difference between control and patient mean values is positive (controls>patients) and in blue if the difference is negative (controls<patients). (C) Corresponding p-values for the significant ROIs resulting from the post-hoc tests. These values (p<0.05) are Bonferroni corrected for multiple comparisons.

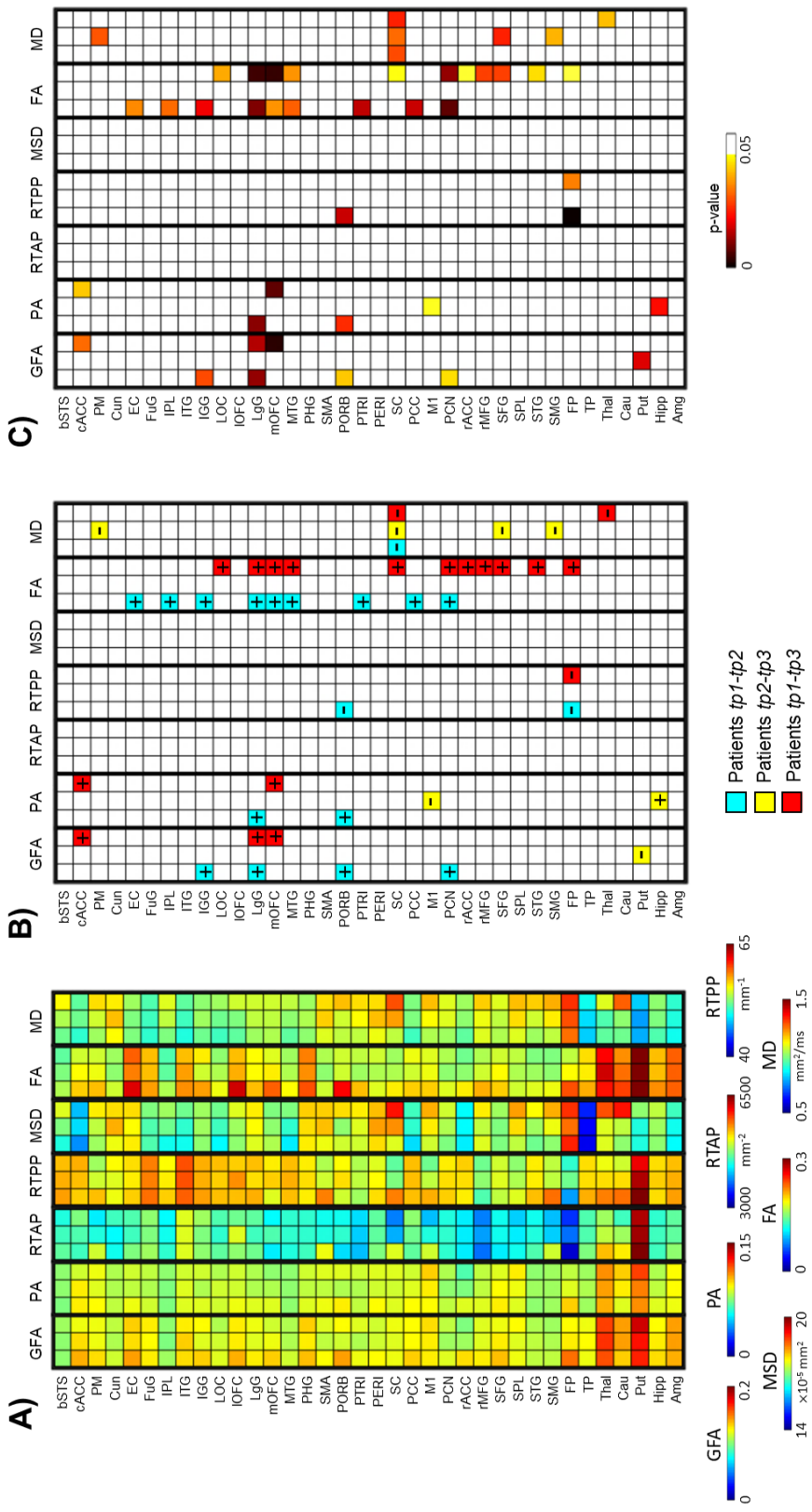

Figure 3.6: A) For each index, the first column represents the mean index values at tp1, the second column at tp2 and the third at tp3. B) Post-hoc results of the significant interactions between Time Point (TP) and Region (ROI) for the different time scales (light blue: tp1-tp2; yellow: tp2-tp3; red: tp1-tp3), expressed with their sign as positive or negative depending on the difference results. (C) Corresponding p-values for the significant ROIs resulting from the post-hoc tests. These values ($p<0.05$) are Bonferroni corrected for multiple comparisons.

3.3 ASSESSMENT OF MICROSTRUCTURAL INDEXES IN THE WHOLE CONNECTOME

After the simpler analyses focused on limited brain areas, further investigation was performed to extend the index evaluation to the whole connectome. We defined the connectome as an undirected graph G = (V, E), where V is the set of vertices corresponding to the ROIs of a full brain parcellation, and E is the set of weighted edges, corresponding to the connectivity values among pairs of ROIs. The microstructural indexes are injecting in the connectivity matrix, evaluating the mean value for each index along the bundle for each pair regions. In details, the mean value for each connection is derived by averaging all the mean values from fibers that belong to that connection. As already presented in Chapter 2, the structural connectivity summarizes the connectivity between all pairs of regions in one matrix. By injecting the microstructural properties, the adjacency matrix become weighted.

In the following subchapters, two different approaches were applied: the first is a feature selection approach [Obertino, et al. 2016 (PRNI)], which takes into account the set of connections as features; the second is a graph theory approach [Obertino, et al. 2016 (OHBM)], in which the properties of the whole-brain connectivity are summarised in specific measures for each ROI, as presented in the previous Chapter. For this work, I helped in designing the methods, processed the data (reconstructed the connectome for all the subjects in each time point, injected the microstructural properties, applying feature selection and graph theory approaches) and contributed to the writing process of the papers.

3.3.1 Feature selection on graph

The weighted adjacency matrices were used as input of the infinite feature selection (Inf-FS) [85] algorithm to rank the features (connections) by importance regarding the patients versus controls classification task [Obertino, et al. 2016 (PRNI)]. RTAP, R=D/2, GFA and PA were chosen for these analyses based on the previous results. In this work, 18 subjects were selected (one patient was excluded, because of noisy connectivity values, and consequently one control to maintain the

balance between classes). The Δ_{tp12c} and Δ_{tp12} were taken into account in order to obtain the representative longitudinal values considering the highlighted importance of the *tp1* in the previous works. As above, the average of the two hemispheres was considered for controls, while only the contralateral part was used for patients.

3.3.1.1 Methods

The graph G of each subject was represented by the adjacency matrix D_n, where each element d_{ij}^n, $1 \leq i; j \leq N$, $N = 39$ is the corresponding entry of the connectivity matrix of subject $n = 1, \ldots, 18$. In order to measure how well each connection separates the two classes of patients (P) and controls (C), a discriminant matrix M was defined using a simple heuristic method for measuring class separation, based on the separation of the class means. For each entry, (i.e., for each feature), the mean and variance are estimated across subjects to generate the matrix *M* whose entries are:

$$M_{i,j} = \frac{\mu_{i,j}^{c} - \mu_{i,j}^{p}}{\left(\sigma_{i,j}^{c}\right)^2 + \left(\sigma_{i,j}^{c}\right)^2}$$

where

$$\mu_{i,j}^{k} = \frac{1}{N_k} \sum_{n \in N_k} d_{i,j}^{k}, \qquad k \in \{C, P\}$$

In the same way, the standard deviation vectors $\sigma_{i,j}^{k}$ for each feature $d_{i,j}^{k}$ of class k was calculated. The approach proposes to rank the features by importance regarding the patients versus controls classification task. To this end, the matrix *M* was used as input of the infinite feature selection (Inf-FS) [85] algorithm, where connections of the graph are seen as features. By construction, the Inf-FS method allows to use convergence properties of the power series of matrices and evaluate the relevance of a feature with respect to all the other ones taken together. In the Inf-FS formulation, each path of a certain length *l* over the graph is seen as a possible selection of features. Letting these paths tend to an infinite number, it permits the investigation of the importance of each feature. As a result, this method assigns a score of "importance" to each feature by taking into account all the possible feature subsets, therefore the higher the final score, the most important the feature. The final rank is

then used in the experimental section, where it was proved that the selected connections turn out to be effective from the classification point of view.

In order to obtain some measure of relevance of the subset of features (connections), a classification approach was followed, which provides an accuracy measure, with precision and recall. Moreover, the receiver operating characteristic (ROC) curve was obtained as well as the corresponding the area under the curve (AUC). Training and testing pools were created using a cross-validation process leave-1-out method, while a Support Vector Machine was used for classification.

3.3.1.2 Results

Good performance, in terms of accuracy, precision, recall and AUC, were obtained using a relatively low number of features, suggesting that few connections could be the key for discriminating patients from controls. Among the set of the first 20 features, six are common to the four indices. Reducing the feature set to this ensemble, the classification performance is slightly degraded especially for GFA and RTAP. However, the still good performance could be an indication of the relevance of such connections in the considered task, pointing to a network modulation involving areas in different cortical and subcortical regions.

For the sake of comparison, Table provides the performance of the classification algorithm using the 23 connections manually selected involving the cortical and subcortical motor loops, previously presented.

Table 3.3: Classification performance on the 23 manually selected features from cortical and subcortical networks.

Index	Accuracy	AUC	Precision	Recall
GFA	66.67	56.79	61.53	88.89
RTAP	50	54.32	50	22.22
R	55.56	50.62	55.56	55.56
PA	50	41.98	50	33.33

The discriminative power of those features is lower than that one obtained using the same number of features that are first ranked by the Inf-FS algorithm (performance reported in Table 3.4).

Table 3.4: Classification performance on the 23 first ranked features following Inf-FS.

Index	Accuracy	AUC	Precision	Recall
GFA	88.89	97.53	100	77.78
RTAP	88.89	100	100	77.78
R	88.89	97.56	87.50	77.78
PA	83.33	92.59	87.50	77.78

This could suggest that a more extended portion of the network is involved in the plasticity process and thus that a wider perspective should be taken for its assessment. However, results show that connection paths with high discriminative power can be identified out of motor networks allowing a classification accuracy ranging between 83% and 98% for the different indices.

3.3.2 Clinical relevance of graph analysis

Simultaneously, the whole-brain connectivity was evaluated with graph analysis, estimating node (regions) properties, and testing the differences between two cohorts [Obertino, et al. 2016 (OHBM)]. In this work, two diffusion indices were used: GFA and PA.

3.3.2.1 Methods

Weighted connectivity matrices derived from each scan for each subject, considering contralateral hemisphere of patients, were analysed to estimate the following node (regions) properties:

- Betweenness Centrality (BC): fraction of all shortest paths in the network that contain a given node

$$b_i = \frac{1}{(n-1)(n-2)} \sum_{j,h \in N, h \neq j, h \neq i, j \neq i} \frac{\rho_{hj}(i)}{\rho_{hj}}$$

where *n* is the number of vertices of the graph, ρ_{hj} is the number of shortest paths between *h* and *j*, and $\rho_{hj}(i)$ is the number of shortest paths between *h* and *j* that pass-through *i*;

- Clustering Coefficient (CC): average of the local clustering coefficients of all the vertices, which measure the proportion of links between the vertices within its neighbourhood divided by the number of links that could possibly exist between them

$$C = \frac{1}{n} \sum_{i \in N} \frac{2t_i}{k_i(k_i - 1)}$$

where *n* is the number of vertices of the graph, *N* is the set of graph nodes, t_i = number of triangles around a node *i* and k_i the neighbours;

- Eigenvector Centrality (EC): influence of a node in a network

$$e_i = \frac{1}{\lambda} \sum_{j \in N} a_{ij} e_j$$

where *n* is the number of vertices of the graph, λ is a constant, a_{ij} represents the presence (a_{ij} = 1) or absence (a_{ij} = 0) of link between nodes *i* and *j*;

- Strength (S): sum of weights of link connected to the nod.

For each graph measure and each microstructural information, a Kolmogorov-Smirnov test between *tp1c* and each *tp* of patients was performed followed by Bonferroni's correction ($P < 0.05$) for multiple comparisons.

3.3.2.2 Results

All microstructural indices showed significant differences only for S, EC and BC in two regions: Frontal and Temporal Pole (FP and TP, respectively). In particular, the differences between groups in the acute time point (*tp1*) and at 1-month follow-

up (*tp2*) was reached in all cases presented above. While, only BC catches differences between groups among all time points *tp1*, *tp2* and *tp3* (Figure).

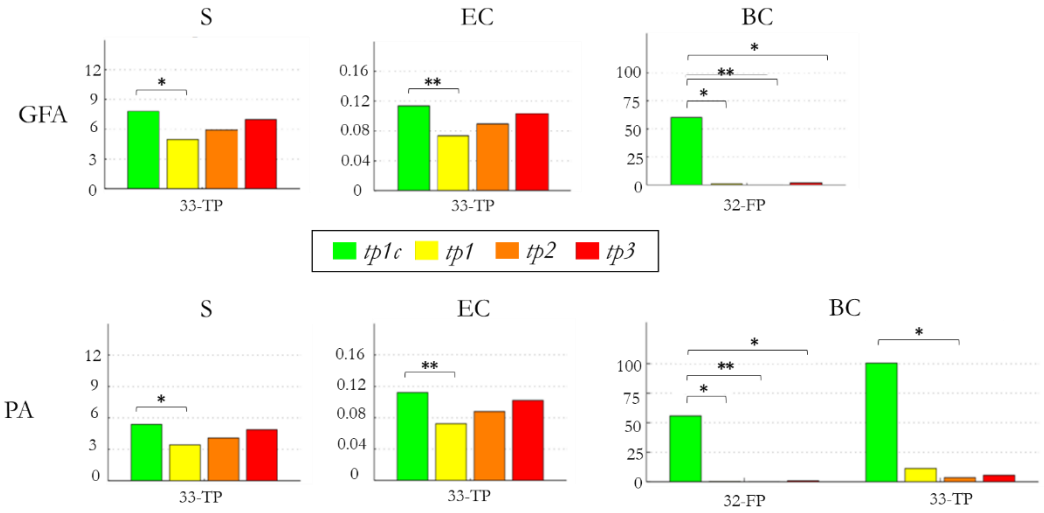

*Figure 3.7: Graph analysis results on GFA index on the first row and PA on the second line. Only the regions (FP, TP) and nodes properties (S, EC and BC) with significant * $p < 0.05$ and ** $p < 0.01$ (corrected) are here reported.*

3.4 CONCLUSION

The indices derived from advanced *Propagator models* performed better than classical DTI derived indices, achieving a high predictive power for clinical outcome over cortico-subcortical connections and a good discrimination between patients and controls at different time scales, further confirming their validity in the application to neurological disorders such as ischemic stroke. The specificity of the SHORE indexes is demonstrated by their significant focus in the six months changes (*tp1-tp3*) and focus in few regions respect to the generalized changes of FA in almost all the regions and all time points. Their combination can allow to convey a more detailed microstructural description, marking a step forward in the definition of a novel family of biomarkers. The benefit of taken into account the properties along all the connectivity is evidenced from the whole brain connectivity analysis with both feature selection and graph theory approaches.

More in general, the set of microstructural properties derived from the advanced *Propagator models* represent stable biomarkers that should be included in the clinical-decision processes. In particular, their values in *tp1* boost the prediction of the

outcome of 6 month after the injury. They provide some microstructural information that are hidden in the classical measures, performing better than *Compartmental model* - derived indices in terms of relevance and redundancy, and reaching significant results in healthy subjects vs patients discrimination.

4 EVALUATION OF DIFFERENT ESTIMATES OF STRUCTURAL CONNECTIVITY

Structural connectivity analysis is a powerful tool for both neuroscience and clinical applications. The last ten years have witnessed a proliferation of methods for all the processing steps needed to obtain structural connectivity, as presented in Chapter 2. In particular, in the last decade the reconstruction models were improved with advanced models that required a multiple-shell acquisition scheme. Previously, an assessment of these new generation models was obtained by evaluating the error of the ODF [50]. However, an evaluation of these new ODF in a connectivity model is still lacking, leading to uncertainty on the reliability of structural connectivity with these advanced models.

The utility of the injection of microstructural properties in the structural connectivity was demonstrated in Chapter 3 in some clinical applications. However, the reproducibility of the weighted structural connectivity is still unclear. In this Chapter, I present some published contributions in which I evaluated the reproducibility of different estimates of the structural connectivity. A preliminary work compares different procedures from the simplest DTI model to the advanced SHORE model [Obertino, et al. 2017 (ISMRM)]. Then, SHORE and NODDI-SH are compared in terms of sensitivity and specificity of the model using different weighting properties. The approach used for this comparison represents a framework that allows to assess the reproducibility of each estimate [Obertino, et al. 2017 (CDMRI)].

4.1 COMPARING DIFFERENT CONNECTIVITY PROCEDURES

The comparison between different procedures to obtain the connectivity matrix was tackled investigating the impact of the main steps of the pipeline adopted to extract the structural connectivity. Indeed, the choice of the reconstruction model and the tractography algorithm can change completely the results. Nine subjects were used to assess the intrinsic variability of the connectivity extracted with a different pre-processing, considering a simplified case. To this end, the density measure (i.e the normalized number of streamlines that connect each pair of brain regions) was chosen and used to derive the connectivity matrix relying on a predefined Freesurfer

parcellation. DTI, CSD and SHORE were used for recovering the main diffusion directions through ODF reconstruction. Tractography was performed following either the deterministic or the probabilistic approaches relying on different software implementations [Obertino, et al. 2017 (ISMRM)]. In this work, I contributed partially to the extraction of tractographies and connectivities, I analysed them, and I have written the abstract for the conference.

4.1.1 Methods

In collaboration with the Department of Neuroradiology, in Verona University Hospital, nine healthy volunteers (age = 36.4 ± 9.7) were enrolled in the study. All participations provided written informed consent. All subjects underwent DWI acquisition consisting of two shells with b = 700, 2000 s/mm^2, 24 and 48 gradients, respectively, TR/TE =8500/91 ms, FOV =230×230 mm^2, 60 slices, 222 mm^3 isotropic spatial resolution (Philips 3T Achieva). Ten additional b=0 s/mm^2 volumes were acquired, five with anterior-posterior phase-encoding and the others with reversed blip, resulting in pairs of images with distortions going in opposite directions. T1-weighted anatomical scans were also acquired in all the sessions (TR/TE= 8.1/3.7 ms, 180 slices, 111 mm^3 resolution).

All DWI datasets were corrected for echo-planar imaging (EPI) and eddy current distortions using FSL 5.0.9 and the b0 volumes that were acquired with reversed phase-encoding directions. In particular, the FSL TOPUP tool [86] was used for estimating and correcting susceptibility-induced geometric distortions. Then, the FSL EDDY tool [87] was applied to correct for eddy-current distortions and head movements. Once the data have been pre-processed, b0 images were aligned to T1 with a linear registration, using FSL Linear Registration Tool (FLIRT) [6 degrees of freedom and normalised mutual information as cost function]. A set of regions of interest (ROIs) were extracted from the individual T1-weighted images using the Freesurfer Desikan-Killiany atlas (33 cortical and 8 subcortical regions per hemisphere plus Brain-stem and Corpus Callosum) [88].

Three different fiber tracking softwares were considered: Diffusion Toolkit (DTK) [88], MRTrix [88] and DIPY [62]. The chosen softwares are the most cited in the literature. The study here presented allows comparing three different reconstruction methods (DTI, CSD, and SHORE), associated with different

tractography algorithms specified for each software (summarized in Table 4.1). In detail:

- In DTK, DTI reconstruction was performed using only one shell (b=2000) and considering four different tractography algorithms (FACT, Kutta, Streamline, and Tensorline);
- In DIPY, deterministic tractography (EuDX) was performed on the three reconstruction models (DTI, SHORE, and CSD).
- In MRTrix, deterministic tractography was applied to both DTI and CSD reconstruction, performed on the big shell (b=2000), while probabilistic tractography was performed using only CSD.

Structural connectivity matrices were derived for each subject and method. As connectivity measure, we chose the normalized number of fibers connecting region pairs. A distance measure was estimated as the mean absolute difference between pairs of connectivity matrices [90]:

$$d(X,Y) = \sum_{ij} |X_{ij} - Y_{ij}|/2$$

where X and Y are two connectivity matrices. The distance analysis was performed across subjects for each method, across methods for each subject and over the group of subjects. In the latter case, the mean matrices were calculated across subjects for each method.

Table 4.1: summary of all methods applied

DTI	**CSD**	**SHORE**
(*DTK*) FACT	(*DIPY*) EuDX	(*DIPY*) EuDX
(*DTK*) Kutta	(*MRTrix*) deterministic	
(*DTK*) Streamline	(*MRTrix*) probabilistic	
(*DTK*) Tensorline		
(*DIPY*) EuDX		
(*MRTrix*) deterministic		

4.1.2 *Results*

Figure and Table 4.2 illustrate the variability of the distance between pairs of subjects for each method. MRTrix probabilistic tractography following CSD provides the best stability across subjects (0.25-0.33). FACT DTK followed by DTI MRTrix and the other DTI-based DTK methods, instead, resulted in the highest variability. CSD (DYPY and MRTrix) and SHORE (DYPY) deterministic tractography led to comparable results. The ability to disambiguate crossings provides to these methods an advantage over DTI, even though the DYPY implementation is quite close in performance. DIPY deterministic tractography showed the highest agreement across reconstruction models. The lowest distance is the one between CSD DIPY and SHORE DIPY (0.25). This result can be explained by the fact that the principal directions of diffusion extracted from SHORE and CSD ODFs are very similar.

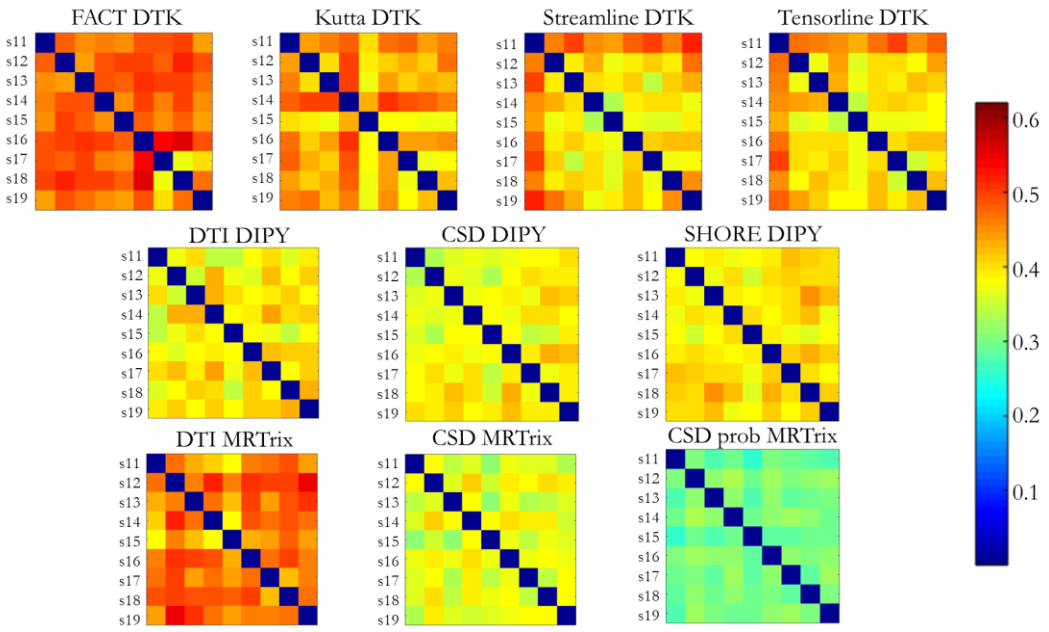

Figure 4.1: Distance analysis across subjects for each method.

Table 4.2: Values of maximum and minimum distances across subjects for each method.

	FACT DTK	Kutta DTK	Streamline DTK	Tensorline DTK	DTI DIPY	CSD DIPY	SHORE DIPY	Tensor MRTrix	CSD MRTrix	CSD prob MRTrix
max	0.55	0.51	0.52	0.50	0.44	0.43	0.45	0.55	0.41	0.33
min	0.37	0.37	0.33	0.35	0.34	0.33	0.35	0.38	0.32	0.25

Figure 4.2 shows the variability of the SC distance measure for each subject across methods. MRTrix methods differ with respect to the others, as also confirmed by the group analysis (Figure 4.3), probably due by the difference of the tractography algorithms of MRTrix respect to the others.

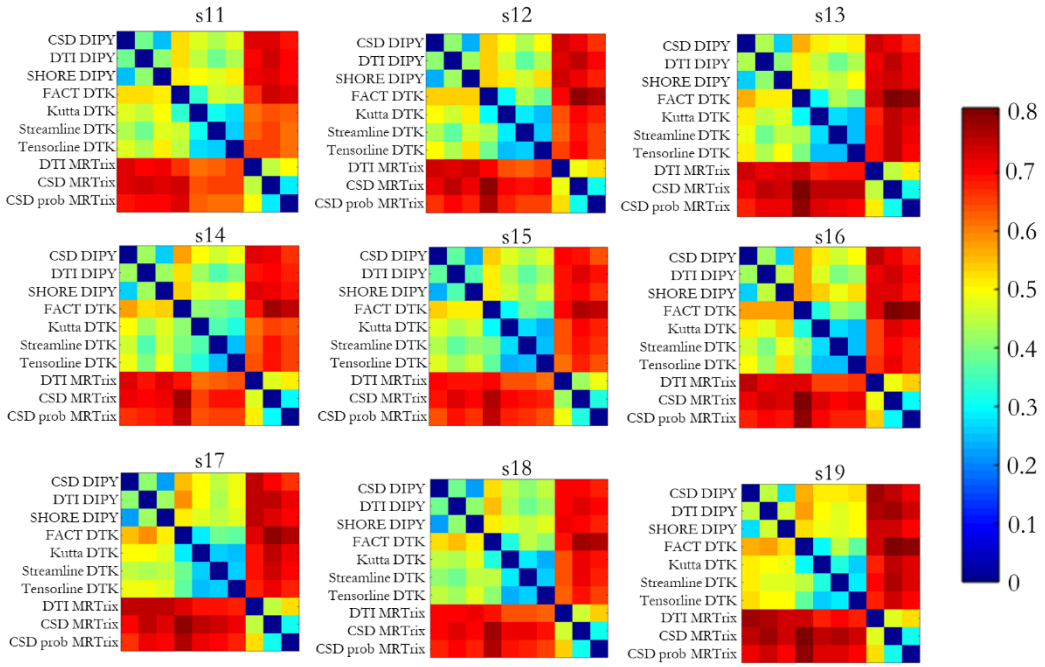

Figure 4.2: Distance analysis across methods for each subject.

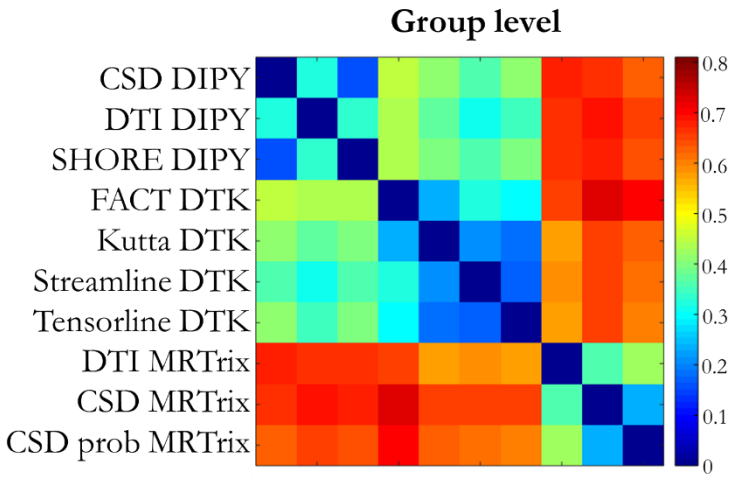

Figure 4.3: Distance analysis across methods on mean matrices of subject group.

Overall, these results suggest that MRTrix provides structural connectivity measures that are different from those obtained by the other methods and that lead to higher stability across subjects, especially following CSD.

4.2 COMBINATION OF ADVANCED ACQUISITION PROTOCOL AND ADVANCED MEASURES

The main limitation of the previous work regards the impossibility to quantitively compare different techniques. In order to define an optimal model, it is necessary to find a method that quantifies the precision of each tractogram model. A possible way to define the precision of a tractogram is to measure the reproducibility. The test-retest paradigm represents a convenient method to find the best compromise between sensitivity and specificity. This paradigm can maximize the differences between different subjects, estimating the sensitivity of a model, and it can recognize the similarity over several acquisitions for the same subject, estimating the specificity of the model.

Examples of this paradigm are reported in [91] [92] [93] [94] [95] [96] [97], where the test-retest paradigm was used to assess the robustness and the reproducibility of the tractography and connectivity pipeline, given the same reconstruction model. In particular, quality measures were quantified using well-known parameters as the ICC and the CV applied to several graph measures (e.g., degree, strength, centrality, path length), as derived from weighted structural matrices. In most of the previous test-retest studies, the weighted adjacency matrix was obtained counting the number of fibers connecting each pair of nodes and correcting this value by the fiber lengths or by the size of the two regions. However, this approach might introduce some biases in the analyses, as the number of fibers is strictly dependent on the reconstruction models and the tractography algorithms chosen. The injection of microstructural information could be more informative compared to the number of fibers, generalizing the values across different reconstruction models and the tractography algorithms, providing additional information as shown in Chapter 3. However, a recent study of Buchanan and colleagues [97], which compared the FA to the other weighting factors reported in literature, retrieved poor ICC performance for FA-weighting graphs. Therefore, the authors suggested further investigations with different types of analysis.

In this subchapter, different advanced properties are injected in the structural connectivity, testing the specificity and the sensitivity with the test-retest paradigm. The analysis is restricted on two advanced ODF estimation methods and three tractography algorithms, injecting different weighting measures [Obertino, et al. 2017 (CDMRI)]. I extracted the tractography that used the MRTrix tool, estimating also the FA map from the same tool. Then, I calculated all the connectivities with all weighting values, analysing and comparing all of them with the correlation parameter and the classification approach. Moreover, I contribute to the concept of this work, writing and presenting the work to the conference.

4.2.1 Methods

The healthy cohort presented in the subchapter 4.1 was extended. Two subjects were acquired after 1 year from the previous acquisition, repeating the scan twice 30 minutes apart, generating three different acquisition for each subject. Two new subjects were also acquired two times. The resulting cohort of eleven subjects (age = 34.5 ± 9.6) underwent at least at one full acquisition with two-shells DWI schema and a T1-weighted acquisition, contributing in a total of seventeen datasets.

The pre-processing presented in the subchapter 4.1.1 was applied to all subjects and all acquisitions.

Starting from a two-shells acquisition, two different fODFs were reconstructed using advanced deconvolution-based methods. The tractography was then performed following either the deterministic or the probabilistic approach. One of the two fODF reconstruction methods is estimate from the NODDI-SH [48], which represents a compartmental model that allows reconstructing the fODF (see Chapter 2 for more details). The other fODF reconstruction method considered here is an extension of the CSD model for multi shell acquisitions called Multi-Shell Multi-Tissue CSD (MSMT) [98], which is available in MRTrix. This model is widely used because it substantially increases the precision of the fODF fiber orientation estimation and reduces the presence of spurious fODF peaks in voxels contaminated by partial volumes of GM or CSF with respect to the classical implementation. In this work a SH order of N=8 was considered for both MSMT and NODDI-SH. Two different tractography softwares were used: MRTrix and DIPY. Deterministic

tractography using EuDX algorithm in DIPY [62] was performed, while MRTrix was used for both deterministic and probabilistic tractography [89], resulting in 6 different tractograms, summarized in Table 4.3.

Table 4.3: summary of all methods applied

	DIPY (EuDX)	**MRTrix (det/prob)**
MRTrix (MSMT)	MSMT – DIPY EuDX	MSMT – MRTrix det MSMT – MRTrix prob
DIPY (NODDI-SH)	NODDI-SH – DIPY EuDX	NODDI-SH – MRTrix det NODDI-SH – MRTrix prob

The following parameters were selected for tractography: angular threshold of 35-degree, 106 seed points randomly selected from the Freesurfer white matter segmentation, maximum fiber length 250 mm. In DIPY EuDX the fODF peaks threshold was set to 0.2, based on previous experiments on synthetic phantom. All the other parameters were left at the default values for both softwares.

Connectivity matrices were obtained relying on four different connectivity measures: the binary connectivity, the fiber density connectivity, and two types of microstructural based connectivity (FA and ν_{ic}). The binary connectivity (B-CM) was obtained by hard thresholding of the streamline number with threshold equal to 10. The Fiber density connectivity (FD-CM) was derived by normalizing the fiber count for the total number of streamlines in the matrix, such that the sum of the elements in the matrix is equal to one. Instead, microstructural properties, in this case FA and ν_{ic}, were averaged along the streamlines for each pair regions obtaining the FA-CM and ν_{ic}-CM, respectively.

Pair-wise similarity between connectivity matrices was expressed by the 2D Pearson correlation coefficient. Two groups of subjects were formed consisting of those who underwent a single scan (seven subjects) and those having two (two subjects) or three (two subjects) acquisitions. The correlation matrix between subjects and acquisitions was used as a feature vector in a simple threshold-based

classifier. In particular, a Receiver Operating Characteristic (ROC) curve analysis was performed to determine the ability of the method to classify the correlation values in different subjects and different acquisitions of the same subject. For each method, ROC curves were created varying the classification thresholds in the range [0-1] with a step size of 0.0001 (10001 points) and calculating for each point the sensitivity and specificity values. These measures were defined as the True Positive Rate (TPR = TP/(TP + FN)) and True Negative Rate (TNR =TN/(FP + TN)), respectively, were TP = true positive, FP = false positive, TN = true negative and FN = false negative. The Area Under the Curve (AUC) was then calculated to assess the classification performance of each method. Finally, the accuracy values were calculated for each threshold and visualized as curves, in order to better highlight the different classifier behaviours.

4.2.2 Results

The group-average connectivity matrices presented a lack of connections in MSMT with DIPY EuDX tractography respect to the other methods, though reporting higher correlation values with FA-CM and ν_{ic}-CM than other combined methods. As expected, in agreement with the literature, MRTrix probabilistic approach leads to the densest solution, followed by the deterministic method of the same software. Compared to MSMT, preliminary results show that NODDI-SH fODF presents in general a higher number of peaks (principal directions), potentially leading to the reconstruction of a higher number of streamlines. Indeed, NODDI-SH followed by MRTrix probabilistic fiber tracking leads to the densest connectivity matrix. This could be an indication of high sensitivity, although it can compromise the specificity, which is the ability to better capturing the inter-subject variability, providing lower performance in the classification task than other methods.

The analysis of the intra/inter-subject correlation matrices highlights that high correlation values are obtained for multiple acquisitions of the same subject. This is clearly visible in Figure 4.4 and Figure 4.5 where blocks appear across the matrix diagonal and corresponding to the same subject.

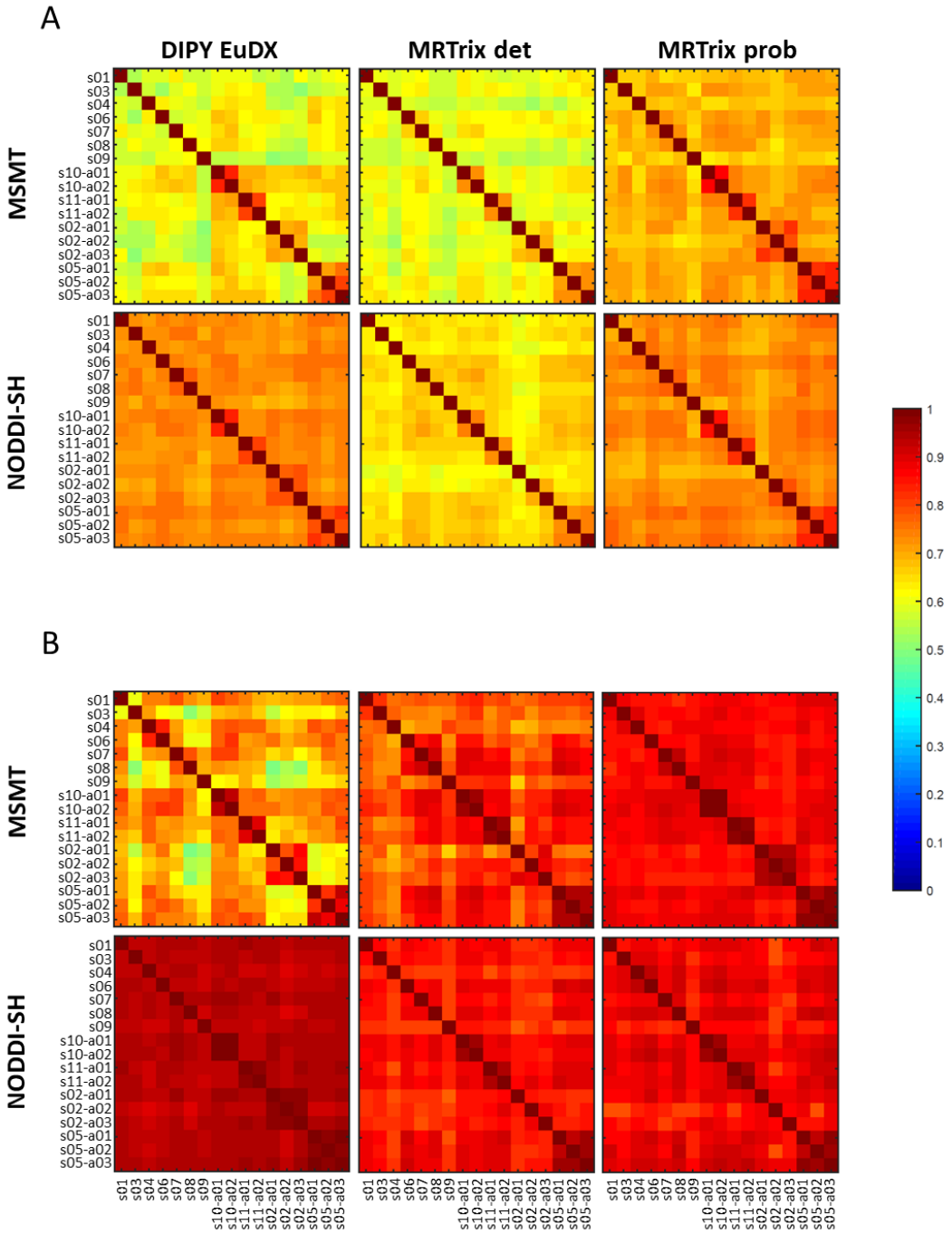

Figure 4.4: B-CM (A) and FD-CM (B) correlation analysis across subjects (s) and acquisitions (a).

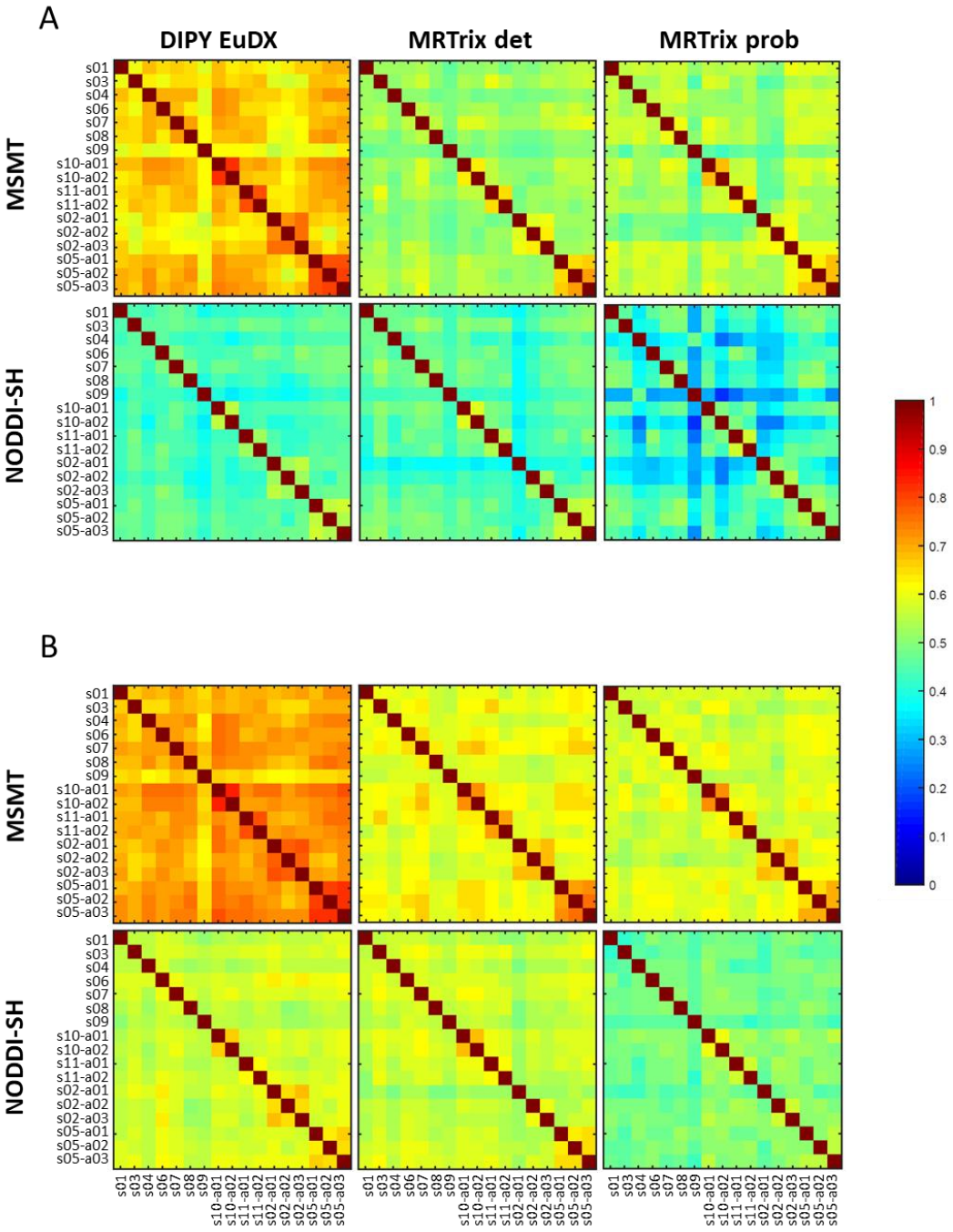

Figure 4.5: FA-CM (A) and ν_{ic}-CM (B) correlation analysis across subjects (s) and acquisitions (a).

This effect is weaker for subject s02, which presents the lowest intra-subject correlation, in particular between the first acquisition and the others. Visual inspection of the data revealed that the raw data were affected by noise, which seems to be the prevalent effect. This highlights the potential of this analysis in revealing acquisition problems once the performance is adequately characterized for a given

acquisition scenario. The range of observed correlation values depends on the connectivity index. In particular, FD-CM (Figure 4.4-B) features the highest set of values both intra- and inter-subject, and NODDI-SH leads to the highest correlation values, both intra- and inter-subject, reaching the maximum with DIPY EuDX tractography ($\rho > 0.96$ for intra-class correlations and $\rho > 0.9$ as inter-class values). MSMT with probabilistic tractography comes next with lower values for both intra- ($\rho > 0.925$) and inter-class correlation ($\rho > 0.8$). While the injection of the fiber number in the correlation matrix (CM) increases the correlation range for all methods with respect to B-CM, microstructural information produces a shift to lower values, as it can be observed in FA-CM and ν_{ic}-CM (Figure 4.5). This could possibly be due to partial volume effects and noise.

ROC and accuracy curves parallel these results. Considering ROC curves, NODDI-SH provides the best classification performance when combined with DIPY EuDX for all the connectivity indices followed by MSMT with MRTrix probabilistic tractography, as shown in Table 4.4.

Table 4.4:Performance of classification in terms of Area of the ROC curves (AUC) for all methods.

	MSMT			**NODDI-SH**		
	DIPY EuDX	MRTrix det	MRTrix prob	DIPY EuDX	MRTrix det	MRTrix prob
B-CM	0.995	0.989	1	1	0.785	0.863
FD-CM	0.979	0.921	1	1	0.834	0.795
FA-CM	0.993	0.994	0.986	1	0.768	0.941
υ_{ic}-CM	0.998	0.994	1	0.997	0.763	0.845

A possible interpretation of these results is that NODDI-SH fODF, in general, has a larger number of peaks than MSMT. As observed before, this results in a denser (less sparse) connectivity matrix across all microstructural indices. On the other end, EuDX is the most restrictive among all the considered tractography methods. The combination of NODDI-SH and EuDX then appears to generate a tractogram that is "minimum" but holds the relevant information for the discrimination task. In other words, it has very good specificity eventually sacrificing

sensitivity. In the case of MSMT, on the other end, the fODF is more selective with respect to the detection of diffusion directions in each voxel, leading to a sparser matrix than NODDI-SH for all tractography algorithms. Consistently, the accuracy analysis allows highlighting the methods that are more effective in separating the two classes, supporting the ROC results and providing detailed information about the optimal correlation threshold for appropriate classification. More in details, these curves, shown in Figure 4.6, highlight the differences among methods when weighting information (FD-CM, FA-CM, ν_{ic}-CM) are injected in CM respect to the B-CM consideration.

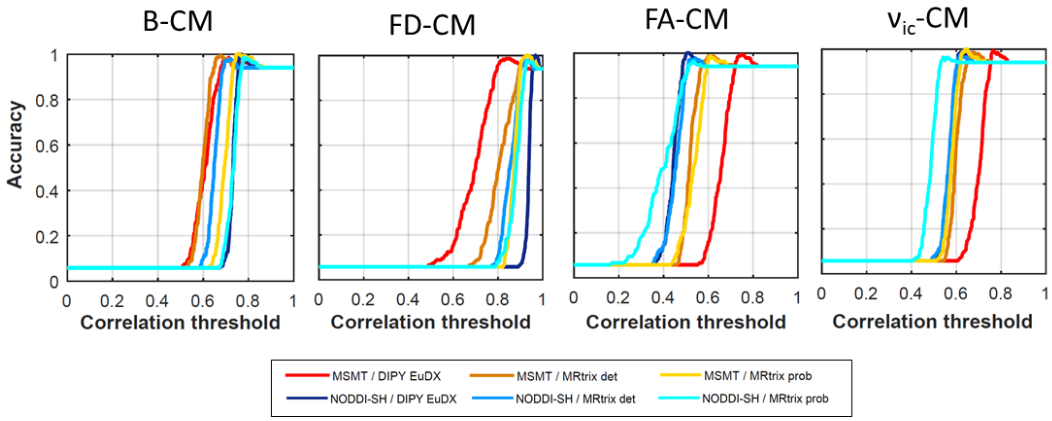

Figure 4.6: Accuracy curves calculated for all the methods.

Both MSMT combined with the probabilistic tractography and NODDI-SH combined with DIPY EuDX tractography reach the optimal accuracy with three of four weighted methods. The perfect classification is available only for a specific threshold as shown in Figure 4.6, probable due by the unbalance of the two classes. Since this dataset is composed of healthy subjects a narrow range of separation thresholds between the two classes would be expected as reported in the literature in terms of small variation coefficient between subjects [100]. Results then highlight that the application of the EuDX algorithm results in an excessive pruning of the tractogram that does not convey enough information for discriminating the two classes of subjects. Switching to MRTrix deterministic, that is less rigid in the constraints for tracking, results in an increased number of fibers and a denser connectivity matrix. If this leads to an improvement in performance for MSMT, which takes advantage of the increased redundancy, it reduces the performance of NODDI-SH. In this respect, for NODDI-SH the denser matrix results to be noisier

as if non-relevant information are added. When passing to MRTrix probabilistic, the same trend is observed for MSMT, which reaches the maximum AUC for all indices except FA, while an inversion is observed for NODDI-SH, whose performance improves for all indices except for FD. This could be explained by the exponential increase in the number of fibers and connections to such an extent that it compensates for the increase of noise, though, without reaching the performance granted by EuDX. Interestingly, the mean values of the FA and υ_{ic} parameters along the detected connections are higher for MSMT than for NODDI-SH reconstruction across tractography methods, that could be an indication of a more anatomically plausible detection of the white matter wiring. However, results seem to suggest that this information is not sufficient for discriminating between groups until the restriction to the tracking algorithm is relaxed at a point to which enough specificity is gained. Table 4.4 shows that the AUC values for the MSMT decrease when passing to the FD weighting methods and increase uniformly across microstructural indices with deterministic algorithms. This means that even though the second tractogram is denser than the first, its descriptive power is lower. A similar trend could be observed for NODDI-SH with a probabilistic tractography when passing from binary matrices to weighting matrices with the exception of υ_{ic}, while the combination with the deterministic algorithm from MRTrix led to a different pattern, reaching the highest AUC value for the FD-CM. AUC values equal to 1 were reached for MSMT combined with the probabilistic algorithm (B-CM, FD-CM and υ_{ic}-CM) and for NODDI-SH combined with DIPY EuDX (B-CM, FD-CM, FA-CM).

4.3 PARTIAL CONCLUSION

Results highlight the variability of the different approaches in both single subject and group level analysis with the first contribution. In details, the advanced SHORE models, which required the multiple-shell acquisition, decrease the distance between subjects compared to the simplest DTI. However, the CSD model, which uses only one shell schema, presents stable results across subjects when, in particular, it is combined with the probabilistic tractography algorithm. The second contribution

identifies a good approach to define the sensitivity and specificity of a model. In details, by extending the CSD to the advanced MSMT estimation and evaluating the new NODDI-SH that uses a multi-shell acquisition, results suggest a trade-off between the selectivity of the fODF (expressed as a function of the number of peaks) and the hardness on the constraints of the tracking algorithm. If the fODF is richer, the combination with a high degree of freedom in tracking would generate more noisy connectivity matrices. However, the variability of tractograms shows a high inter-subject stability in the case of probabilistic tractography, confirming the previous results. In summary, as far as the detection of test-retest subjects is concerned, the MSMT solution seems to be preferable as it provides optimal performance in almost all cases across all microstructural indices. In particular, MSMT paired with the probabilistic tractography reaches the best specificity, maintaining a very high reproducibility across different healthy subjects. Concerning the injection of advanced properties in the connectivity, results clearly highlighted the decrease of the correlation measures across both subjects and acquisitions, and the not perfect reproducibility, although the performance in terms of classification remain high. It can be concluded that the binary matrix, which records only the presence or absence of a link, better reaches the reproducibility of the models, while the inclusion of microstructural properties can be more informative in the case of clinical applications as presented in Chapter 3.

5 GRAPH SIGNAL PROCESSING TO COMBINE STRUCTURE AND FUNCTION

The recently explored application of graph signal processing to the study of brain connectivity opened an interesting opportunity for a multimodal approach, which allows for the integration of structure and function [31]. However, given the novelty of the field, there are plenty of directions that appear worth investigating, but are currently still unexplored. As already mentioned in Chapter 1, Medaglia and colleagues limited their study to fMRI, therefore to low temporal resolution signals, and they haven't optimized the choice of cut-off frequency for the filtering operation defining the aligned/liberal portions of the signals. Further, their investigation remains confined to static analyses of functional signals. Here, we present a new method for function/structure integration that aims at overcoming these limitations. We combine MEG or EEG signals with structural bases that are extracted with Graph Fourier Transform (GFT) applied to the structural connectivity. Moreover, an automated way to define aligned and liberal components is here presented, exploiting the idea of the diffusion kernels. The diffusion kernels permit to relate the aligned and liberal contributions to the path length in the connectivity, which was recently demonstrated important for the mapping of functional activity [99]. In fact, long structural connectivity pathways of length 3 and up to 8 steps contain most of the information needed to map functional correlations with fMRI data. Specifically, the direct structural links mapped only the 57% of the functional correlation, increasing to 77% when adding paths with length of 2, and about 80% with paths passing through 3 nodes. Diffusion kernels integrated in the eigendecomposition of the connectivity matrix have recently been demonstrated to be related to the indirect links [100], opening to the perspective of modelling a new definition of aligned and liberal components.

The contribution that is presented in this Chapter is the result of my visiting period in the Medical Image Processing Lab (MIP:Lab) in Geneva, Switzerland, under the supervision of Prof. Dimitri Van De Ville. In collaboration with Prof. Van De Ville and Dr. Elvira Pirondini, I designed the methods, generated a simulation framework to test the introduced approach, and performed all the analyses on simulated and real data (structural connectivity analysis and EEG/MEG source localization). The study is in preparation for publication.

5.1 DATA ACQUISITION AND SIMULATION

Structural connectivity. In this study, a binary adjacency matrix is derived averaging 26 subject binary matrices. The presence of the connection in the group is defined if at least half subjects present the link in their single binary matrix. The set of subjects is selected from the Human Connectome Project (HCP), pre-processed as follow. The DWI images are already pre-processed by the HCP team (glasser minimal preprocessing reference), following conventional pre-processing steps. Precisely, movements, eddy-current and susceptibility-induced geometric distortions corrections are applied, with the TOPUP and EDDY tools of FSL. Then, the b0 images are aligned to T1-weighted ones with a linear registration, using FLIRT [6 degrees of freedom and normalised mutual information as cost function]. Moreover, the non-linear registration (using FNIRT tool of FSL) is estimated between them and the MNI space to register the Automated Anatomical Labeling (AAL) atlas to the subject space. The AAL atlas is chosen for this analysis in order to have a brain parcellation that could represent the function of the different parcels, instead of a subdivision based on gyri and sulci, such as the Freesurfer parcellation. The combination of MSMT CSD reconstruction model followed by the probabilistic tractography, which is, as demonstrated in Chapter 4, the most reliable method to extract the structural connectivity, is used to derive the fibers for each subject. The AAL atlas and the fibers are then overlapped in the subject specific space, deriving the subject binary structural connectivity matrix (SC).

Functional signal. We define the functional signal x_t (spatial pattern at each timepoint t), which can be obtained by source localization from EEG or MEG. In this study a source localization signal is first simulated to validate the model and then real MEG recordings are used from HCP data.

The simulated source localization is constructed applying a sinusoidal signal (frequency = 10Hz) in a specific region (as the example presented in **Errore. L 'origine riferimento non è stata trovata.**).

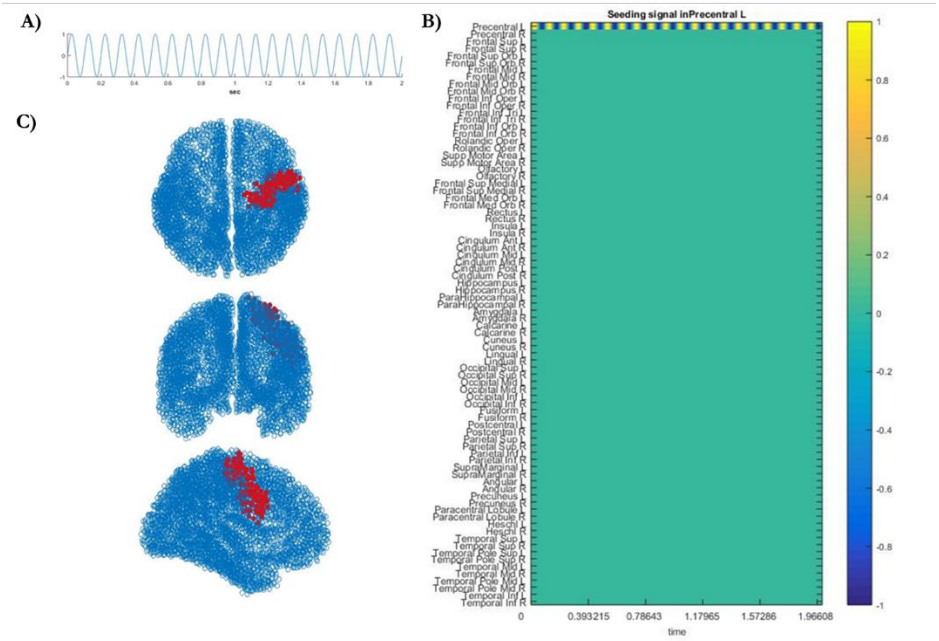

Figure 5.1: Sinusoidal signal (Panel A) in precentral left region (Panel B) with the selected sources points belong to the region (red filled dots) presented in axial, coronal and sagittal views (Panel C).

The signal is then propagated along aligned and liberal components using smooth diffusion kernels defined in a source level set of eigenmodes. The eigenmodes at the source points level are derived applying the GFT on the matrix $A = M * SC$ in which M is a mapping matrix between the used parcellation (AAL in this case, with 82 regions) and the source vertices (~5000 sources), and SC is the group binary connectivity matrix derived from the MSMT probabilistic tractography using the AAL parcellation. In details, the mapping M is defined with a simple approach as a binary matrix with the belonging of each source point to each region:

$$M_{ij} = \begin{cases} 1 & \text{if source point } i \text{ is in the ROI } j \\ 0 & \text{otherwise} \end{cases}$$

Following the idea of Atasoy and colleagues [103], the local connections that correspond to the links of the vertices on the cortical surface mesh are added to the A matrix, resulting in smooth eigenmodes (shown in **Errore. L'origine riferimento n on è stata trovata.Errore. L'origine riferimento non è stata trovata.**).

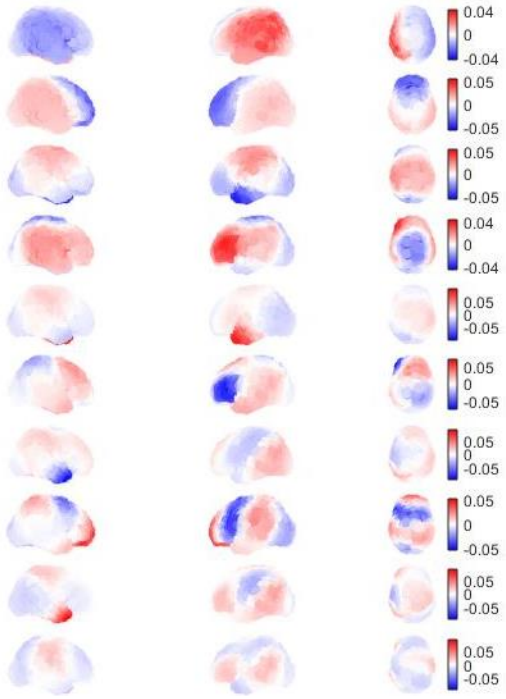

Figure 5.2: First 10 eigenmodes of the example subject (id=106521).

Liberal and Aligned components are defined using a diffusion kernel with τ=-1, in order to simulate a signal as closer as possible to reality. However, the middle components contribution is excluded to simplify the simulation, concentrating the spectrum in the tightly aligned and liberal elements. The simulated time course of 2 seconds is divided in two parts: half period (1 second) propagated with the aligned kernel, and half period (1 second) propagated with the liberal kernel.

The HCP dataset includes subjects with MEG acquisition (248 magnetometer channels with 23 reference channels, 18 magnetometers and 5 first-order gradiometer channels, recorded at 2034.51 Hz sampling rate) co-registered to the MRI structural scans. Three subjects having both resting-state and motor task MEG acquisitions are selected (id=106521, 108323 and 205119). In details, resting-state (rMEG) data are divide in 3 runs of about 6 minute each. The subjects were instructed to relax supine with eyes open, fixing a projected red crosshair on a dark background. Electrocardiography and electrooculography electrodes were used for cardiac and oculomotor monitoring and offline artefact rejection. In the case of movement task (tMEG) acquisition, sensory-motor evoked potentials (adapted from the one

developed by Buckner and colleagues [103] [104]) were acquired. The participants were instructed to tap their left or right index and thumb fingers or squeeze their left or right toes. The limb (hand or foot) and the side (left or right) were instructed by a visual cue, and the timing of each movement was controlled by a pacing arrow presented on the center of the screen (as shown in Figure 5.3**Errore. L'origine riferimento non è stata trovata.**). The paradigm included 32 blocks of 12 seconds each, with 16 of hand movements (8 right and 8 left), and 16 of foot movements (8 right and 8 left) plus 9 rest blocks of 15 seconds.

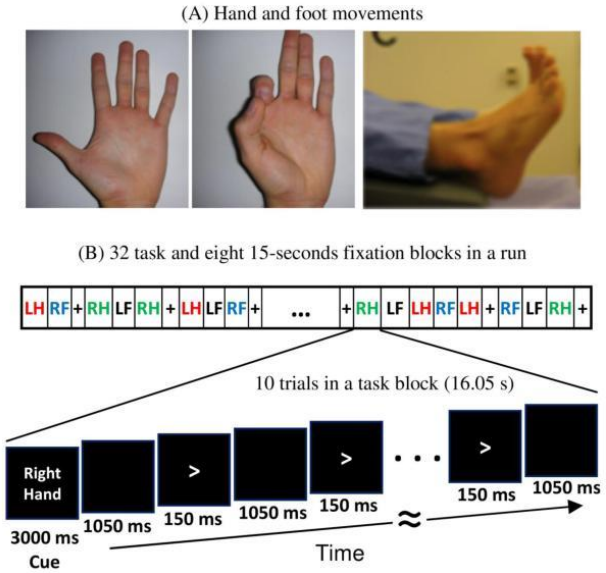

Figure 5.3: Summary of motor task paradigm with the movement of hand and foot in panel A, and the block design in panel B [107].

Electromyography electrodes were applied to hands and feet (as shown in Figure 5.4**Errore. L'origine riferimento non è stata trovata.**) to acquire the muscle electrical signals and pre-process the tMEG dividing the scan in trials.

Figure 5.4: Photo of electromyography sensors placed in each hand and foot\cite{Larson-Prior2013}.

The MEG signals are provided pre-processed by the HCP team. Particularly, the bad channels (values>1^{12}) and bad trials (values>12σ, where σ is the variance of the trial) are removed, data are filtered (Butterworth band-pass filter 1-40 Hz), subdivided in

trials, and baseline correction is applied in case of task signals. Taken the clean signals, the forward and inverse model are applied using the MNE model as presented in detail in Chapter 1, using MNE python tool [102].

Simulated signal analysis. The simulated signal is used as an initial source signal, which is averaged on the chosen ROIs, to demonstrate that the real structural bases are needed for the model. For this reason, a randomization process is used on the group structural connectivity, at the AAL space resolution (82 ROIs). The structural connectivity is randomized 1000 times with a function that maintains the degree of the nodes. In each iteration the randomize matrix is used to extract the eigenmodes to project the simulated source localization. To evaluate the performance of each iteration a ratio between aligned and liberal signals is evaluated, formulating as

$$\varepsilon_{ratio}^{t} = log_{10}\left(\frac{\left|\widehat{x}_{t_A}\right|/_{c_{w_A}}}{\left|\widehat{x}_{t_L}\right|/_{c_{w_L}}}\right)$$

where each filtered signal in $\widehat{x_t}$ is normalized to the mean one (c_w). To summarize the performance of each iteration the ratio (ε_{ratio}^{t}) is averaged along regions and compare to the ratio obtained using the eigenmodes derived from the real structural connectivity

Real data analysis. The analysis on the real data preliminary tests the projection model in both tMEG and rMEG signals localized in the sources of the three selected subjects. Each MEG subject data is projected individually using the eigenmodes derived from the group binary structural connectivity. In details, only right and left hands movement are selected for tMEG, in which trials are averaged for each limb side to obtain a stable time course according to the timing from electromyography signals. On the other hand, for rMEG analysis, only 20 trials of 2 seconds each are selected in each subject for computational problems. The performance is evaluated using three ε_{ratio}^{t} that compared the different filtered signals:

- A/L, which represents the ratio between aligned and liberal signals with negative values for liberal prevalence and positive values for aligned;
- A/M that shows the ratio between aligned and middle, in which negative values represent middle prevalence, while positive values are aligned;
- M/L, which is the ratio between middle and liberal signals, with negative values for liberal prevalence and positive values for middle components.

5.2 GSP FRAMEWORK

Structural Eigenmodes. Applying the GFT to the structural connectivity, structural eigenmodes can be obtained as connectome harmonics [101]. The eigenmodes represent the complete set of orthonormal eigenvectors extracted by the eigendecomposition:

$$\check{\mathcal{L}} = U^L \cdot S \cdot U^{L^T}$$

of the normalized Laplacian matrix, which is formulated as:

$$\check{\mathcal{L}} = D^{-1/2} \cdot \mathcal{L} \cdot D^{-1/2}$$

where $\mathcal{L} = D - SC$ is the unnormalized Laplacian and D is the degree matrix of the structural connectivity SC (binary or weighted). The set U^L includes patterns of connectivities with different degree of alignment to the structural graph, and different amount of local variation, as shown in the group example in **Errore. L 'origine riferimento non è stata trovata.**: the first eigenmodes, corresponding to lower eigenvalues (i.e., lower frequency), vary slowly across the brain and reflect more the underlying structure, while the eigenmodes corresponding to higher eigenvalues (higher frequencies) are characterized by faster variations and less alignment to the structure.

Indirect links. As aforementioned, it is possible to identify the contribution of indirect links through the formalization of the diffusion kernel. Specifically, Van De Ville et al. [100] demonstrated the presence of a link between the eigendecomposition and indirect links. Applying the eigendecomposition to a structural connectivity matrix, a set U^{sc} of eigenvectors and a set S of eigenvalues λ_l are defined as:

$$SC = U^{sc} \cdot S \cdot U^{sc^T}$$

where SC represents the binary matrix of white matter connections. The sum of all length-2 walks between i and j can be read out from the squared adjacency matrix as demonstrated by [100] and rewritten as an eigendecomposition:

$$SC^2 = SC \cdot SC = U^{sc} \cdot S \cdot U^{scT} \cdot U^{sc} \cdot S \cdot U^{scT}$$
$$= U^{sc} \cdot S \cdot S \cdot U^{scT} = U^{sc} \cdot S^2 \cdot U^{scT}$$

Similarly, higher powers of SC relate to longer walks, and all of them are related only with the power of the set of eigenvalues. Moreover, Van De Ville et al. [100] related the indirect paths to the exponential diffusion kernel, defining:

$$K = U^{sc} \cdot exp(\tau S) \cdot U^{scT} = U^{sc} \cdot \sum_{n=0}^{\infty} \frac{\tau^n}{n!} S^n \cdot U^{scT}$$

where τ is the decay factor to decrease the influence of longer walks. With this formulation, the diffusion kernel can be injected in the GFT to relate the indirect links to the eigenmodes (i.e., using the diffusion kernel to weight the eigenmodes).

Combination of DW-MRI and Encephalography. Medaglia and colleagues [31] decomposed the fMRI signal in aligned and liberal components filtering the signal with a selected set of eigenmodes. As already presented in Chapter 1, the GFT of a graph signal $x \in \mathbb{R}^n$ can be written as:

$$\tilde{x} = V^T x$$

where V^T is the set of eigenvectors derived from the eigendecomposition of a connectivity matrix $A = V \Lambda V^T$. Λ represents the set of eigenvalues, ordered so that $\lambda_0 \leq \lambda_1 \leq \ldots \leq \lambda_{n-1}$, and $V = \{v_k\}_{k=0}^{n-1}$ is the set of associated eigenvectors. From this notions, the signal can be described as a combination of its spectral components of different frequencies as follows:

$$x = \sum_{k=0}^{n-1} \tilde{x}_k v_k$$

given $\tilde{x} = [\tilde{x}_0, \ldots, \tilde{x}_{n-1}]^T$, representing the GFT component $\tilde{x}_k$ as the contribution of v_k to the signal x. In details, Medaglia used this formulation to decompose the fMRI signal into three portions: a portion x_A showing strong alignment with respect to the structure, i.e., reconstructed from the combination of low frequency components; a portion x_M characterized by medium alignment, i.e. reconstructed from middle freuquencies; and a portion x_L, more liberal with respect to the graph

and defined in fact as the combination of high frequency components. They defined K_L =10 as the set of liberal components and K_A = 10 as the set of aligned components, which they found as the best cut-offs for the specific cognitive task adopted in their study. Consequently, middle components are identified as $K_M = n - K_A - K_L$. The original signal can then be written as the sum $x = x_A + x_L + x_M$. The arbitrary choice of the cut-offs represents a limitation of the Medaglia study. Here, an automated solution is presented linking the concept of the indirect paths with the aligned and liberal regimes.

Considering the link between the indirect paths and the diffusion kernel, a relationship between the diffusion kernel and the aligned and liberal signal components can be defined. Using a diffusion kernel D, the GFT signal can be expressed as:

$$\tilde{x} = V^T D x$$

and the filtered signal can be consequently derived extending the formula with the inverse GFT step:

$$\hat{x} = V(V^T D x)$$

Applying the eigendecomposition on the Laplacian matrix, the filtered signal can be reformulated as:

$$\hat{x} = U^L({U^L}^T D x)$$

where D takes the respective formulation D_A for aligned, D_L for liberal and D_M for middle, generating the consequently filtered signals $\hat{x}_A$, $\hat{x}_L$ or $\hat{x}_M$.

The introduction of the diffusion kernel allows to replace the choice of a specific number of components with a parameter τ, formulating

- the aligned diffusion kernel as a smooth low-pass filter, formulated as $D_A = exp(\tau S)$ which decreases the influence of the high spatial frequency components by decreasing τ, as shown in **Errore. L'origine riferimento n on è stata trovata.**:
- the liberal diffusion kernel is formulated as $D_L = exp(\tau(\lambda_{max} - S))$ which represents a smooth high-pass filter, where the influence of the low spatial

frequency components decreases by decreasing τ, as shown in **Errore. L 'origine riferimento non è stata trovata.**;

- the remaining middle components can be consequently defined as $D_M = 1 - (D_A + D_L)$.

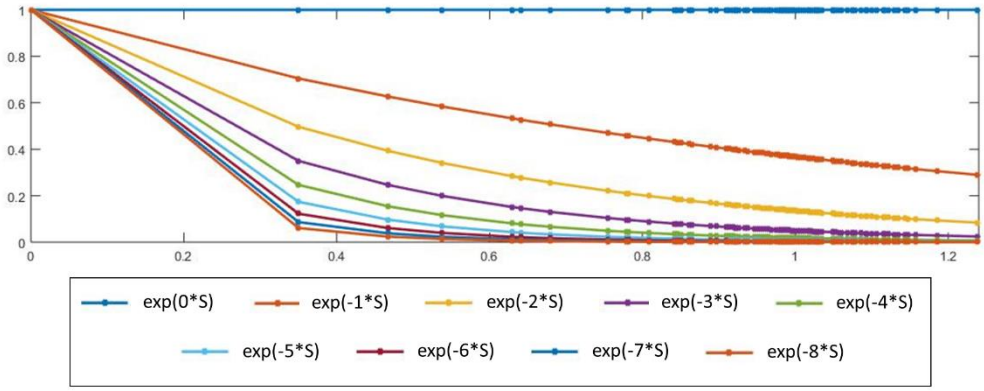

Figure 5.5: Example of the aligned diffusion kernel with a real set of eigenvalues compose from a structural connectivity of 82 parcels.

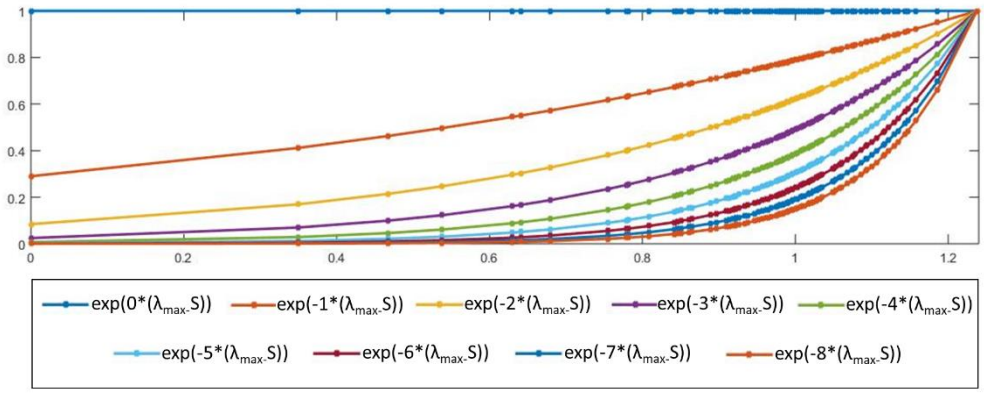

Figure 5.6: Example of the liberal diffusion kernel with a real set of eigenvalues compose from a structural connectivity of 82 parcels.

To avoid the empirical selection of the parameter, which is one of the limitations of Medaglia and colleagues' work [31], a paradigm can be defined on the spectrum of each set of components, formulated as:

$$E = \left(U^{L^T}\hat{x}\right)^2 = \left(U^{L^T}U^L\left(U^{L^T}Dx\right)\right)^2 = \left(U^{L^T}Dx\right)^2$$

Ideally the parameter τ, which is equivalent for aligned and liberal diffusion kernels, gives the same energy to aligned and liberal regime. However, to find the best τ, the contribution of the middle regime is important. In particular, to equally distribute

aligned, liberal and middle components the energy has to be equivalent, but the middle regime represents the discarded part of the signal from both aligned and liberal. For this reason, here the constraint is formulated as: the middle component signal must have the same energy as the sum of the aligned and liberal signals, generating smooth band filters.

Empirically, the constraint highlighted a high contribution of middle components, choosing a smaller set then 10 components for aligned and liberal filters. Mathematically, calculating the middle regime energy, it is demonstrated that the composition of the middle diffusion kernel generates mixed aligned and liberal components. These components add power to the middle regime, hiding the contribution of the middle and aligned components. For this reason, a square root is added in the aligned and liberal diffusion kernel definitions, which permit to have higher diffusion kernel values in the energy calculation:

$$D_A = \sqrt{exp(\tau * S)}$$

$$D_L = \sqrt{exp(\tau * (max(S) - S))}$$

Consequently, D_M remains:

$$D_M = 1 - (D_A + D_L)$$

5.3 RESULTS

Simulation. The randomization process highlighted the importance of the real structural eigenmodes. The differences between the set of eigenmodes from a real connectivity (Figure 5.7-A) and from the randomize matrix (Figure 5.7-B) are clearly remarkable already from a visual inspection.

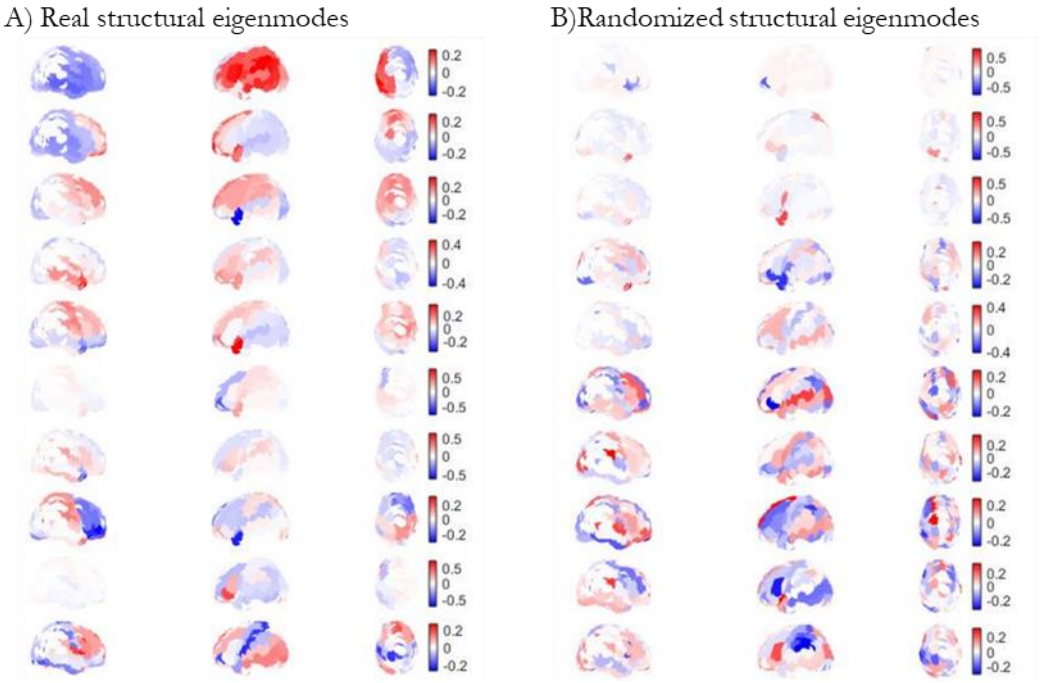

Figure 5.7: set of first ten real eigenmodes (Panel A) with an example of the first 10 eigenmodes extracted from a randomize matrix.

Indeed, the real set of structural bases presents some geometrical global connections, such as the Left-Right connection, the Fronto-Parietal one and the Fronto-temporal one. The randomized example, instead, shows some focused eigenmodes highlighting only local connections. The ε_{ratio}^{t} quantifies the prevalence of aligned or liberal components using the respectively filtered signals. In details, negative values of the ε_{ratio}^{t} mean a prevalence of liberal components (blue scale in Figure 5.8), while positive values mean prevalence of aligned components (red scale in Figure 5.8). The real set of eigenmodes permits to verify the correct definition of aligned and liberal components, while the randomize ones validate the need of the real eigenmodes in the model. The mean ε_{ratio}^{t} using the real set of structural bases estimate exactly the separation of the two periods, the first second aligned and the second one liberal (see Figure 5.8-A). The result shows the direct implication of the structure in the process and give a first step of validation of the approach. The ratio of the randomization process shows overall a prevalence of liberal components in both periods (see Figure 5.8-B). Moreover, in some of the 1000 simulations an opposite estimation of the two periods is retrieved, i.e. negative values in the aligned period and positive values in the liberal part.

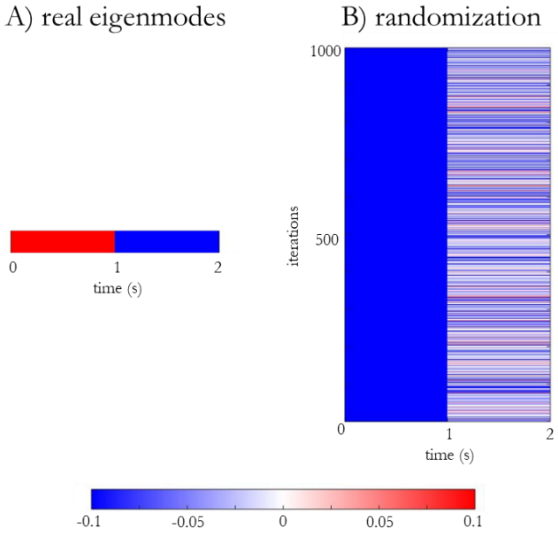

Figure 5.8: ε_{ratio}^{t} using the real set of eigenmodes.

Real data. After the preliminary validation of the structural eigenmodes, the real data are analysed in both motor movement task and resting state, to demonstrate the usability of the model as a structural-functional biomarker. The structural eigenmodes for each subject is derived from the group connectivity in the atlas resolution (see Figure 5.7-A). All of them present the typical geometrical global connections as already presented in the simulation analysis. All the three definitions (aligned, middle and liberal) are used in this analysis, reporting the results in three different ratios (A/L, A/M and M/L). Using the tMEG signal in both right and left hand movement, the ratio estimated shows high aligned prevalence before the timing 0 – i.e. when the movement starts (see the increasing of the EMG signal in Figure 5.9-A), which are highlighted with positive values (red colour) in both A/L (see first line of Figure 5.9-A) and A/M (see second line of Figure 5.9-A). This period can be related to the preparation timing, in which the brain uses global connections to spread the instruction for the movement. On the other hand, during the movement a prevalence of liberal components is highlighted with negative values in both A/L (see first line of Figure 5.9-A) and M/L (see third line of Figure 5.9-A). The line M/L (see third line of Figure 5.9-A) presents low values, meaning that the middle components are quite similar to the liberal ones. In general, it is easier to see the pattern in left hand in all the subjects presented. This could be explained by the fact that all subjects are right-handed, so they were probably more concentrated during

the left-hand task. Unfortunately, a left-hand dataset is still missing in the MEG-HCP database. On the other hand, the resting state analysis shows a continue fluctuation between aligned and liberal, as a periodic signal with a specific frequency (shown in Figure 5.9-B). However, the middle components still present low ratio values when they are compared with the liberal ones, reinforcing the similarity between the two components.

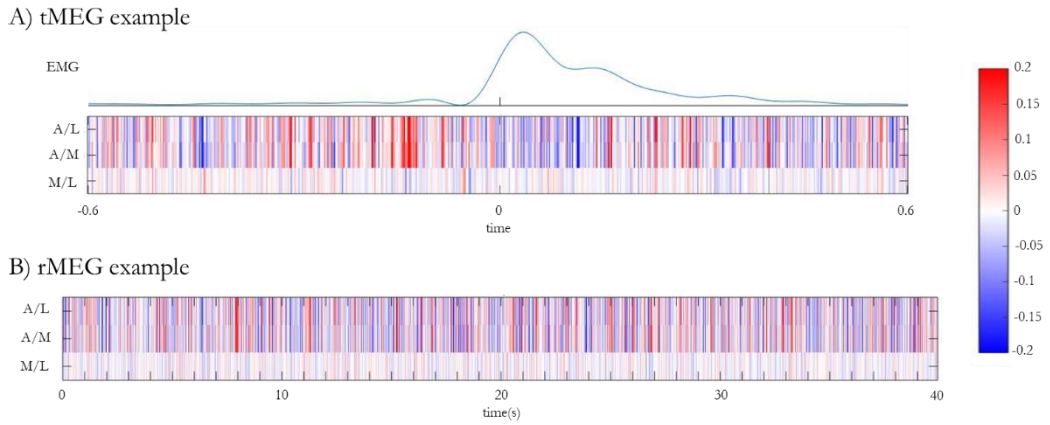

Figure 5.9: summary of the three ratios for the example subject (id 106521) in the left-hand task movement (Panel A) and resting state (Panel B).

5.4 PARTIAL CONCLUSION

This work represents a preliminary study in real subjects, which demonstrates the reliability of GSP as possible method to investigate the structure-function link in the human brain. It allowed to highlight the contribution of long and global structural connections at rest and during motor task. In details, a period of high alignment of functional signals to the brain structure is identified right before the motor task. This temporal interval is probably related to the preparation of the movement that uses the global long indirect connections of the brain to spread the instruction. While during the motor task the activation in the brain can be more focused on the regions related to the task (the motor cortex in the case of movement), causing a prevalence of liberal components that are related to the short, almost direct, structural connection of those regions.

The model is tested with MEG data, because they provide a more accurate source localization, but it is possible to use this multimodal approach also with EEG. This opens the possibility to test the model in clinical applications in which EEG recordings are more suitable. For example, applying the GFT on the adjacency matrices of stroke subjects, the eigenmodes could show the lack of some connections related to stroke lesions. Moreover, acquiring EEG or MEG signals in stroke subjects during a motor task and resting-state, the link between function and structure could be evaluated revealing alternative paths that the brain can use thanks to the plasticity process after the injury.

6 Conclusions and Outlook

The major novel contribution of this PhD Thesis focuses on the design of a new multimodal approach for the study of brain connectivity, highlighting the importance of considering structural connectivity when analysing functional signals in the brain. The proliferation of different methods to acquire and reconstruct the signal of the Diffusion Weighted Magnetic Resonance Imaging offers a plethora of choices for the estimation of structural connectivity. A detailed analysis to compare the different estimates of structural connectivity appears therefore necessary to define the best combination of models to reliably reconstruct connectomes. Moreover, even if the presence of a correlation between functional and structural connections is nowadays clear, the literature still lacks a precise description of this link. Recent attempts of using graph signal processing to investigate this association were presented with promising findings [31] [32]. For these reasons, I have focused in this work first on a detailed comparison of the different methods to extract structural connectivity, followed by the modelling of a multimodal framework that combines the best estimate of structural connectivity with the high temporal resolution functional signals acquired on the scalp via encephalography.

6.1 SUMMARY OF THE MAIN FINDINGS

In **Chapter 3**, I presented a preliminary assessment of the most informative properties that can be estimated from the diffusion signal, using advanced reconstruction models. The microstructural indices became popular in the last decade as weighting properties for structural graph, but the proliferation of new advanced models provoked an increase of the number of the different properties that can be used. Different well-known indices, such as Fractional Anisotropy, are already defined as biomarkers in literature and used to define a preliminary correlation between structure and function presented in literature [10]. In this context, we evaluated the set of indices extracted from more advanced propagator models (SHORE and MAP MRI) in the clinical application of stroke, defining a set of possible biomarkers. This allowed to highlight significant differences between stroke patients and healthy controls at different structural connectivity levels, from specific connections related to the motor impairment, to the whole connectivity evaluated with graph theory and machine learning approaches.

In **Chapter 4**, I focused on identifying the best estimate of structural connectivity with the actual possible knowledge. The reliability of structural connectivity was evaluated with different reconstruction models, tractography algorithms and weighting properties. Different reconstruction models, i.e. Spherical Deconvolution and the advanced *Propagator* and *Compartmental models*, are evaluated in comparison to the simplest Diffusion Tensor model. A paradigm that allows to estimate sensitivity and specificity of each combination was used to identify the model that reaches the best specificity, maintaining a very high reproducibility across different healthy subjects. The variability of the different approaches in both subject and group level analysis was highlighted. The best performance was reached by the Multiple Shell Multi Tissue model, which represents an advanced extension of the Spherical Deconvolution model, paired with probabilistic tractography. The findings suggested a trade-off between the restricted reconstruction model and the degrees of freedom of tractography. In details, the advanced Spherical Deconvolution model permits to solve partially the complex architecture, allowing to have a conservative reconstruction across different acquisitions of the same subject. On top of that, probabilistic tractography allows to maintain a high reproducibility across subjects with its robustness in areas of high uncertainty, such as crossing or noise areas. The binary structural connectivity achieved the best correlation range across subjects and acquisitions, performing the best classification between subjects across all methods. However, the highest correlation across subjects was reached by the weighted connectivity with the fiber density property, decreasing the performance values in almost all cases. On the other hand, the microstructural properties tested with the test-retest paradigm highlighted the high variability across healthy subject that required further investigation to allow using different properties in the model that integrates structure and function.

Finally, in **Chapter 5** I addressed the most challenging issue described in this thesis, i.e. the integration of structural and functional signals. A new model based on graph signal processing is presented, that permits to combine the structural bases, extracted with graph Fourier transform, and the encephalography signals, defined on the nodes of the structural graphs. The model follows the idea to filter the functional signal based on its degree of alignment to the underlying structural connectivity. With respect to the literature, different limitations are here addressed and overcome, as,

for example, the use high temporal functional signals (EEG and MEG), and the automated definition of the filter cut-offs for the functional signal. A validation on simulated data and a preliminary testing step on real data at rest and during motor task showed that a specific pattern can be reached using align and liberal components. In details, the resting state analysis retrieved the expected fluctuation as a periodic signal that change from liberal to aligned and vice versa with a specific frequency. On the other hand, the motor task presents a specific pattern comprising a strong aligned period, probably related to the preparation of the movement, and a liberal period during the motor task, due by the activation of short path related to the activated motor cortex.

6.2 LIMITATION OF THE RESEARCH

The analysis of the possible estimates of structural connectivity showed in Chapter 4 focused on different classical and advanced recent models. In details, it is restricted in the properties derived from the models used in the analysis, missing all the advanced microstructural properties derived from, for example, the Simple Harmonic Oscillator based Reconstruction and Estimation model. The study could be extended to the analysis of those indices, viewing the stability presented in Chapter 3. The results in Chapter 3, about the suitability of some microstructural properties to characterize the stroke impairment, open the issue of the comparison between different structural connectivity estimation in the application to different clinical diseases, extending the analysis to the microstructural properties. Moreover, the comparison between different estimations of structural connectivity can be particularly useful in a clinical datasets, giving more information then the lonely reproducibility.

Another limitation of this study is presented by the model that combines structure and function (Chapter 5), which is restricted in the derivation of the eigenmodes from the binary structural connectivity. This can lead to the extension of weighted structural graph, using for example microstructural properties derived from advanced models if they will present a good reproducibility in terms of classification performance using the test-retest paradigm and correlation values across healthy

subjects. Moreover, some statistical analyses presented in Chapter 3 can be used to test the reproducibility and the relevance in the clinical applications.

In this work, only a preliminary validation is presented for the multimodal approach using simulated data and few real datasets. In order to test the new model in *in-vivo* data, a deep analysis is required that extends the real data analysis on more subjects. Precisely, the results extracted from real subjects give the chance to better understand the resting state acquisition, studying the frequency of fluctuations in different subjects, and answering specific questions, as for example if the fluctuations represent a basal rhythm of the brain for each specific subject, or if there is a specific range of this rhythm maybe based on the age. This implies different types of studies, as the analysis of brain development, familiarity, etc. On the other hand, the results of the motor task analysis would be enriched by the analysis with different tasks, already presented in the HCP data, as the working memory, language, social and emotional cognitive. Finally, the multimodal approach is preliminary tested only on healthy subjects, and would therefore benefit from future application to clinical context.

6.3 FUTURE PERSPECTIVES FOR CLINICAL APPLICATIONS

Several extensions of this work to the clinical field could be envisaged. First, the characterization of the best trade-off between sensitivity and specificity of the structural connectivity could be extended comparing several reconstruction models and using different microstructural properties, which are relevant for specific diseases, as shown in Chapter 3 for stroke patients. Moreover, the integrated model for binary structural and encephalography functional signals could open the perspective for clinical applications. Nowadays, different neurodegenerative and mental disorders are studies in clinical neurology. The definition of reliable imaging-based biomarkers for clinical decision and therapeutic interventions necessitates the identification of clearer associations between structure and function. The majority of the previous work in literature considered individually function or structure in brain impairment, such as stroke [105] [106] [69], parkinsonism [107] [108] [109], Alzheimer disease [110] [111] [112], epilepsy [113] [114] [115] and more other. Future

studies should investigate the combination of these through multimodal approaches in order to provide a more detailed and complete description of the pathological phenomena causing abnormalities in brain connections. The multimodal approach could characterize disease phenotypes and progression, improving therapeutic strategies. The integrated model presented in this thesis could represent a first step in this way, that can be applied on different diseases using high temporal resolution encephalography datasets. Preliminary applications in this direction could be easily done for instance in Parkinson disease, using the available Parkinson progression marker initiative (PPMI) database, from a multi-center study comprising 400 diagnosed Parkinsonian subjects and 200 healthy ones with both DW-MRI and EEG acquisitions [116].

REFERENCES

[1] O. Sporns, G. Tononi e R. Kötter, The human connectome: a structural description of the human brain, PLoS computational biology, 1(4), e42, 2005.

[2] P. Hagmann, From diffusion MRI to brain connectomics, EPFL Lausanne: Doctoral dissertation, 2005.

[3] A. Waller, Experiments on the section of the glossopharyngeal and hypoglossal nerves of the frog, and observations of the alterations produced thereby in the structure of their primitive fibres, Philosophical Transactions of the Royal Society of London, 140, 423-429., 1850.

[4] J. Schmahmann, D. Pandya, R. Wang, G. Dai, H. D'arceuil, A. de Crespigny e V. Wedeen, Association fibre pathways of the brain: parallel observations from diffusion spectrum imaging and autoradiography, Brain, 130(3), 630-653, 2007.

[5] K. Friston, Functional and effective connectivity in neuroimaging: a synthesis, Human brain mapping, 2(1-2), 56-78, 1994.

[6] N. Kasthuri e J. Lichtman, The rise of the'projectome', Nature Methods, 4(4), 307, 2007.

[7] S. Ogawa, T. Lee, A. Kay e D. Tank, Brain magnetic resonance imaging with contrast dependent on blood oxygenation, Proceedings of the National Academy of Sciences, 87(24), 9868-9872, 1990.

[8] D. Le Bihan, E. Breton, D. Lallemand, P. Grenier, E. Cabanis e M. Laval-Jeantet, MR imaging of intravoxel incoherent motions: application to diffusion and perfusion in neurologic disorders, Radiology, 161(2), 401-407, 1986.

[9] P. Basser, J. Mattiello e D. LeBihan, MR diffusion tensor spectroscopy and imaging, Biophysical journal, 66(1), 259-267, 1994.

[10] M. Falcon, J. Riley, V. Jirsa, A. McIntosh, A. Shereen, E. Chen e A. Solodkin, The virtual brain: modeling biological correlates of recovery after chronic stroke, Frontiers in neurology, 6, 228, 2015.

[11] S. Baillet, J. Mosher e R. Leahy, Electromagnetic brain mapping, IEEE Signal processing magazine, 18(6), 14-30, 2001.

[12] M. Hamalainen e J. Sarvas, Realistic conductivity geometry model of the human head for interpretation of neuromagnetic data, IEEE transactions on biomedical engineering, 36(2), 165-171, 1989.

[13] B. Roth, M. Balish, A. Gorbach e S. Sato, How well does a three-sphere model predict positions of dipoles in a realistically shaped head?, Electroencephalography and clinical Neurophysiology, 87(4), 175-184, 1993.

[14] B. Cuffin, EEG localization accuracy improvements using realistically shaped head models, IEEE Transactions on Biomedical Engineering, 43(3), 299-303, 1996.

[15] A. Crouzeix, B. Yvert, O. Bertrand e J. Pernier, An evaluation of dipole reconstruction accuracy with spherical and realistic head models in MEG, Clinical Neurophysiology, 110(12), 2176-2188., 1999.

[16] J. Haueisen, A. Boettner, M. Funke e H. Brauer, Effect of boundary element discretization on forward calculation and the inverse problem in electroencephalography and magnetoencephalography, Biomedizinische Technik. Biomedical engineering, 42(9), 240-248, 1997.

[17] J. Haueisen, C. Ramon, M. Eiselt, H. Brauer e H. Nowak, Influence of tissue resistivities on neuromagnetic fields and electric potentials studied with a finite element model of the head, IEEE Transactions on Biomedical Engineering, 44(8), 727-735, 1997.

[18] S. Gabriel, R. Lau e C. Gabriel, The dielectric properties of biological tissues, Physics in medicine & biology, 41(11), 2231-2251-2271, 1996.

[19] B. Vanrumste, G. Van Hoey, R. Van de Walle, M. D'havé, I. Lemahieu e P. Boon, Dipole location errors in electroencephalogram source analysis due to volume conductor model errors, Medical and Biological Engineering and Computing, 38(5), 528-534, 2000.

[20] N. Gençer e C. Acar, Sensitivity of EEG and MEG measurements to tissue conductivity, Physics in Medicine & Biology, 49(5), 701, 2004.

[21] J. Ollikainen, M. Vauhkonen, P. Karjalainen e J. Kaipio, Effects of local skull inhomogeneities on EEG source estimation, Medical engineering & physics, 21(3), 143-154, 1999.

[22] K. Wendel e J. Malmivuo, «Correlation between live and post mortem skull conductivity measurements,» in *In Engineering in Medicine and Biology Society, 2006. EMBS'06. 28th Annual International Conference of the IEEE (pp. 4285-4288). IEEE.*, 2006.

[23] C. Michel, M. Murray, G. Lantz, S. Gonzalez, L. Spinelli e R. de Peralta, EEG source imaging, Clinical neurophysiology, 115(10), 2195-2222, 2004.

[24] K. Wendel, O. Väisänen, J. Malmivuo, N. Gencer, B. Vanrumste, P. Durka, R. Magjarevic, S. Supek, M. Pascu, H. Fontenelle e R. de Peralta Menendez, EEG/MEG source imaging: methods, challenges, and open issues, Computational intelligence and neuroscience, 2009, 13, 2009.

[25] R. Pascual-Marqui, Review of methods for solving the EEG inverse problem, International journal of bioelectromagnetism, 1(1), 75-86, 1999.

[26] R. Grech, T. Cassar, J. Muscat, K. Camilleri, S. Fabri, M. Zervakis, P. Xanthopoulos, V. Sakkalis e B. Vanrumste, Review on solving the inverse problem in EEG source analysis, Journal of neuroengineering and rehabilitation, 5(1), 25, 2008.

[27] C. Honey, R. Kötter, M. Breakspear e O. Sporns, Network structure of cerebral cortex shapes functional connectivity on multiple time scales, Proceedings of the National Academy of Sciences, 104(24), 10240-10245, 2007.

[28] C. Honey, O. Sporns, C. L. X. Gigandet, J. Thiran, R. Meuli e P. Hagmann, Predicting human resting-state functional connectivity from structural connectivity, Proceedings of the National Academy of Sciences, 106(6), 2035-2040, 2009.

[29] e. a. Van Den Heuvel, Functionally linked resting-state networks reflect the underlying structural connectivity architecture of the human brain, Human brain mapping, 30(10), 3127-3141, 2009.

[30] F. Bowman, L. Zhang, G. Derado e S. Chen, Determining functional connectivity using fMRI data with diffusion-based anatomical weighting, NeuroImage, 62(3), 1769-1779, 2012.

[31] J. Medaglia, W. Huang, E. Karuza, A. Kelkar, S. Thompson-Schill, A. Ribeiro e D. & Bassett, Functional alignment with anatomical networks is associated with cognitive flexibility, Nature Human Behaviour, 2(2), 156, 2018.

[32] W. Huang, T. Bolton, A. Ribeiro e D. Van De Ville, A Graph Signal Processing View on Functional Brain Imaging, arXiv preprint arXiv:1710.01135, 2017.

[33] J. Meier, P. Tewarie, A. Hillebrand, L. Douw, B. van Dijk, S. Stufflebeam e P. Van Mieghem, A mapping between structural and functional brain networks, Brain connectivity, 6(4), 298-311, 2016.

[34] L. Astolfi, F. De Vico Fallani, F. Cincotti, D. Mattia, M. Marciani, S. Bufalari, S. Salinari, A. Colosimo, L. Ding, J. Edgar, W. Heller, G. Miller, B. He e F. Babiloni, Imaging functional brain connectivity patterns from high-resolution EEG and fMRI via graph theory, Psychophysiology, 44(6), 880-893, 2007.

[35] E. Bullmore e O. Sporns, Complex brain networks: graph theoretical analysis of structural and functional systems, Nature Reviews Neuroscience, 10(3), 186, 2009.

[36] U. Brandes e T. Erlebach, Fundamentals, In Network analysis (pp. 7-15). Springer, Berlin, Heidelberg, 2005.

[37] D. Shuman, S. Narang, P. Frossard, A. Ortega e P. Vandergheynst, The emerging field of signal processing on graphs: Extending high-dimensional data analysis to networks and other irregular domains, IEEE Signal Processing Magazine, 30(3), 83-

98, 2013.

[38] E. Stejskal e J. Tanner, Spin diffusion measurements: spin echoes in the presence of a time-dependent field gradient, The journal of chemical physics, 42(1), 288-292, 1965.

[39] D. Alexander, G. Barker e S. Arridge, (2002). Detection and modeling of non-Gaussian apparent diffusion coefficient profiles in human brain data, Magnetic Resonance in Medicine: An Official Journal of the International Society for Magnetic Resonance in Medicine, 48(2), 331-340, 2002.

[40] L. Frank, Anisotropy in high angular resolution diffusion-weighted MRI, Magnetic Resonance in Medicine: An Official Journal of the International Society for Magnetic Resonance in Medicine, 45(6), 935-939, 2001.

[41] D. Tuch, T. Reese, M. Wiegell, N. Makris e J. Belliveau, High angular resolution diffusion imaging reveals intravoxel, Magnetic Resonance in Medicine: An Official Journal of the International Society for Magnetic Resonance in Medicine, 48(4), 577-582, 2002.

[42] J. Tournier, F. Calamante, D. Gadian e A. Connelly, Direct estimation of the fiber orientation density function from diffusion-weighted MRI data using spherical deconvolution, NeuroImage, 23(3), 1176-1185, 2004.

[43] F. Aboitz e J. Montiel, One hundred million years of interhemispheric communication: the history of the corpus callosum, Brazilian journal of medical and biological research, 36(4), 409-420, 2003.

[44] H. Zhang, T. Schneider, C. Wheeler-Kingshott e D. Alexander, Noddi: Practical in vivo neurite orientation dispersion and density imaging, Neuroimage, 61(4), 1000-1016, 2012.

[45] M. Kleinnijenhuis, Imaging fibres in the brain, Radboud University Nijmegen: Doctoral dissertation, 2014.

[46] E. Özarslan, C. Koay, T. Sheperd, S. Blackband e P. Basser, Simple harmonic oscillator based reconstruction and estimation for threedimensional, Processings of International Society for Magnetic Resonance in Medicine, 17 (pp. 1396), 2009.

[47] E. Özarslan, C. Koay, T. Shepherd, M. Komlosh, M. Irfanoglu, C. Pierpaoli e P. Basser, Mean apparent propagator (MAP) MRI: A novel diffusion imaging method for mapping tissue microstructure, NeuroImage, 78, 16-32, 2013.

[48] M. Zucchelli, M. Descoteaux e G. Menegaz, A generalized SMT-based framework for diffusion MRI microstructural model estimation, In Computational Diffusion MRI (pp. 51-63). Springer, Cham, 2018.

[49] E. Özarslan, C. Koay e P. Basser, Simple harmonic oscillator based reconstruction and estimation for one-dimensional q-space magnetic resonance (1D-SHORE), In

Excursions in Harmonic Analysis, Volume 2 (pp. 373-399). Birkhäuser, Boston., 2013.

[50] R. Fick, M. Zucchelli, G. Girard, M. Descoteaux, G. Menegaz e R. Deriche, Using 3D-SHORE and MAP-MRI to obtain both tractography and microstructural constrast from a clinical DMRI acquisition, In Biomedical Imaging (ISBI), 2015 IEEE 12th International Symposium on (pp. 436-439). IEEE, 2015.

[51] J. Cheng, R. Deriche, T. Jiang, D. Shen e P. Yap, Non-negative spherical deconvolution (NNSD) for estimation of single-/multi-shell diffusion MRI, NeuroImage, 101, 750-764., 2014.

[52] E. Kaden, F. Kruggel e D. Alexander, Quantitative mapping of the per-axon diffusion coefficients in brain white matter, Magnetic resonance in medicine, 75(4), 1752-1763, 2016.

[53] E. Kaden, N. Kelm, R. Carson, M. Does e D. Alexander, Multicompartment microscopic diffusion imaging, NeuroImage, 139, 346-359, 2016.

[54] M. Zucchelli, L. Brusini, C. Méndez, A. Daducci, C. Granziera e G. Menegaz, What lies beneath? diffusion eap-based study of brain microstructure, Medical image analysis, 32, 145-156, 2016.

[55] P. Basser e C. Pierpaoli, Microstructural and physiological features of tissues elucidated by quantitative-diffusion-tensor MRI, Journal of magnetic resonance, Series B, 111(3), 209-219, 1996.

[56] V. Wedeen, P. Hagmann, W. Tseng, T. Reese e R. Weisskoff, Mapping complex tissue architecture with diffusion spectrum magnetic resonance imaging, Magnetic resonance in medicine, 54(6), 1377-1386, 2005.

[57] H. Zhang, P. Hubbard, G. Parker e D. Alexander, Axon diameter mapping in the presence of orientation dispersion with diffusion MRI, Neuroimage, 56(3), 1301-1315, 2011.

[58] Y. Wu e A. Alezìxander, Hybrid diffusion imaging, NeuroImage, 36(3), 617-629, 2007.

[59] P. Basser, S. Pajevic, C. Pierpaoli, J. Duda e A. Aldroubi, In vivo fiber tractography using DT-MRI data, Magnetic resonance in medicine, 44(4), 625-632, 2000.

[60] S. Mori, B. Crain, V. Chacko e P. Van Zijl, Three-dimensional tracking of axonal projections in the brain by magnetic resonance imaging, Annals of Neurology: Official Journal of the American Neurological Association and the Child Neurology Society, 45(2), 265-269, 1999.

[61] T. Conturo, N. Lori, T. Cull, E. Akbudak, A. Snyder, J. Shimony, R. McKinstry, H. Burton e M. Raichle, Tracking neuronal fiber pathways in the living human brain,

Proceedings of the National Academy of Sciences, 96(18), 10422-10427, 1999.

[62] E. Garyfallidis, Towards an accurate brain tractography, University of Cambridge: Doctoral dissertation, 2013.

[63] S. Mori, B. Crain e v. Z. P.C., 3D brain fiber reconstruction from diffusion MRI, Neuroimage, 7(4 PART II), 1998.

[64] M. Van Den Heuvel, C. Stam, M. Boersma e H. Pol, Small-world and scale-free organization of voxel-based resting-state functional connectivity in the human brain, Neuroimage, 43(3), 528-539, 2008.

[65] R. Martuzzi, R. Ramani, M. Qiu, X. Shen, X. Papademetris e R. Constable, A whole-brain voxel based measure of intrinsic connectivity contrast reveals local changes in tissue connectivity with anesthetic without a priori assumptions on thresholds or regions of interest, Neuroimage, 58(4), 1044-1050, 2011.

[66] P. Bellec, V. Perlbarg, S. Jbabdi, M. Pélégrini-Issac, J. Anton, J. Doyon e H. Benali, Identification of large-scale networks in the brain using fMRI, Neuroimage, 29(4), 1231-1243, 2006.

[67] R. Craddock, G. James, P. Holtzheimer, X. Hu e H. Mayberg, A whole brain fMRI atlas generated via spatially constrained spectral clustering, Human brain mapping, 33(8), 1914-1928, 2012.

[68] G. Adluru, Y. Gur, J. Anderson, L. Richards, N. Adluru e E. DiBella, Assessment of white matter microstructure in stroke patients using NODDI., n Engineering in Medicine and Biology Society (EMBC), 2014 36th Annual International Conference of the IEEE (pp. 742-745). IEEE, 2014.

[69] C. Granziera, A. Daducci, D. Meskaldji, A. Roche, P. Maeder, P. Michel, N. Hadjikhani, A. Sorensen, R. Frackowiak, J. Thiran e R. Meuli, A new early and automated MRI-based predictor of motor improvement after stroke, Neurology, 79(1), 39-46, 2012.

[70] X. Nguyen, J. Chan, S. Romano e J. Bailey, Effective global approaches for mutual information based feature selection, In Proceedings of the 20th ACM SIGKDD international conference on Knowledge discovery and data mining (pp. 512-521). ACM, 2014.

[71] M. Glasser, S. Sotiropoulos, J. Wilson, T. Coalson, B. Fischl, J. Andersson, J. Xu, S. Jbabdi, M. Webster, J. Polimeni e D. Van Essen, The minimal preprocessing pipelines for the Human Connectome Project, Neuroimage, 80, 105-124, 2013.

[72] H. Peng, F. Long e C. Ding, Feature selection based on mutual information criteria of max-dependency, max-relevance, and min-redundancy, IEEE Transactions on pattern analysis and machine intelligence, 27(8), 1226-1238, 2005.

[73] G. Brown, A. Pocock, M. Zhao e M. Luján, Conditional likelihood maximisation: a unifying framework for information theoretic feature selection, Journal of machine learning research, 13(Jan), 27-66, 2012.

[74] Y. Lin, A. Daducci, D. Meskaldji, J. Thiran, P. Michel, R. Meuli, G. Krueger, G. Menegaz e C. Granziera, Quantitative analysis of myelin and axonal remodeling in the uninjured motor network after stroke, Brain connectivity, 5(7), 401-412, 2015.

[75] K. Friston, J. Ashburner, C. Frith, J. Poline, J. Heather e R. Frackowiak, Spatial registration and normalization of images, Human brain mapping, 3(3), 165-189, 1995.

[76] J. Bland e D. Altman, Statistics notes: measurement error, Bmj, 312(7047), 1654, 1996.

[77] Y. Chen, D. Wang e J. Detre, Test–retest reliability of arterial spin labeling with common labeling strategies, Journal of Magnetic Resonance Imaging, 33(4), 940-949, 2011.

[78] J. Pinto, J. Jorge, I. Sousa, P. Vilela e P. Figueiredo, Fourier modeling of the BOLD response to a breath-hold task: optimization and reproducibility, Neuroimage, 135, 223-231, 2016.

[79] J. Fleiss, Methods for rates and proportions, Wiley, New York, 2nd edn., 1981.

[80] D. Cicchetti, Methodological commentary the precision of reliability and validity estimates re-visited: distinguishing between clinical and statistical significance of sample size requirements, Journal of Clinical and Experimental Neuropsychology, 23(5), 695-700, 2011.

[81] S. Marenco, R. Rawlings, G. Rohde, A. Barnett, R. Honea, C. Pierpaoli e D. Weinberger, Regional distribution of measurement error in diffusion tensor imaging, Psychiatry Research: Neuroimaging, 147(1), 69-78, 2006.

[82] E. Heiervang, T. Behrens, C. Mackay, M. Robson e H. Johansen-Berg, Between session reproducibility and between subject variability of diffusion MR and tractography measures, Neuroimage, 33(3), 867-877, 2006.

[83] S. Maniega, M. Bastin, P. Armitage, A. Farrall, T. Carpenter, P. Hand, V. Cvoro, C. Rivers e J. Wardlaw, Temporal evolution of water diffusion parameters is different in grey and white matter in human ischaemic stroke, Journal of Neurology, Neurosurgery & Psychiatry, 75(12), 1714-1718, 2004.

[84] C. Sotak, The role of diffusion tensor imaging in the evaluation of ischemic brain injury–a review, NMR in Biomedicine: An International Journal Devoted to the Development and Application of Magnetic Resonance In Vivo, 15(7-8), 561-569, 2002.

[85] G. Roffo, S. Melzi e M. Cristani, Infinite feature selection, In Proceedings of the IEEE International Conference on Computer Vision (pp. 4202-4210), 2015.

[86] J. Andersson, S. Skare e J. Ashburner, How to correct susceptibility distortions in spin-echo echo-planar images: application to diffusion tensor imaging, Neuroimage, 20(2), 870-888, 2003.

[87] J. Andersson e S. Sotiropoulos, Non-parametric representation and prediction of single-and multi-shell diffusion-weighted MRI data using Gaussian processes, Neuroimage, 122, 166-176, 2015.

[88] R. Wang, T. Benner, A. Sorensen e V. Wedeen, Diffusion toolkit: a software package for diffusion imaging data processing and tractography, In Proc Intl Soc Mag Reson Med (Vol. 15, No. 3720), 2007.

[89] J. Tournier, F. Calamante e A. Connelly, MRtrix: diffusion tractography in crossing fiber regions, International Journal of Imaging Systems and Technology, 22(1), 53-66, 2012.

[90] G. Girard, K. Whittingstall, R. Deriche e M. Descoteaux, Structural connectivity reproducibility through multiple acquisitions, In Organization for Human Brain Mapping, 2015.

[91] P. Hagmann, L. Cammoun, X. Gigandet, R. Meuli, C. Honey, V. Wedeen e O. Sporns, Mapping the structural core of human cerebral cortex, PLoS biology, 6(7), e159, 2008.

[92] M. Vaessen, P. Hofman, H. Tijssen, A. Aldenkamp, J. Jansen e W. Backes, The effect and reproducibility of different clinical DTI gradient sets on small world brain connectivity measures, Neuroimage, 51(3), 1106-1116, 2010.

[93] A. Zalesky, A. Fornito, I. Harding, L. Cocchi, M. Yücel, C. Pantelis e E. Bullmore, Whole-brain anatomical networks: does the choice of nodes matter?, Neuroimage, 50(3), 970-983, 2010.

[94] D. Bassett, J. Brown, V. Deshpande, J. Carlson e S. Grafton, Conserved and variable architecture of human white matter connectivity, Neuroimage, 54(2), 1262-1279, 2011.

[95] L. Cammoun, X. Gigandet, D. Meskaldji, J. Thiran, O. Sporns, K. Do, P. Maeder, R. Meuli e P. Hagmann, Mapping the human connectome at multiple scales with diffusion spectrum MRI, Journal of neuroscience methods, 203(2), 386-397, 2012.

[96] H. Cheng, Y. Wang, J. Sheng, W. Kronenberger, V. Mathews, T. Hummer e A. Saykin, Characteristics and variability of structural networks derived from diffusion tensor imaging, Neuroimage, 61(4), 1153-1164, 2012.

[97] C. Buchanan, C. Pernet, K. Gorgolewski, A. Storkey e M. Bastin, Test–retest reliability of structural brain networks from diffusion MRI, Neuroimage, 86, 231-

243, 2014.

[98] B. Jeurissen, J. Tournier, T. Dhollander, A. Connelly e J. Sijbers, Multi-tissue constrained spherical deconvolution for improved analysis of multi-shell diffusion MRI data, NeuroImage, 103, 411-426, 2014.

[99] C. Becker, S. Pequito, G. Pappas, M. Miller, S. Grafton, D. Bassett e V. Preciado, Spectral mapping of brain functional connectivity from diffusion imaging, Scientific reports, 8(1), 1411, 2018.

[100] D. Van De Ville e G. Preti, Graph spectral analysis for modified diffusion flow: application to C. Elegans connectomic, In International Conference on Network Science, 2018.

[101] S. Atasoy, I. Donnelly e J. Pearson, Human brain networks function in connectome-specific harmonic waves, Nature communications, 7, 10340, 2016.

[102] A. Gramfort, M. Luessi, E. Larson, D. Engemann, D. Strohmeier, C. Brodbeck, R. Goj, M. Jas, T. Brooks, L. Parkkonen e M. Hämäläinen, MEG and EEG data analysis with MNE-Python, Frontiers in neuroscience, 7, 267, 2013.

[103] R. Buckner, F. Krienen, A. Castellanos, J. Diaz e B. Yeo, The organization of the human cerebellum estimated by intrinsic functional connectivity, American Journal of Physiology-Heart and Circulatory Physiology, 2011.

[104] B. Yeo, F. Krienen, J. Sepulcre, M. Sabuncu, D. Lashkari, M. Hollinshead, J. Roffman, J. Smoller, L. Zollei, J. Polimeni, F. B., H. Liu e R. Buckner, The organization of the human cerebral cortex estimated by intrinsic functional connectivity, J Neurophysiol, 106, 1125-1165, 2011.

[105] R. Pineiro, S. Pendlebury, H. Johansen-Berg e P. Matthews, Altered hemodynamic responses in patients after subcortical stroke measured by functional MRI, Stroke, 33(1), 103-109, 2002.

[106] N. Ward, M. Brown, A. Thompson e R. Frackowiak, Neural correlates of motor recovery after stroke: a longitudinal fMRI study, Brain, 126(11), 2476-2496, 2003.

[107] C. Summerfield, C. Junqué, E. Tolosa, P. Salgado-Pineda, B. Gómez-Ansón, M. Martí, P. Pastor, B. Ramírez-Ruíz e J. Mercader, Structural brain changes in Parkinson disease with dementia: a voxel-based morphometry study, Archives of Neurology, 62(2), 281-285, 2005.

[108] U. Ekman, J. Eriksson, L. Forsgren, S. Mo, K. Riklund e L. Nyberg, Functional brain activity and presynaptic dopamine uptake in patients with Parkinson's disease and mild cognitive impairment: a cross-sectional study, The Lancet Neurology, 11(8), 679-687, 2012.

[109] H. Baggio, R. Sala-Llonch, B. Segura, M. Marti, F. Valldeoriola, Y. Compta, E. Tolosa e C. Junqué, Functional brain networks and cognitive deficits in Parkinson's

disease, Human brain mapping, 35(9), 4620-4634, 2014.

[110] C. Grady, M. Furey, P. Pietrini, B. Horwitz e S. Rapoport, Altered brain functional connectivity and impaired short-term memory in Alzheimer's disease, Brain, 124(4), 739-756, 2001.

[111] K. Supekar, V. Menon, D. Rubin, M. Musen e M. Greicius, Network analysis of intrinsic functional brain connectivity in Alzheimer's disease, PLoS computational biology, 4(6), e1000100, 2008.

[112] C. Fennema-Notestine, D. Hagler Jr, L. McEvoy, A. Fleisher, E. Wu, D. Karow e A. Dale, Structural MRI biomarkers for preclinical and mild Alzheimer's disease, Human brain mapping, 30(10), 3238-3253, 2009.

[113] N. Voets, J. Adcock, R. Stacey, Y. Hart, K. Carpenter, P. Matthews e C. Beckmann, Functional and structural changes in the memory network associated with left temporal lobe epilepsy, Human brain mapping, 30(12), 4070-4081, 2009.

[114] Z. Zhang, W. Liao, H. Chen, D. Mantini, J. Ding, Q. Xu, Z. Wang, C. Yuan, G. Chen, Q. Jiao e G. Lu, Altered functional–structural coupling of large-scale brain networks in idiopathic generalized epilepsy, Brain, 134(10), 2912-2928, 2011.

[115] J. O'muircheartaigh, C. Vollmar, G. Barker, V. Kumari, M. Symms, P. Thompson, J. Duncan, M. Koepp e M. Richardson, Abnormal thalamocortical structural and functional connectivity in juvenile myoclonic epilepsy, Brain, 135(12), 3635-3644, 2012.

[116] K. Marek, D. Jennings, S. Lasch, A. Siderowf, C. Tanner, T. Simuni, C. Coffey, K. Kieburtz, E. Flagg, S. Chowdhury e W. Poewe, The parkinson progression marker initiative (PPMI), Progress in neurobiology, 95(4), 629-635, 2011.